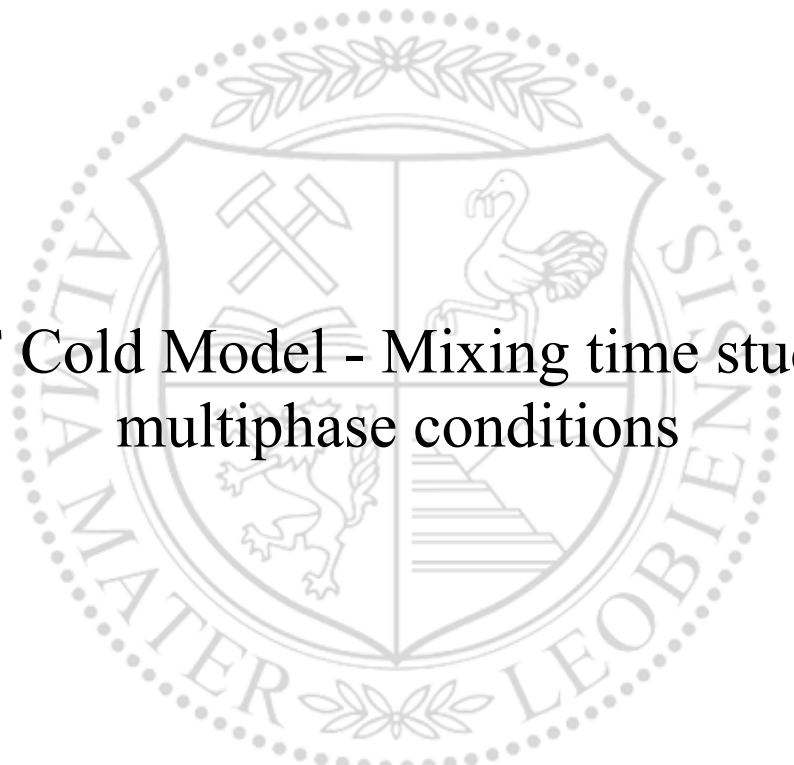Chair of Ferrous Metallurgy

Doctoral Thesis

BOF Cold Model - Mixing time study at multiphase conditions

Daniel Augusto Godinho de Carvalho

March 2021

AFFIDAVIT

I declare on oath that I wrote this thesis independently, did not use other than the specified sources and aids, and did not otherwise use any unauthorized aids.

I declare that I have read, understood, and complied with the guidelines of the senate of the Montanuniversität Leoben for "Good Scientific Practice".

Furthermore, I declare that the electronic and printed version of the submitted thesis are identical, both, formally and with regard to content.

Date 21.03.2021

Signature Author
Daniel Augusto Godinho de Carvalho

Abstract

The BOF process was born in 1949 in Linz, Austria. Fast growth for the Basic Oxygen Processes (BOP) was observed in the 1960s. By 1971, Basic Oxygen Furnace (BOF) produced more than half of the world's steel. The LD process led worldwide steel production to increase from 0.2 to 1.8 billion metric tons of crude steel per year. The integrated steelmaking route based on the BF-BOF is directly responsible for 70% of total world steel production. At least up until 2050, primary steelmaking based on the BOF technology is assumed to continue the main process route.

In an earlier work about lime dissolution and slag making for an industrial $330\,t$ BOF, the same process as presented in this thesis, several process parameters were studied. Nevertheless, the model's weak point was the efficiency factors that correlate the mixing energy related to top lance, bottom stirring, and decarburization reactions.

A couple of different reports for the agitation of a top blowing jet to the bath and bottom stirring are available in the literature, and different expressions to calculate the agitation power have been proposed. Although experimental conditions are used, these empirical assumptions are not necessarily suitable for all BOF processes. Those parameters substantially impact the steel process productivity, costs, and quality, and the mixing time concept investigated through cold modelling is perfect for assessing the system performance.

This thesis developed investigations through laboratory cold model to improve the mixing time and mass transfer rate due to a gradient of apparent density caused by different bottom stirring flow zone. The proposed setups were validated in the industrial environment, and more than 1750 trial heats were produced in a $330\,t$ BOF.

This research introduced novel modified dimensionless numbers (Fr^*_{LaSiP}, Eo^*_{LaSiP}, We^*_{LaSiP}, Q^*, and E^*), the new parameters added in the equations delivered a unique solution to develop a complete BOF process similarity. For the first time, a similarity study employed and associated the effects of the multi-nozzle supersonic lance, slag-phase and the bottom stirring gas parameters to design a new BOF cold model.

The methods applied in the laboratory measurements employed a mix of modified procedures available in the literature, and new techniques to evaluate the bath mixing time, mass transfer rate, jet penetration, decarburization area, sloping and projection rate for BOF cold modelling.

The industrial-scale experiments were fundamental to validate the laboratory trials,

the first phase of experiments delivered important laboratory and process data for seven different bottom stirring configurations.

Despite the influence of many other parameters and variables faced in the industrial environment, the performed trials delivered essential process data for a statistical and machine learning analysis.

Kurzfassung

Das LD-Verfahren wurde in 1949 in Linz, Österreich, entwickelt. Ein rascher Anstieg der Rohstahlproduktion mit diesem Verfahren erfolgte in den 1960er Jahren und 1971 wurden bereits damit mehr als die Hälfte der weltweit Stahlherstellung produziert. Durch das LD-Verfahren kam es weltweit zu einem Anstieg der jährlichen Stahlproduktion von damals 0,2 auf 1,8 Milliarden Tonnen Auf die klassische integrierte Stahlerzeugungsroute bestehend aus Hochofen und LD-Konverter entfallen heute mehr als 70% der weltweiten Rohstahlproduktion. Prognosen bis zum Jahr 2050 gehen davon aus, dass für die primäre Stahlherstellung der Hauptprozessroute weiterhin über die Rohstahlproduktion mit dem LD-Konverter sein wird.

In einer früheren Arbeit zur Kalkauflösung und Schlackenbildung wurden in einem 330 Tonnen Konverter bei Ternium BR in Brasilien, der auch in dieser vorliegenden Arbeit für Versuche im Industriemaßstab verwendet wird, der Einfluss mehrere Prozessparameter untersucht. Dabei wurde es festgestellt, dass Korrelation zwischen Mischenergie des Metallbades, die durch den vertikalen Sauerstoffstrahl der Blaselanze und dem Inertgasrühren durch die Bodenspülung in das Bad eingebracht wird, und der Entkohlungsreaktionen nicht befriedigend ist.

Zahlreiche Berichte hinsichtlich Rührwirkung des Stahlbades infolge des vertikalen Aufblasens und Bodenspülen mit Inertgas stehen in der Literatur zur Verfügung. Es wurden mehrere mathematische Beziehungen zur Berechnung der Rührleistung vorgeschlagen. Die Ergebnisse aus experimentellen Bedingungen wurden auf empirische Ansätze umgelegt, die aber nicht allgemeingültig sind. Die Rührwirkung hat einen erheblichen Einfluss auf die Produktivität, Kosten and Qualität des Prozesses. Für deren Bewertung ist die Ermittlung der Vermischungszeit mit einem Wasser-Kaltmodellen eine gute experimentelle Methodik.

In dieser vorliegenden Arbeit wurden Untersuchungen im Labor an einem Kaltmodell mit Wasser durchgeführt, um die Vermischungszeit und Stoffübergangsrate zu untersuchen. Es wurden verschiedene Anordnungen der Bodenspüler und Variationen der Gasbeaufschlagung der Spüler validiert und optimiert. Die bevorzugten Konfigurationen wurden im industriellen Maßstab untersucht, wozu mehr als 1750 Versuchsschmelzen an einem 330 Tonnen Konverter durchgeführt wurden.

Mit dieser Forschungsarbeit wurden neue, modifizierte dimensionslose Kennahlen eingeführt (Fr^*_{LaSiP}, Eo^*_{LaSiP}, We^*_{LaSiP}, Q^*, und E^*). Es wurden die originalen Kenn-

zahlen mit zusätzlichen Parameter ergänzt, wodurch eine vollständige Ähnlichkeit zwischen Kaltmodell und Industrieanlage hergeleitet werden konnte. Zum ersten Mal wurden in einer Ähnlichkeitsstudie für das Design ein neues LD Kaltmodell angewandt, in dem die Wechselwirkung zwischen der Überschallströmung eine Mehrlochdüse, der Schlackenphasen und dem Bodenspülen abgebildet wurde.

Die in den Laborversuchen angewandten Methoden wurden aus der Literatur mit Modifikationen übernommen und es wurden auch neue entwickelt, um die Vermischungszeit, Stoffübergangsrate, Strahleindringtiefe sowie die Reaktionszone (Fläche und Steigung) im Kaltmodell der LD-Konverters zu ermitteln.

Die Experimente im industriellen Maßstab spielten eine wesentliche Role zur Validierung der Laborversuche. Diese lieferten Erkenntnisse für sieben verschiedene Bodenspülkonfigurationen.

Trotz des Einflusses vieler anderer Parameter und Variablen im industriellen Umfeld lieferten die durchgeführten Tests wesentliche Prozessdaten für die statistische Analyse durch maschinelles Lernen.

Acknowledgment

To finish all the steps necessary to conclude this PhD Thesis while working full-time on the BOF process, required me to resign my family's free time, required the comprehension and empathy of my supervisors, and generous support of friends, colleagues, partners and teammates.

Thank you...

... God, to provide me with all the health, chances, and wisdom to perform this work.

... my wife, Maria Paula, for your patience, partnership, support, and generously providing me all the time necessary at home, and taking care of our son Miguel. He was born at the same time I was dedicated to the PhD program. She could not be a more dedicated mother, and wife.

... my son, Miguel, to inspire me every day to keep walking.

... my parents, Maria Jose and Jose Quintella, to understand my absence in remarkable family moments.

... my brothers, Tatiane and Rodrigo, for the partnership, and to support our parents in all the time I was unavailable.

... my Professors, Johannes Schenk and Roberto Parreiras, you were fundamental to conclude this work. Despite all the priceless technical discussions, the most crucial aspect of this partnership was empathy to recognise the particular situation. I am so grateful for leading me with your humane touch.

... Professor, Johannes Schenk and MUL, to allow me to run this fantastic PhD project in two different continents.

... Professor Roberto Parreiras and UFMG, to provide me with the infrastructure, and the chance to run all the laboratory experiments at LaSiP.

... Ternium Brazil, my leaders, teammates, and technicians to support and empower me to perform this work in such a relevant industrial plant. It is unfair to cite some names because this work was possible due to the whole Steel Plant team's support.

... Dr Breno Totti, for your friendship and partnership to perform the trials and conduct the project at LaSiP, it would not be possible without your time and commitment.

... to all LaSiP interns teams, to execute the trials, perform the analysis, and added invaluable discussions to improve the experimental practices. Caio Diniz, Daniela Ladeira, Debora Silveira, Felipe Eliziario, Jose Arthur Guimaraes, Mariana Ribeiro, Raissa Sal-

gado, Raquel Souza, and Rubia Teodoro, you did great.

... Eng Marcos Viana, for your friendship, partnership, and invaluable support and insightful vision for advanced data analytics to evaluate the metallurgical results.

... Dr Bernardo Braga, for your generous contribution to the similarity analysis section.

... Eng. Gabriel Romeu, for your friendship and the generous contribution to translate the abstract to the German language.

... Eng Willian Lima, for your contribution to elaborate all drawings required for the project, and all the other discussions.

This work concludes one of the most exciting journeys of my life. I am so grateful to all of you that made this experience possible.

This work is dedicated to my wife Maria Paula, my son Miguel, my father Jose Quintella, and my mother Maria Jose.

Daniel Carvalho

Contents

List of Figures

List of Tables

Latim Nomenclature

Symbol	Description	Unit
V_W	Aqueous phase volume	$[m^3]$
A_{exit}	Area at the nozzle exit	$[m^2]$
A_{exit}/A^*	Area dimensionless ratio	$[-]$
H_{Bath}	Bath height	$[m]$
H_{BLD}	Bath level distance	$[m]$
H_{BOF}	BOF height	$[m]$
D_{BOF}	BOF diameter	$[m]$
Q_{gas}	Bottom stirring gas flow rate	$[m^3.s^{-1}]$
V_{bath}	Characteristic bath velocity	$[m.s^{-1}]$
D_{cm}	Cold model diameter	$[m]$
C'_W	Concentration at the water interface	$[mol.m^{-3}]$
$C^t_{CO_2}$	Concentration of CO_2 at a specific time	$[mol.m^{-3}]$
$C^{eq}_{CO_2}$	Concentration of CO_2 at the equilibrium	$[mol.m^{-3}]$
C_W	Concentration of caprylic acid in water	$[mol.m^{-3}]$
h	Concentration partition ratio $= \frac{c'_w}{c_o}$	$[-]$
d_{exit}	Diameter at the nozzle exit	$[m]$
C^*	Dimensionless concentration	$[-]$
Q^*	Dimensionless gas flow rate	$[-]$
P^*	Dimensionless jet penetration	$[-]$
L^*	Dimensionless light intensity	$[-]$
E^*	Dimensionless mixing energy	$[-]$

t	Elapsed time	$[s]$
K	Empirical constant	$[-]$
T_{EOB}	End of blow temperature	$[^{\circ}C]$
C_W^*	Equilibrium concentration of acid	$[mol.m^{-3}]$
C_f	Final concentration of tracer	$[mol.m^{-3}]$
Mn_{output}	Final manganese content measured in the steel sample	$[\%]$
P_{output}	Final phosphorus content measured in the steel sample	$[\%]$
Q_g	Gas flow rate	$[m^3.s^{-1}]$
Q_{tuyere}	Gas flow rate of the tuyere	$[m^3.s^{-1}]$
M	Gas molar mass	$[g.mol^{-1}]$
V_{tuyere}	Gas velocity at the tuyere exit	$[m.s^{-1}]$
g	Gravity acceleration	$[m.s^{-2}]$
C_p	Heat capacity at constant pressure	$[J.kg^{-1}.K^{-1}]$
C_v	Heat capacity at constant volume	$[J.kg^{-1}.K^{-1}]$
H_{BL}, H_{bath}	Height of static bath level	$[m]$
H_{SL}	Height of static slag level	$[m]$
D_{Ind}	Industrial BOF diameter (internal)	$[m]$
C_W^O	Initial aqueous solution concentration	$[mol.m^{-3}]$
$C_{CO_2}^i$	Initial concentration of CO_2	$[mol.m^{-3}]$
C_i	Initial concentration of tracer	$[mol.m^{-3}]$
L_i	Initial light intensity	$[cd.m^{-2}]$
Mn_{input}	Initial manganese content input from hot metal	$[\%]$
P_{input}	Initial phosphorus content input from hot metal	$[\%]$
d_{nozzle}	Inner diameter of the nozzle	$[m]$
C_W	Instant aqueous solution concentration	$[mol.m^{-3}]$
C	Instantaneous concentration of tracer	$[mol.m^{-3}]$
L	Instantaneous light intensity	$[cd.m^{-2}]$
D	Internal diameter of the transversal section of the nozzle	$[m]$

H	Jet length	$[m]$
P	Jet penetration	$[m]$
L	Length	$[m]$
L_f	Light intensity at the end of test	$[cd.m^{-2}]$
Ma	Mach number	$[-]$
W_{gas}	Mass of bottom stirring gas	$[kg]$
W_{slag}	Mass of static slag layer	$[kg]$
W_{bath}	Mass of static steel bath	$[kg]$
$K_{tm},\ k_W$	Mass transfer constants/coefficients	$[m.s^{-1}]$
Eo^*_{LaSiP}	Modified Eötvös number	$[-]$
Fr^*_{LaSiP}	Modified Froude number	$[-]$
$Re^*_{Meidani}$	Modified Reynolds number	$[-]$
We^*_{LaSiP}	Modified Weber number	$[-]$
n	Number of nozzles in lance tip	$[-]$
C_O	Organic phase concentration	$[mol.m^{-3}]$
V_O	Organic phase volume	$[m^3]$
L_P	Phosphorus partition ratio	$(\%P)/[\%P]$
P	Pressure	$[N.m^{-2}]$
P_{exit}/P_0	Pressure dimensionless ratio	$[-]$
P_{exit}	Pressure of gas jet at the nozzle exit	$[Pa]$
P_0	Pressure of gas jet at the throat	$[Pa]$
L_0	Quiescent bath level	$[m]$
r_x	Radius of "cavity" in the bath at the stagnant point	$[m]$
Fe_T	Slag oxidation	$[\%]$
V_s	Sound speed of gas at the nozzle exit	$[m.s^{-1}]$
$BLD,\ DBL$	Static bath level distance	$[m]$
T	Temperature	$[^\circ C]$
T_{exit}/T_0	Temperature dimensionless ratio	$[-]$

T_{exit}	Temperature of gas jet at the nozzle exit	$[K]$
T^*	Temperature of gas jet at the throat	$[K]$
t	Time	$[s]$
A_{exit}^{total}	Total area at the nozzle exit	$[m^2]$
Q_{exit}^{total}	Total gas flow rate	$[m^3.s^{-1}]$
L	Transport coefficient	$[m^3.s^{-1}]$
D_{tuyere}	Tuyere exit diameter	$[m]$
R	Universal gas constant	$[J.mol^{-1}.K^{-1}]$
V	Velocity	$[m.s^{-1}]$
V_{exit}	Velocity of gas jet at the nozzle exit	$[m.s^{-1}]$
V_{jet}	Velocity of gas jet under the nozzle exit along the jet axis	$[m.s^{-1}]$
V_{slag}	Volume of static slag layer	$[m^3]$
$V_{static.bath}$	Volume of static steel bath	$[m^3]$
V_w	Water volume	$[m^3]$

Greek Nomenclature

Symbol	Description	Unit
$\eta,\ \mu$	Dynamic viscosity	$[kg.m^{-1}.s^{-1}]$
η_{Mn}	Manganese oxidation	$[-]\ or\ [\%]$
$\eta_{Mn\,200}$	Mn oxidation levels at the inblow sample	$[-]\ or\ [\%]$
$\eta_{Mn\,210}$	Mn oxidation levels at the end of the blow (EOB)	$[-]\ or\ [\%]$
η_n	Efficiency factors	$[-]$
η_P	Dephosphorization degree	$[-]\ or\ [\%]$
$\eta_{P\,200}$	Dephosphorization degree at the inblow sample	$[-]\ or\ [\%]$
$\eta_{P\,210}$	Dephosphorization degree at the end of the blow (EOB)	$[-]\ or\ [\%]$
γ	Heat capacity ratio of the gas	$[-]$
λ	Scale factor	$[-]$
ν_{gas}	The speed of sound in the gas	$[m.s^{-1}]$
ν_s	Speed of sound	$[m.s^{-1}]$
ν	Cross-sectional mean velocity of gas in the nozzle	$[m.s^{-1}]$
ν	Kinematic viscosity	$[m^2.s^{-1}]$
$\overline{\nu_{gas}}$	Local gas velocity	$[m.s^{-1}]$
ρ_{bath}	Density of the bath	$[kg.m^{-3}]$
ρ_{exit}	Density of gas jet at the nozzle exit	$[kg.m^{-3}]$
ρ_{gas}	Density of the gas at the nozzle exit	$[kg.m^{-3}]$
ρ_{mix}	Density of the slag-metal mix	$[kg.m^{-3}]$
ρ_{slag}	Slag density	$[kg.m^{-3}]$
ρ_{steel}	Bath density	$[kg.m^{-3}]$

ρ^*	Density of gas jet at the throat	$[kg.m^{-3}]$
ρ	Density	$[kg.m^{-3}]$
σ_{slag}	Slag interfacial tension	$[N.m^{-1}]$
σ_{steel}	Liquid steel interfacial tension	$[N.m^{-1}]$
σ	Interfacial tension	$[N.m^{-1}]$
θ, θ_{nozzle}	Angle of individual nozzle	$[°]$
ε^0_{bottom}	Mixing energy due to bottom stirring	$[W.t^{-1}]$
$\varepsilon^0_{decarburization}$	Mixing energy due to decarburization	$[W.t^{-1}]$
ε^0_{top}	Mixing energy due to top lance	$[W.t^{-1}]$
ε^0_{total}	Total mixing energy	$[W.t^{-1}]$

Abbreviations

AOD   Argon Oxygen Decarburization

BF   Blast Furnace

BLD   Bath Level Distance

BOF   Basic Oxygen Furnace

BOP   Basic Oxygen Processes

BR   Brazil

CCM   Continuous Casting Machine

CFD   Computational Fluid Dynamics

CSA   Companhia Siderúrgica do Atlântico

DBL   Bath Level Distance

DRI   Direct Reduced Iron

EAF   Electric Arc Furnace

EOB   End Of Blow

GBM   Gradient Boosting Machine

HM   Hot Metal

HMD   Hot Metal Dessulphurization

K-BOP Kawasaki - Basic Oxygen Process

KOBM Klöckner Oxygen Bottom Maxhütte

LaSiP   Process Simulation Laboratory

LD   Linz-Donawitz Converter

LD-BS Linz-Donawitz Bottom Stirring

LD-KG LD Kawasaki Gas Stirring

LD-OB Linz-Donawitz Oxygen Bottom

LED Light Emitting Diode

LOMAS Low Maintenance Gas Analyzing System

LTS Ladle Treatment Stirring

LWS Loire-Wendel-Sprunck

MHP Multiple Hole Plugs

OBM Oxygen Bodenblasen Maxhuette or Oxygen Bottom Blowing Furnace

PCD Pitch Circle Diameter

PIV Particle Image Velocimetry

Q-BOP Quick - Basic Oxygen Processes

RH Vacuum Degasser

SHAP SHapley Additive exPlanations

SHP Single Hole Plug

TBM Thyssen Blowing Metallurgy

UFMG Universidade Federal de Minas Gerais

WP Work Package

1 Introduction

Before World War II, Robert Durrer set the fundamental theoretical principles and encouraged VÖEST to blow the oxygen directly over the melt in a separate vessel. From 1909 to 1948, scientists talked about and later attempted to use oxygen to make steel and to improve the existing steelmaking processes. The discovery of Linde-Fraenkel's process in 1928 for large scale production of oxygen and the start-up of tonnage oxygen generating equipment from 1931 to 1933 in integrated steel plants in Germany inspired more experiments and gave steelmakers the cheap oxygen they needed [1].

After a series of experiments using a $2\ t$ experimental converter, the LD process was born in 1949 in Linz, Austria. After suffering numerous primary misfortunes, a step forward was taken as early as June 25th, 1949; the LD process was born at this moment. The experimental operations remained until the production of several heats of $2\ t$, after which they changed to a specially constructed $15\ t$ experimental converter. VÖEST developed the LD process industrial-scale maturity in Linz and ÖAMG in Donawitz, and LD is the abbreviation for the Linz-Donawitz. In 1952, the first industrial LD vessel was commissioned in Linz and the second one in 1953 in Donawitz [2].

Fast growth for the Basic Oxygen Processes (BOP) was observed in the 1960s. By 1971, Basic Oxygen Furnace (BOF) was making more than half of the world's steel. This new technology started to challenge open-hearth steelmaking in the USA. This new technology replaced the Bessemer process in the USA by 1969, while the open hearth (Siemens-Martin) process survived to a smaller extent in a minor way in that country until 1991 [3].

The LD process led worldwide steel production to increase from 0.2 to 1.8 billion metric tons of crude steel per year, Figure 1.1 [4]. The new process brings the possibility to satisfy severe applications and the production of higher added-value products. Moreover, the steel produced from the LD process may be 100% recycled, and it is the unique alloy that maintains its property without quality loss. In other words, scrap can produce high-quality steel [2]. The LD process, also identified as a Basic Oxygen Furnace (BOF), because of the type of additives, and the refractory applied in their processes [5].
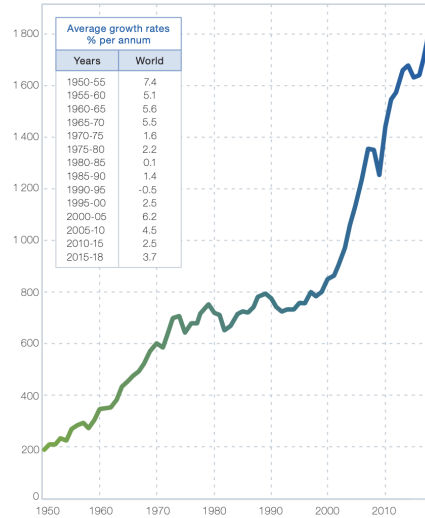
Figure 1.1: World crude steel production (million tons) [4].

Steel production is based mainly on two production routes, the Electric Arc Furnace (EAF) and the Blast Furnace-Basic Oxygen furnace (BF-BOF) route. Figure 1.2 shows the diversification and combinations of existing routes of steel production. Steel production in the BF-BOF route is based on raw materials such as coal, iron ore, burnt lime, and different scraps. EAF technology uses steel scrap and electricity for melting. According to the availability of steel scrap and the plant configuration, direct-reduced iron (DRI) or hot metal (HM) can also be used as metallic iron sources [6]. The integrated steelmaking route based on the BF-BOF is directly responsible for 70% of total world steel production [4].
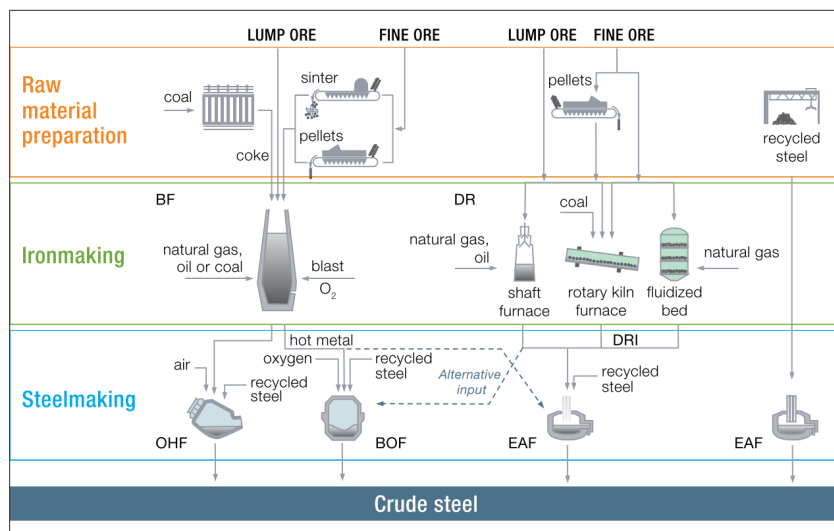
Figure 1.2: Steelmaking routes [6].

Figure 1.3 shows the historical and the forecast of crude steel production by route based on the past tendency. At least up until 2050, primary steelmaking based on the BOF technology is assumed to continue the main process route [7].
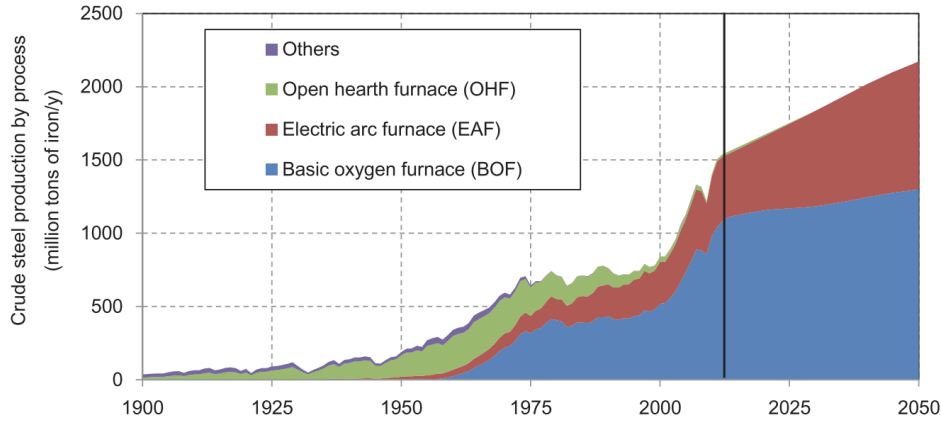
Figure 1.3: World crude steel production by process (million tons) [7].

1.1 BOF process and variations

In the beginning of the BOF process, mixing of steel bath was based solely on a top lance through the injection of pure oxygen, an insufficient mixing of the steel bath was encountered, which led to problems for a further increase in productivity and steel output [8]. Aiming to overcome this problem, the development of LD converters combining the bottom blowing technology existing in the Bessemer's converter started in the 1970s. A diverse range of technology with different process variations started up at that time. These technologies consist of the injection of oxygen, nitrogen, argon, carbon dioxide, and lime through the bottom, each technology with their specific variations [9].

Bottom stirring means the injection of inert gases through the bottom of the BOF vessel under the melt. The main task is to improve the interaction between the melt and the slag; the bottom stirring itself is not directly associated with chemical reaction. On the other hand, bottom blowing involves the oxygen injection, especially with fluidized lime or in addition to hydrocarbon-based fuels such as fuel oil, natural gas, or pulverized coke, and all conveyed in the equivalent method to launch reactions in the steel melt [10]. A general classification of BOF vessels is presented in Figure 1.5 the BOF installations processes range from 'top blowing only' to 'bottom blowing only' including many combined process standards [11].

Lance tip and nozzle design have been a critical issue to the operation of modern BOF plants, the use of a single hole lance took place in the first years of the BOF process between 1952 and 1963, the heat size typically being between 20 to 40 t. It was observed that the process was controllable up to heat sizes of 50 t, but for higher heat sizes, blowing problems increased considerably, even when significant lance distances to the metal bath were adjusted. The metallurgical and especially the processing difficulties (slopping, converter mouth, and hood skulls) were so dramatic that it could limit the expansion of the BOF process for a larger production scale [12].
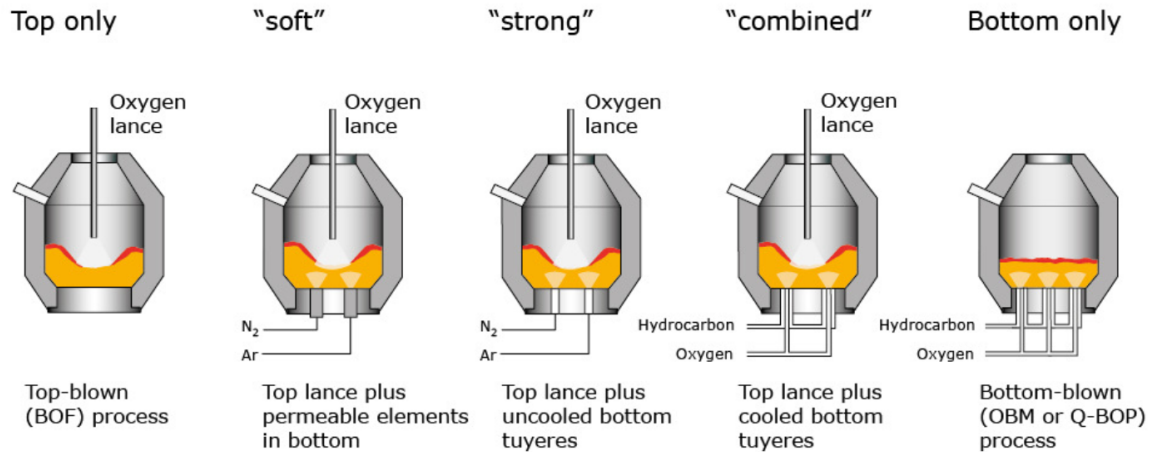
Figure 1.4: General BOF vessel classifications [11].

In 1962, the use of a multiple hole lance tip was demonstrated at the Yawata Iron and Steel Co. It was noted the three-hole lance tip, with an inclination of the nozzles to the longitudinal lance axis, creating an unusually calm blowing characteristic. Since then, the multiple hole lance has been developed, mainly depending on the vessel dimensions and the desired oxygen flow rates [12].

1.2 Process Modeling

Measuring the fluid flow characteristics in a real process is nonviable due to natural conditions related to the metallurgical process, such as high-temperature and opacity. Additionally, model experiments based on molten metals, precisely like the real process, are usually awkward. When heat and mass transfer, and chemical reactions co-occur, the situation is complicated faraway [13]. Considering these complex and severe conditions plus the operational costs, experimental investigations on the real process is very challenging. In this way, modelling is a valuable tool for fluid flow phenomena.

Generally, the modelling is classified in physical and mathematical categories, and both approaches are complementary [14, 15, 13]. Mathematical modelling suggests the use of a combination of differential or algebraic equations to describe the fluid flow and correlated the real process heat and mass transfer. These models rely on the fundamentals of chemistry, physics, fluid, and solid mechanics [13]. Usually, physical modelling is employed to describe a system to be modelled by changing the factors to be handled and the scale of the operation to achieve a practical process description. However, at the same time, to enable the measurements to be executed more conveniently and cost-effectively. Water usually is employed to simulate the liquid steel, due to its kinematic viscosity approximately equal to that of liquid steel [15].

Szekely and Ilegbusi [15] mentioned that the fluid flow problems encountered in metal processing were too complicated to rely on predictions based on mathematical modelling.

Nevertheless, in more recent literature, Iguchi and Ilegbusi [13] mentioned that mathematical modelling has become widely applied in engineering and science practice, due to the current progress in computer processing hardware and developments in numerical computation methods. The authors also mention that the exact equations for governing phase flows are still missing for the multiphase flow (gas-liquid-solid) systems, which includes the BOF. To describe the fluid flow vectors, the development of a combination of simplified or approximated governing equations is necessary.

Odenthal et al. [16] developed a converter model based on CFD fluid simulation software, and they considered various fluid dynamic characters, such as the slag-melt-gas phases interaction, the melt cavities generation, and the refractory lining heat transfer. A single CFD model can integrate numerical and mathematical models, such as kinetics reaction models. Nevertheless, the computational requirements to determine the system of equations becomes so large that there is no rational balance between costs and benefits. They developed an integrated CFD model to simulate around 20 to 30 seconds of a combined blowing converter; longer process times could not be implemented due to limited computer capacities, but in general, the simulation is possible [17, 18].
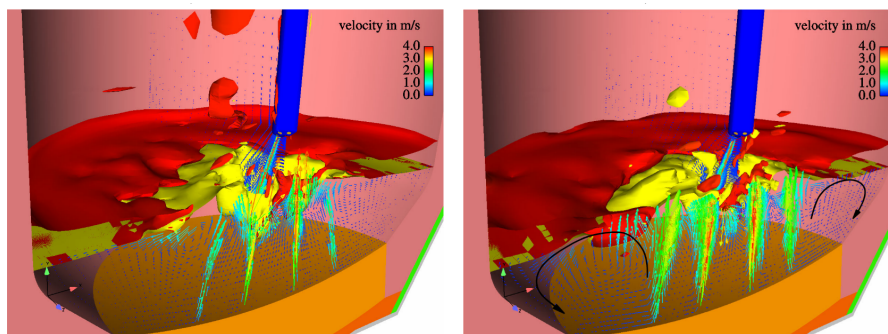
Figure 1.5: CFD multi phase simulation 335 t BOF with six hole top lance [16].

The advantage of the water model test is that a large number of trials can be completed in a brief time, granting the observer a lot of informative data, enhancing the knowledge of physical phenomena involved in metallurgy problems. Nevertheless, all the modelling criteria can not be fulfilled at the same time. Consequently, it is desirable to compare theoretical predictions with direct measurements or to formulate an overall strategy where experiments and theoretical analysis complement each other [15].

Experiments in industrial plants can be very costly and risky because of many reasons such as interference in the operational routine, productivity losses, risk of accidents due to new practices, and new materials still not tested as well losses on the quality of the final products [19]. Modelling is a well-established scientific technique to reduce these impacts, widely applied to process developments [20]. These models, in general, are built to scale, adopting similarity principles between the model and prototype and using materials at ambient temperatures like water in the place of liquid metal, which kinematic viscosity of the liquids are nearly equal. On the other hand, oil can simulate slag for multiphase

simulations [20].

While a complete and quantitative understanding of the detailed process mechanism has not been reached, the fluid flow theory, coupled with physical modelling experiments, has been an essential tool for process metallurgy improvements [14].

1.3 Motivation of the present work

In an earlier work about lime dissolution and slag formation for an industrial 330 t BOF at Ternium BR [5], the same process as presented in this thesis, several process parameters were studied, and a sensitivity analysis was developed. Fundamental relations between thermodynamics and kinetics were established to describe the process. Essential results for specific process knowledge and further industrial improvements were delivered. Nevertheless, a weak point for the model was the efficiency factors that correlate the mixing energy related to top lance, bottom stirring, and decarburization reactions. The stirring power of the gas introduced into the converter and the gas, which evolves in the form of carbon monoxide bubbles, not only brings about mixing but also has a direct effect on the time constants of the refining reactions [21].

A couple of different reports for the agitation of a top blowing jet to the bath and bottom stirring are available in the literature, and different expressions to calculate the agitation power have been proposed [22, 23, 24, 25, 26, 27, 28, 29]. Although experimental conditions from each are used, these empirical assumptions are not necessarily suitable for all BOF processes. The concept of the mixing time is perfect for an assessment of the system performance [15].

Numerous parameters are connected to the BOF refining process. Developments concerning the blowing pattern (Bath Level Distance - BLD, and oxygen flow rate), the design of the lance tip (nozzle number and angle), and bottom stirring structure (design and gas flow rate of each tuyere) are essential for the manufacturing system. Those parameters have a substantial impact on the steel process productivity, costs, and quality [30].

The primary objective of this thesis is to develop an investigation about the improvement of the mixing time and mass transfer rate due to a gradient of apparent density caused by different bottom stirring flow zone.

A development of experimental simulation, based on a physical laboratory modelling, in the conditions similar to the converter steelmaking technology, has been conducted at UFMG (Universidade de Federal Minas Gerais) to investigate this proposal. With the task to compare the metallurgical results, tests in an industrial 330 t BOF have been carried out at Ternium Brazil (former thyssenkrupp CSA), plant in Santa Cruz, Rio de Janeiro, Brazil.

2 Fundamentals and Literature Review

The oxygen lance position and flow control have a dominant role in the BOF process. The bath level distance is an empirical agreement among performing faster decarburization and proper slag formation [10]. The inert gas injection through the converter bottom stirring, combined with the top lance oxygen blowing, promotes a more significant metallic bath mixing. It also enhances the refining reactions based on mass transfer, such as decarburization, dephosphorization, and manganese oxidation. Besides, the bottom stirring allows lower chemical stagnation areas and improved metallurgical results [30].

In the BOF process, all the reactions related to oxidation-reduction co-occur, according to their driving force, and reach a coupled equilibrium in competition at the bubble-liquid interfaces [31]. The driving force is strongly connected to the efficiency of the bath mixing, which is determined by the top blowing lance and bottom stirring parameters, as well as the melt conditions.

Numerous publications have investigated the bath mixing efficiency for the BOF process, and the fundamental understanding of the BOF process is well known. Mathematical equations have been developed to describe the effects of process parameters effects on the mixing efficiency. However, these equations consider empiric adjustments to fit the industrial with the theoretical or simulated data. Most of these equations describe a specific operation and may not be valid for quantitative analysis. Cold modelling studies that consider the individual characteristics of each process are frequently applied to define the quantitative mixing performance for an industrial process.

2.1 BOF Fundamentals

In the BOF process, solid particles and droplets are distributed in the melt, and it occurs by emulsification, with both slag droplets being emulsified in steel melts and steel droplets being emulsified in slags [21]. The flow of the oxygen jet generates a basin on the bath surface, circled by a wave peak. In this slag free cavity, the oxygen jet reacts directly with the liquid metal inside the vessel, and the emulsification occurs as a result of the breakaway of metal droplets from the upwardly flowing liquid at the upper edge of the penetration cavity produced by the oxygen jet, Figure 2.1. The slag frothed into an emulsion produced by the CO bubbles created inside the metal bath by the oxidized metal droplets sinking back into the bath or by the metal droplets oxidized in the high

$\%FeO$ containing slag foam phase [32].
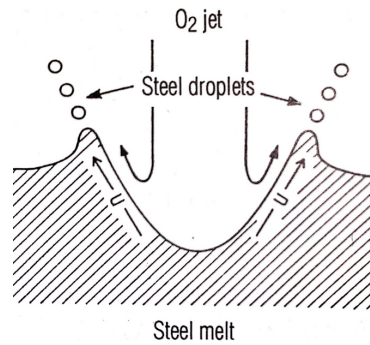
Figure 2.1: The principles of emulsification of steel droplets in the BOF process [21].

The mathematical model approach developed by Carvalho [5] for the BOF process, is based on the assumption that the blown oxygen oxidizes C, Si, and Mn in the steel and Fe as a matrix. However, the FeO formed is also an oxidant of C, Si, and Mn in the steel, Figure 2.2. At high carbon contents, it is assumed that the supplied oxygen determines the oxidation rates of elements according to thermodynamic rules. It is also assumed for low carbon levels, a decarburization rate primarily defined by carbon mass transfer from the steel bath to the reaction interfaces.
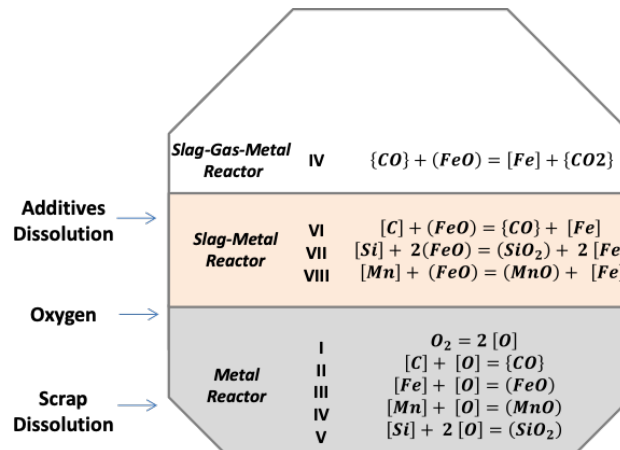
Figure 2.2: Schematic representation of the BOF reactions [5]

2.1.1 BOF Blowing Profile

On the steelmaking shop floor, the terms soft and hard blowing usually define the oxygen blowing pattern, these generic terms are related to the Bath Level Distance (BLD), which is the length between the lance tip and the steel bath in the static position. If all parameters are the same, in the same process, the hard blow has a lower BLD than the soft blow.

When the oxygen is injected deep into the bath, also known as hard blow, the proportion of oxygen reacting with the carbon is considerable, and CO bubbles are formed low down in the metal melt, the stirring effect of the CO is correspondingly intense [21].

In intense hard blow practice, a poor slag formation with low slag oxidation is faced, and problems are observed for phosphorus removal and skull formation in the system.

On the other hand, in a soft blow, the oxygen is injected at shallow depths, the rate of decarburization is reduced, and only a minor degree of stirring takes place [21]. If the adjustment is not well coordinated, the slag is over-oxidized, and a higher slag volume observed, increasing the chance of sloping.

The first step of the blowing pattern usually has a significant BLD, to avoid the possibility of the lance nozzle tip having contact with the scrap and to establish the oxidizing, heat-generating reactions safely. After this first step, a soft blow is still required to enhance the reaction rate and control the first slag generation, and this step provides some early iron oxide to develop suitable slag formation. The more prolonged and principal stage, where most of the reactions take place, is known as the main decarburization period [10] and usually requires a blowing practice harder than the first steps. Figure 2.3 shows different blowing patterns applied in different plants [32].

The carbon removal rate is managed by rising the jet force along the path to the end of the blow, where the rate quickly drops. At this point, the dynamic models start calculations based on sublance measurements and off-gas analysis to define the precise end-of-blow point according to the production aims (e.g., C, T, P, and slag activity) [10].
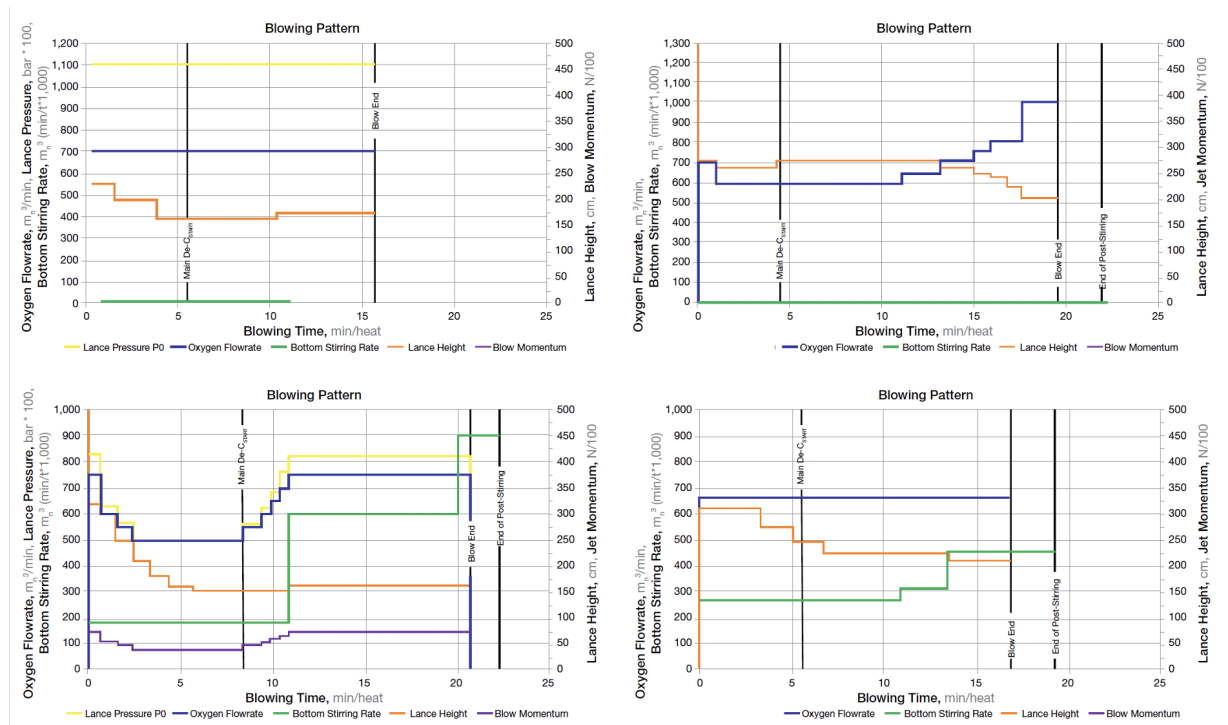
Figure 2.3: Typical blowing profiles from different plants [32].

2.1.2 Bottom Stirring

The development of the bottom blown converter (OBM, LWS) in West Germany and France in 1968 attracted many investigators to study the relation between mixing energy and metallurgical characteristics. Intensive development of converter operating technology took place in the mid-seventies, studies regarding the improvement of top blown converter refining efficiency were performed based on bottom blowing or bottom stirring technology [33].

In 1963, Nippon Steel experimentally proved enhanced dephosphorization reactions by blowing an inert gas into the molten steel bath in the top blown converter [34]. They also developed various water modelling experiments starting in 1977 to study the conditions for bottom blowing-stirring and the improvement of mixing conditions, and their first 75 t industrial trials were in 1978 at Yawata Works [33].

At the beginning of 80s, several European and Japanese steel plants reported the implementation of some bottom stirring-blowing technology in their LD process; Thyssen AG, Krupp Stahl AG, Kloeckner Maxhuette, Mannesmann, Arbed-Irsid, CRM, Nippon Steel, Kawasaki, Sumitomo, Kobe, NKK, Solmer [35, 36, 37, 38, 39, 40, 41, 42]. A few companies in the USA reported these developments at that time: Indiana Harbour and US Steel [43, 44]. Hoogoven and British Steel started their developments later in the 80s [45]. Since then, bottom stirring technology has become very popular, Figure 2.4, shows the variety and share of oxygen steelmaking processes technology applied worldwide in 2011 [46]. The process abbreviations are related to the historical background and, in some cases, are linked to their first commercial names. The OBM means Oxygen Bottom Maxhütte, KOBM denotes Klöckner Oxygen Bottom Maxhütte, and the LD, LD-OB, and LD-BS are the well known Linz-Donawitz process with their variations such as Oxygen Bottom and Bottom Stirring respectively.
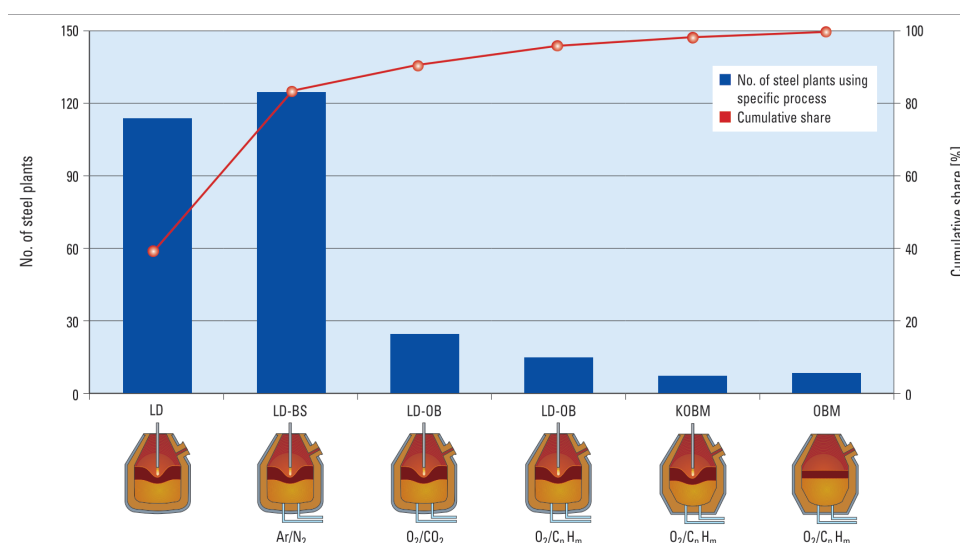
Figure 2.4: Worldwide oxygen steelmaking processes variations and share of each technology application - reference year 2011 [46].

The intense mixing effect introduced by bottom stirring implies a less dependent mixing process on the *CO* influence as the bath stirring engine than in cases where there is no bottom stirring, and also the overall degree of mixing is much more intensive. Consequently, the reaction equilibria in the converter are more easily achieved than in the case of the top-blowing process alone [21]. Figure 2.5, shows the mixing times in converters as a function of the specific flow rate of the gas injected through the bottom for various industrial processes [47]. In the case of the LD process (top left), oxygen is blown exclusively from above, while the OBM process (bottom right), oxygen is only injected from below. The other fields indicate various types of the combined blowing process, involving in some cases oxygen when bottom blowing technology is adopted, and inert gas in case of bottom stirring technology [21].
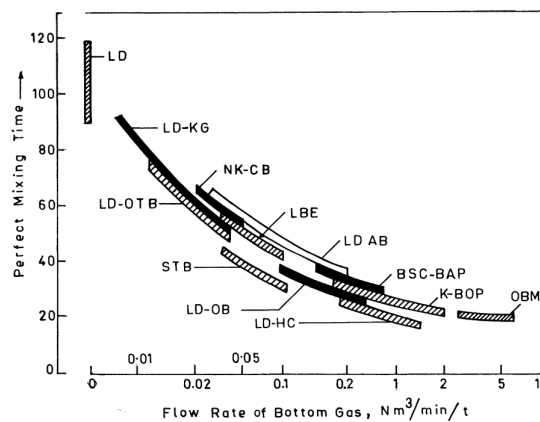
Figure 2.5: Effect of bottom gas flow rate on mixing time for various converter technologies [47].

The gas purging system influences the equilibrium conditions in the steel bath by enhancing the refining process mixing time, and this condition enables the system to approach the equilibrium at the end of blowing. Decarburization and dephosphorization are considerably improved, several reports are available showing the industrial benefits. Table 2.1 shows typical metallurgical results for both BOF technologies [35, 36, 37, 38, 39, 40, 41, 43, 44, 42, 45, 48, 49, 50, 51, 52, 53, 54, 11, 55, 56].

Bottom stirring also plays an essential role in the additives dissolution, the increase in gas flow rate gives a higher mass transfer rate over the main oxygen blow process, resulting in a lower undissolved additives quantities at the end of the process. Nevertheless, further increases in the bottom-stirring gas flow rate produce no more than a slight marginal improvement in this effect, Figure 2.6 [5].

One important metallurgical performance indicator for the BOF process usually is defined by the carbon and oxygen product ($[\%C][ppmO]$) in the final steel. To minimize the consumption of deoxidation elements (e.g., Al), slag iron losses, and the BOF lining wear, a high oxidation level in the process must be avoided. Figure 2.7, exhibits a comparison between BOF steelmaking operations with and without bottom stirring.

Usually, there are three different bottom gas purging technologies available, the tuy-

Table 2.1: Typical BOF metallurgical results [57].

Parameter	Top Blowing	Bottom Stirring	Unit	Reference
Iron Content in Slag	20-23	15-18	%	[57]
$[C]$ at the end of blow	>400	300-400	ppm	[46]
$[O]$ at the end of blow	>650	500-650	ppm	[46]
Carbon Oxygen Product	30-35	22-25	$[\%C][ppmO]$	[57]
Phosphorus Distribution	30-50	70-110	$(\%P)/[\%P]$	[57]
Manganese Yield	20-30	40-50	%	[57]
Al deox. comsumption	>2	1.5-2	kg/t	[46]
Reblow Rate	>18	10-18	%	[46]
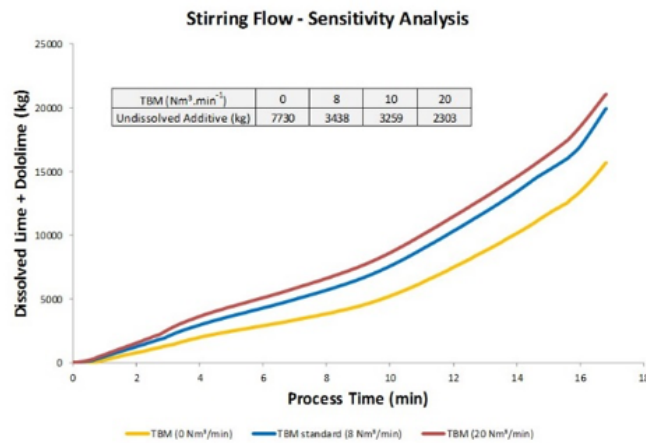
Figure 2.6: Additives dissolution and bottom stirring flow rate [5].

eres and the Single (SHP) and Multiple Hole Plugs (MHP), Figure 2.9. The MHP is primarily chosen by steel plants using BOF bottom gas stirring technology.

The MHP technology is usually described by the reduced probability of steel infiltration and a weaker gas flow interruption potential, and this technology is recommended because the plug can be reestablished throughout the lining campaign, which brings improved stirring plug availability. The tuyeres technology has a similar function of SHP, and steel plants operating with the tuyere technology have the chance to drill and install new tuyeres through the lining campaign. Steel plants that operate on the tuyere philosophy have the opportunity to drill and set new tuyeres during a campaign. Usually, 8 to 13 purging plugs are installed per vessel; an overview of the different purging plug characteristics is provided in Figure 2.8 [46].

Typically, lower levels of carbon and oxygen product ($[\%C][ppmO]$) are achieved with MHPs when compared to steel plants operating with SHPs and tuyeres. Average results obtained with different purging plug types are shown in Figure 2.10 [46]. These results are related to the increased plug blocking potential during the campaign for SHP and
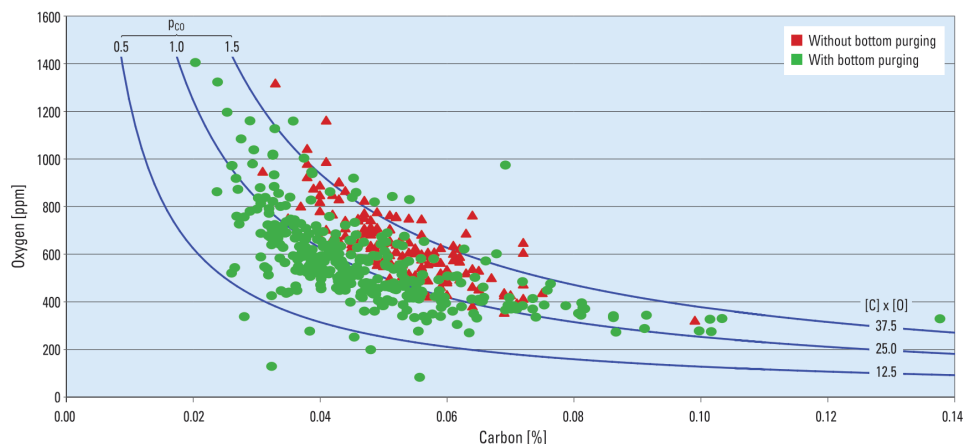
Figure 2.7: Comparison of carbon and oxygen content at the end of blowing with and without bottom gas purging [46].

Parameter	MHP	SHP	Tuyere
Relative price	Medium	Low	High
Bubble characteristics	Well distributed small bubbles	Ineffectively distributed large bubbles	Ineffectively distributed large bubbles
Breakthrough safety	High	Low	Low
Blocking	Likely to reopen	Likely to remain blocked	Likely to reopen
Average flow rate range per plug (l/min)	200–1400	200–1200	2000–3500
Average total flow rate consumption per heat (Nm³/t)	0.8–1.2	0.8–1.2	> 1.5
Average pipe diameter range (mm)	1–2	4–8	1.5–3.8
Number of pipes per plug	12, 24, 32	1	1
Open gas section per plug (mm²)	9.4–100.5	12.6–50.3	100–120
Average wear rate (mm/heat)	0.40	0.42	0.40–0.45
Number of plugs per vessel	8–12	8–13	3–4
Additional information	>> Less plug blocking potential >> Less infiltration affinity >> Reopening during a campaign (purging availability increased) >> Installation during relining procedure	>> Economically priced >> Increased plug blocking potential during a campaign >> Installation during the relining procedure	>> Defined drilling positions >> Complicated installation procedure >> Installation during campaign startup period >> No purging availability at campaign start (installation after 50–100 lining heats) >> Poor bath agitation caused by very high flow rates (jetting)

Figure 2.8: Characteristics of MHP's, SHPs, and tuyeres [46].

Tuyere plug technology, which reduces the metallurgical performance.

Bottom stirring design and pattern are essential for the BOF process and the metallurgical results. Parameters related to bottom stirring design such as the number, arrangement, and type of bottom stirring elements and others related to the bottom stirring pattern such as the gas flow rate, type, and quality of inert gas (Ar, N_2) and inert gas shifting points must be rigorously coordinated. Otherwise, the process becomes uncontrolled, and the metallurgical results cannot be achieved [58].
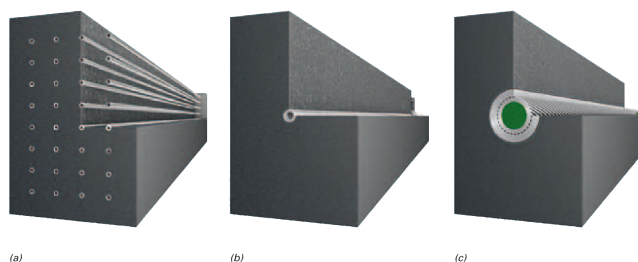
Figure 2.9: Common purging plug types: (a) MHP, (b) SHP, and (c) Tuyere [46].
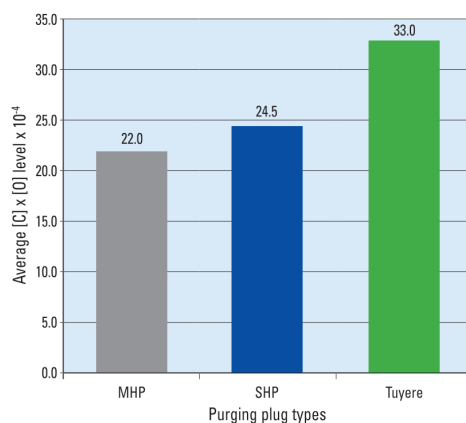
Figure 2.10: Average $[C]x[O]$ levels achieved with different bottom stirring technologies [46].

2.2 BOF Mixing Efficiency

The mixing efficiency plays an essential role in the driving force of the BOF reactions, and the mixing time is widely applied to calculate the metal circulation and the efficiency of the bath mixing, the mixing time decreases with the increase of the mixing energy. The stirring energy equations available in the literature adopt empirical adjustments and specific assumptions, making it necessary to introduce the jet momentum and the energy balance.

2.2.1 Mixing Time

Mixing has considerable importance due to the high reaction rate in the BOF process. The carbon monoxide (CO) reaction is the most important bath stirrer, and this reaction is controlled by the quantity of oxygen injected through the melt. Top blowing combined with bottom stirring enhances the stirring effect, and relatively small amounts of bottom stirring gas are sufficient to cause vigorous stirring. At the same time, increases in the bottom-stirring gas flow rate produce no more than a slight marginal improvement in this effect [21].

Mixing energy considers the stirring effects of all the gases involved, Equation 2.1 [28], including the CO which is formed within the bath. The expansion work of the gases is expressed by the terms of the expansion work caused by the decrease in pressure as the

gas bubbles rise, and the thermal expansion work of the injected or top-blown gases. The stirring power of the gas introduced into the converter and the gas, which evolves in the form of CO bubbles, not only brings about mixing but also has a direct effect on the time constants of the refining reactions, Figure 2.11 [21].

$$\varepsilon_{total}^0 = \eta_1.\varepsilon_{top}^0 + \eta_2.\varepsilon_{bottom}^0 + \eta_3.\varepsilon_{decarburization}^0 \qquad (2.1)$$

Where, ε_{total}^0 – total mixing energy $(W.t^{-1})$, ε_{top}^0 – mixing energy due to top lance $(W.t^{-1})$, ε_{bottom}^0 – mixing energy due to bottom stirring $(W.t^{-1})$ and $\varepsilon_{decarburization}^0$ – mixing energy due to decarburization $(W.t^{-1})$ and η_n – efficiency factors $(-)$.

The mixing power of bottom stirring ε_{bottom}^0 was estimated as the sum of buoyance power $\varepsilon_{buoyance\ power}^0$, expansion power $\varepsilon_{expansion\ power}^0$ and kinetic energy $\varepsilon_{kinetic\ energy}^0$ [28].
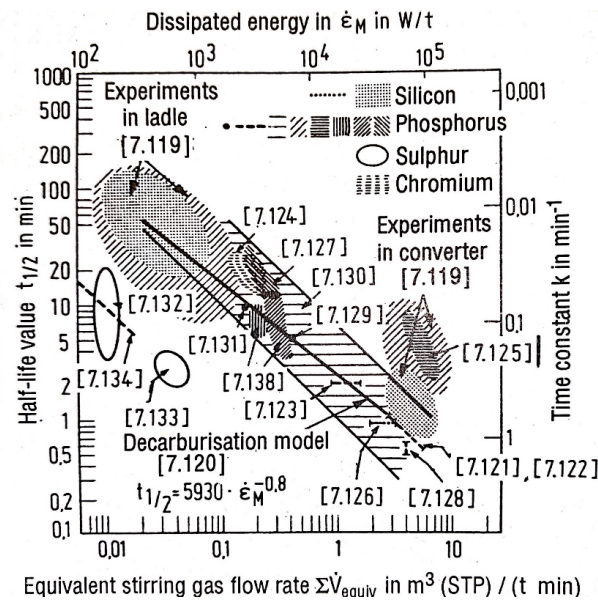
Figure 2.11: BOF refining reactions mixing time as a function of the equivalent stirring gas flow rate [21].

An analysis of the metal component of the slag-metal emulsion in different heights did not show significant chemical differences at any stage in the blow. This analysis is a significant result because it shows that the high level of mixing and turbulence in the slag-metal emulsion limits the local chemical content differences. A comparison between the metal droplets in emulsion and the bulk metal was also made. It was clear that the metal droplets in emulsion play an essential task in the BOF chemical reactions. The amount of ejected droplets is related to the dynamic impact of the lance jet on the metal bath surface [59].

The considerable reduction in mixing time values, which occurs as stirring power increases, is due mainly to the higher degree of emulsification, explained by the emulsion-metallurgical reaction description proposed by Oeters [21].

In the case of scrap melting, the diffusive scrap melting and the forced scrap melting

mechanisms must be considered. The diffusive scrap melting model considers the specific mixing energy to calculate the mass transfer coefficients of the metal phase. The mixing energy is generated in the metal bath as a consequence of top blowing and the bottom stirring, when available. The specific mixing power is also applied for the calculation of the heat transfer coefficient in the metal phase in the forced scrap melting mechanism [60]. In a comprehensive review of steel scrap melting in molten iron-carbon melts, Penz and Schenk [61] mention the influence of dissolution and melting behaviour of scrap in the whole BOF process cycle. They also found the heat transfer coefficient of the liquid phase intrinsically related to the bath mixing energy.

Mixing energy also has a critical role in slag formation, and additives dissolution [5], mass transfer coefficients for lime, and dolomitic lime can be estimated by a relationship based on Sherwood and Schmidt numbers [62]. According to Oeters [21], the turbulent mass transfer to solid particles in the metallurgical system can be related to stirring power input.

2.2.2 Jet Momentum and Energy Balance

According to Szekely and Themelis [63], when the oxygen jet reaches the liquid surface, a cavity is formed on the bath surface surrounded by a wave crest, Figure 2.12, and the the gas jet transfers momentum, which generates the bath movement. The cavity depth correlates with the jet momentum through an energy balance according to Equation 2.2.
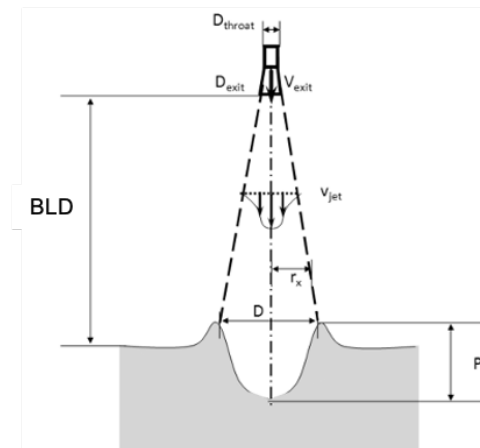
Figure 2.12: Simplified jet penetration model [64].

$$\frac{1}{2} \cdot \rho_{gas} \cdot V_{jet}^2 = g \cdot \rho_{steel} \cdot P + \frac{2 \cdot \sigma_{steel}}{r_x} \tag{2.2}$$

$$V_{jet} = \frac{V_{exit} \cdot K \cdot d_{exit}}{H} \tag{2.3}$$

Meidani et al. [65] performed experiments through a cold model for different designs of supersonic oxygen lance tip, including single central hole and auxiliary nozzles, and

defined the jet penetration according to Equation 2.4.

$$\frac{\pi}{2.K^2}.\frac{P}{BLD}.\left(1 + \frac{P}{BLD}\right)^2 = \frac{\pi.\rho_{gas}.V_{exit}^2.d_{exit}^2}{4.\rho_{steel}.g.BLD^3} \tag{2.4}$$

Alam [66] introduced in the Equation 2.5, the angle between the bath and the injectors for a single nozzle lance in the EAF process, Figure 2.13.
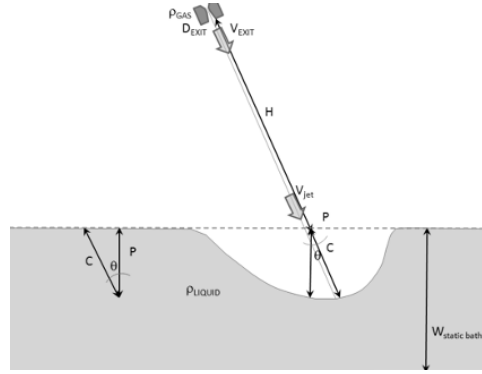
Figure 2.13: Schematic jet model considering the angle and single nozzle for EAF injectors [66].

$$\frac{\pi}{2.K^2}.\frac{P}{H}.\left(1 + \frac{P}{H.cos\theta}\right)^2 = \frac{\pi.\rho_{gas}.V_{exit}^2.d_{exit}^2.cos\theta}{4.\rho_{steel}.g.H^3} \tag{2.5}$$

Maia and Tavares [67] developed a cold modelling study for the BOF process considering the multi-nozzle supersonic lance. Based on previous investigations, the author introduced a new term related to the number of nozzles, Equation 2.6.

$$\frac{2}{K^2}.\frac{P}{BLD}.\left(1 + \frac{P}{BLD.cos\theta}\right)^2 = \frac{\pi.\rho_{gas}.V_{exit}^2.d_{exit}^2.cos\theta.n}{4.\rho_{steel}.g.BLD^3} \tag{2.6}$$

All previous equations, calculated the penetration index based on a static bath level. However, in the BOF operation, the bath level is dynamic [32]. In a recent cold modelling study, Maia et al. [64] introduced new parameters in the previous equations to include the effects of the bottom stirring parameters in a multi-phase bath, Figure 2.14, and included the term related to the surface tension, considering the steel and slag phase, Equation 2.7.

$$\frac{1}{K^2}.\left(\frac{\pi}{2}.\frac{P}{(BLD + P)}\right).\left(1 + \frac{1}{P^2}.\frac{cos\theta.(\sigma_{steel} + \sigma_{slag})}{(\rho_{steel} + \rho_{slag}).g}\right) = \left(\frac{\pi}{4}.\frac{\rho_{gas}.V_{exit}^2.d_{exit}^2.cos\theta^2.n}{(\rho_{steel} + \rho_{slag}).g.(BLD + P)^3}\right) \tag{2.7}$$

The concept of mix density is introduced, Equation 2.8, and considers the influence of the gas hold up due to the bottom stirring gas flow rate when Ar/N_2 bubbles are injected into the melt, the bubbles decrease the density of the melt, and as a consequence, increase
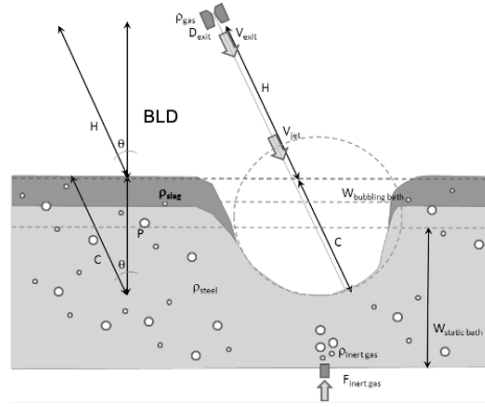
Figure 2.14: Jet penetration model considering gas hold-up and slag phase for BOF operations [64].

bath height.

$$\rho_{steel} + \rho_{slag} \simeq \rho_{mix} \simeq \frac{W_{gas} + W_{bath} + W_{slag}}{V_{gas} + V_{static.bath} + V_{slag}} \tag{2.8}$$

Where, ρ_{gas} – density of the gas at the nozzle exit ($kg.m^{-3}$), V_{jet} – velocity of gas jet under the nozzle exit along the jet axis ($m.s^{-1}$), g – gravity acceleration ($m.s^{-2}$), P – jet "cavity" penetration (m), σ_{steel} – liquid steel interfacial tension ($N.m^{-1}$), r_x – radius of "cavity" in the bath at the stagnant point (m), K – empirical constant ($-$), H – jet length (m), BLD – static bath level distance (m), V_{exit} – velocity of gas jet at the nozzle exit ($m.s^{-1}$), d_{exit} – diameter at the nozzle exit (m), ρ_{steel} – bath density ($kg.m^{-3}$), θ – angle of individual nozzle ($°$), n – number of nozzles in lance tip ($-$), ρ_{slag} – slag density ($kg.m^{-3}$), σ_{slag} – slag interfacial tension ($N.m^{-1}$), W_{gas} – mass of bottom stirring gas (kg), W_{bath} – mass of static steel bath (kg), W_{slag} – mass of static slag layer (kg), V_{gas} – volume of bottom stirring gas (m^3), $V_{static.bath}$ – volume of static steel bath (m^3), and V_{slag} – volume of static slag layer (m^3).

2.3 Cold Model Fundamentals

According to the general theory of models, the results obtained in the laboratory model of an industrial unit apply to the industrial practice when there is a complete similarity between the model (operated in the laboratory) and prototype (industrial reactor). That is to say, all similarity criteria such as geometric, kinematic, dynamic as well as thermal and chemical are satisfied. In such cases, the correlation between dimensionless numbers describing the above similarity principles in the model can be transported to the prototype, and essential parameters for optimization of the process can be determined, Figure 2.15 [19].

The relation of shape defines the geometric similarity, and one system is geometrically similar when the ratio of any length in one system is the same everywhere in the other
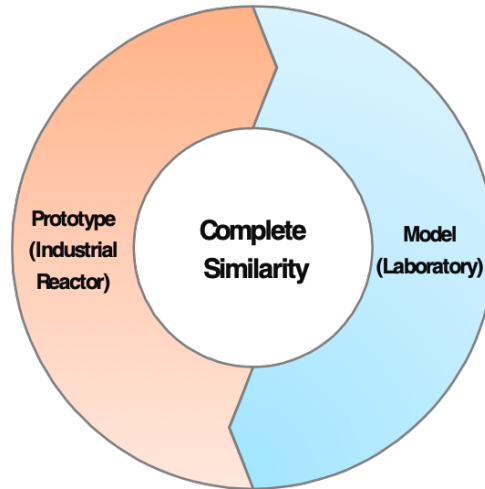
Figure 2.15: Complete similarity - general theory of models.

comparing system. Kinematic similarity represents the similarity of motion. Dynamic similarity represents the similarity of forces and is observed between the two systems when the magnitude of forces at analogous positions in both systems is in a fixed ratio [14].

2.3.1 Similarity

In the modelling of fluid flow problems, both geometric and dynamic similarity must be observed if quantitative results are aimed [14]. For the study of the fluid flow, a model can be built in the laboratory using a geometric factor λ.

$$\lambda = \left(\frac{Model}{Prototype} \right)_{Characteristic\ Length} \tag{2.9}$$

The physical modelling objective is to represent a modelled system by changing the materials to be handled, and also the scale of the operation, to achieve realistic representation, but at the same time to allow more conveniently measurements, and in a cost-effective manner. The principles of physical modelling may be derived from the differential equations that govern fluid flow and the associated heat transfer, and mass transfer phenomena [15]. The Navier-Stokes equations apply to both model and prototype, assuming a Newtonian and incompressible flow of a fluid through a conduit of arbitrary shape, [19].

$$\nabla . V = 0 \tag{2.10}$$

$$\rho . \frac{DV}{Dt} = -\nabla . P + \eta . \nabla^2 . V + \rho . g \tag{2.11}$$

Equations 2.10 and 2.11 define the equations of continuity and motion, respectively. Where, ρ – density $(kg.m^{-3})$, V – velocity $(m.s^{-1})$, t – time (s), P – pressure $(N.m^{-2})$,

η – dynamic viscosity ($kg.m^{-1}.s^{-1}$), g – gravity acceleration ($m.s^{-2}$) and L – length (m).

$$\nabla = \frac{\partial}{\partial x}.\overrightarrow{i} + \frac{\partial}{\partial y}.\overrightarrow{j} + \frac{\partial}{\partial z}.\overrightarrow{k} \tag{2.12}$$

$$\nabla^2 = \frac{\partial^2}{\partial x^2} + \frac{\partial^2}{\partial y^2} + \frac{\partial^2}{\partial z^2} \tag{2.13}$$

$$\frac{D}{Dt} = \frac{\partial}{\partial t} + \frac{\partial}{\partial x}.V_x + \frac{\partial}{\partial y}.V_y + \frac{\partial}{\partial z}.V_z \tag{2.14}$$

Where equation 2.12 is the gradient operator, equation 2.13 is the Laplace operator and equation 2.14 is the substantive operator derived over the movement or Stokes operator. The following dimensioless variables are defined in terms of characteristic values of velocity (V), length (L) and pressure (P_0) [19].

$$x^* = \frac{x}{L}; y^* = \frac{y}{L}; z^* = \frac{z}{L}; V^* = \frac{V_i}{V}; P^* = \frac{P - P_0}{\rho.V^2}; t^* = \frac{t.V}{L} \tag{2.15}$$

$$\nabla^* = L.\nabla = L.\left(\frac{\partial}{\partial x}.\overrightarrow{i} + \frac{\partial}{\partial y}.\overrightarrow{j} + \frac{\partial}{\partial z}.\overrightarrow{k}\right) = \left(\frac{\partial}{\partial x^*}.\overrightarrow{i} + \frac{\partial}{\partial y^*}.\overrightarrow{j} + \frac{\partial}{\partial z^*}.\overrightarrow{k}\right) \tag{2.16}$$

$$\nabla^{*2} = L^2.\nabla^2 = \frac{\partial^2}{\partial x^{*2}} + \frac{\partial^2}{\partial y^{*2}} + \frac{\partial^2}{\partial z^{*2}} \tag{2.17}$$

$$\frac{\partial}{\partial t^*} = \left(\frac{L}{V}\right).\frac{\partial}{\partial t} \tag{2.18}$$

The equations of continuity and Navier Stokes can be written as equations 2.19 and 2.20, respectively [19].

$$\nabla^* V^* = 0 \tag{2.19}$$

$$\frac{DV^*}{Dt^*} = -\nabla^*.P^* + \frac{1}{\left(\frac{L.V.\rho}{\eta}\right)} \times \nabla^{*2}.V^* + \frac{1}{\left(\frac{V^2}{L.g}\right)} \tag{2.20}$$

These equations are valid for both the model and the prototype and represent a family of equations describing the velocity fields. A specific equation of this group may be needed for solving a particular problem for which initial conditions and boundary conditions are known. The solutions for the model and the industrial unit (prototype) are the same if the coefficients of the terms of the differential equations are the same [19].

$$\left(Re = \frac{L.V.\rho}{\eta}\right)_{Prototype} = \left(Re = \frac{L.V.\rho}{\eta}\right)_{Model} \tag{2.21}$$

$$\left(Fr = \frac{V^2}{L.g}\right)_{Prototype} = \left(Fr = \frac{V^2}{L.g}\right)_{Model} \tag{2.22}$$

A physical model and the industrial unity (prototype), are rigorously similar if they meet the criteria for geometric and dynamic similarity. It means that the model and the prototype are of identical shape, but not necessarily on the same scale, and the forces acting on the system are of the same ratio. In practice, the same equations will apply, and the only difference will be introduced through the scaling factors, which can be attained if the key dimensionless numbers are the same. In other words, they will behave identically as long as the Reynolds and the Froude numbers are the same [15].

These arguments relate to a single-phase flow system in the absence of free surfaces. Nevertheless, the metallurgical process can be somewhat more complicated. To represent these phenomena, additional and more complex differential equations and boundary conditions need to be used, which introduce further dimensionless groups.

2.3.2 Dimensionless Numbers

A large number of dimensionless numbers applicable in various fields involving heat mass and momentum transfer are available in the literature. A partial list of dimensionless numbers, relevant to the metallurgical processes, are briefly explained in the following paragraphs and summarized in the Table 2.2 [63].

Table 2.2: Dimensioless groups of relevance in Process Metallurgy [63].

Group	Definition	Application
Froude	$Fr = \frac{\mu^2}{g.L}$	Wave and surface behaviour pouring streams.
Modified Froude	$Fr' = \frac{\rho_g.V^2}{(\rho_L - \rho_g).g.L}$	Fluid behaviour of gas-liquid systems.
Mach	$Ma = \frac{\nu}{\nu_s}$	High speed flow.
Reynolds	$Re = \frac{L.V.\rho}{\eta}$	Fluid Flow.
Weber	$We = \frac{\rho.L.V^2}{\sigma}$	Bubble Formation, atomization of liquid jets.

- **Froude Number**, dimensioless number used for describing wave and surface behaviour in pouring streams (inertial force/buoyancy force) [63].

$$Fr = \frac{\mu^2}{g.L} \tag{2.23}$$

- **Mach Number**, specifies the effect of fluid compressibility on the flow and expresses the transition from bubbling to jetting (inertial force/elastic force) [13].

$$Ma = \frac{\nu}{\nu_s} \tag{2.24}$$

$$\nu = \frac{4.Q_g}{\pi.d_{nozzle}^2} \tag{2.25}$$

Meidani et al. [68], introduce the following modified Froude, Reynolds and Weber numbers through the BOF water modelling considering the supersonic nozzle jet.

- **Modified Froude Number** [68], this parameter represents the ratio of the inertial force of injected gas to the buoyancy force acting on bubbles generated at the nozzle exit. Widely used to characterize the movement of bubbles generated with a single hole nozzle (inertial force/buoyancy force).

$$Fr_{Meidani}^* = \frac{\rho_{gas}.V_{exit}^2.d_{exit}^2}{\rho_{steel}.g.H^3} \tag{2.26}$$

- **Reynold Number** [68], dimensionless number useful for describing the transition from laminar to turbulent flow as well as the reverse transition (inertial force/viscous force) [13].

$$Re_{Meidani}^* = \left(\frac{\rho_{steel}.\rho_{gas}.V_{exit}^2.d_{exit}^2}{\mu_{steel}^2} \right)^{\frac{1}{2}} \tag{2.27}$$

- **Weber Number** [68], essential parameter for metallurgical engineering systems because the surface tension of melted metal is usually considerably higher than fluids often used in mechanical and chemical engineering systems such as water (inertial force/force due to surface tension) [13].

$$We_{Meidani}^* = \frac{\rho_{gas}.V_{exit}^2.d_{exit}^2}{\sigma_{steel}.H} \tag{2.28}$$

Where, μ, ν – dynamic viscosity ($kg.m^{-1}.s^{-1}$), g – gravity acceleration ($m.s^{-2}$), L – length (m), ν – cross-sectional mean velocity of gas in the nozzle ($m.s^{-1}$), ν_s – speed of sound ($m.s^{-1}$), Q_g – gas flow rate ($m^3.s^{-1}$), d_{nozzle} – inner diameter of the nozzle (m), ρ_{gas} – density of the gas at the nozzle exit ($kg.m^{-3}$), V_{exit} – velocity of gas jet at the nozzle exit ($m.s^{-1}$), d_{exit}^2 – diameter at the nozzle exit (m), ρ_{steel} – bath density ($kg.m^{-3}$), H – jet length (m) and σ – interfacial tension ($N.m^{-1}$).

2.4 BOF Cold Modeling Literature Review

Modern thermodynamic and kinetic process models are classified as single and multi-zone models. The single-zone models are the models, in which the mass flow between the reaction zones (hot spot, metal-slag-gas, emulsion, among others) is not considered. The multi-zone modelling theory divides the converter process into a restricted number of reaction zones [60]. Nevertheless, most of the modern models do not consider the

physical effects of lance blowing on the process [32]. In order to have a better process understanding, the kinetic calculations should be based on technological parameters such as oxygen lance and bottom stirring pattern, as well as the geometry of the lance and converter, including the bottom stirring elements [60].

Physical models are frequently applied for BOF process development in the initial stage, as well as today. The mechanism of the blow in hot models has already been studied in a limited number of publications [69, 70, 71, 72, 73, 59]. Nevertheless, valuable insights could be assumed about penetration depth, metal splash, and droplet generation, and size. Due to the difficulties for direct observation, physical modelling offers essential tools to deal with process development and optimizing the BOF process [20], Figure 2.16 shows a general subdivision of steelmaking modelling.
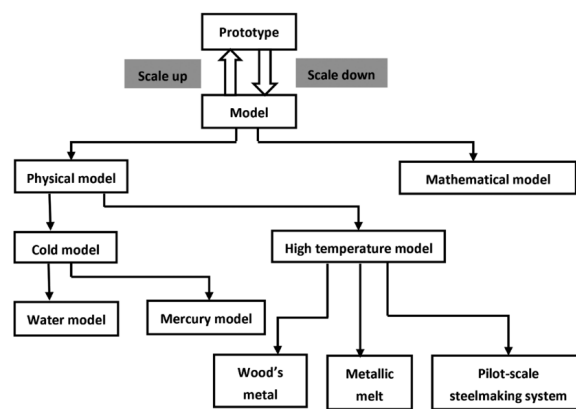
Figure 2.16: Modeling approaches in steelmaking [20].

Comprehensive former publications have applied cold model experiments, based on water and air, to check the mixing performance, flow patterns, the effect of the jet on the bath surface, and even some heat transfer. Newby [74] developed one of the first physical models about the fluid flow in a side-blown converter and observed the existence of a gas back attack effect. At that time, the vast field to study the effects of the jet on a liquid surface, and the benefits of physical water simulation became evident.

2.4.1 Top Blowing, Jet Penetration and Droplet Generation

Cold modelling simulation to investigate the jet penetration and the splashing of liquid materials due to the oxygen jet in the BOF converter has been studied by many researchers since the early times.

Collins and Lubanska [75] investigated through photographies the water surface turbulence caused by a jet of air. The penetration depth was measured, and an equation established for a single hole lance, blowing with differents axial angles. Similar research was done by Glass and Hays [76], and they published extensive research on the physical mechanisms of jet penetration and bath movement, as well as the nozzle parameters that

influence the BOF process. Cheslak et al. [77] developed trials on water and wet cement to observe cavities formed on liquid surfaces by impinging gaseous jets.

In the extensive research report (1953-1963) published by Glass and Hays [76], a set of trials employing various liquids and gases was performed, including chemical reaction trials between the liquid and the jetted gas (e.g., air, water, glycerine, mercury, hydrogen chloride into soda solution and others). Even a physical model of water to simulate steel and a layer of balsa wood chips to simulate the slag layer were shown. The same circulation pattern was observed in the liquid bath by the gas jet in all simulations. The primary and intuitive knowledge nowadays could be established in this first study [78, 79, 80, 81, 76].

> - *Increasing the gas flow rate generally produces greater jet penetration in the liquid bath.*
>
> - *Reducing the lance tip height increases the depth of penetration and rate of circulation.*
>
> - *Increasing the fluid viscosity, the penetration depth is slightly reduced, but the circulation rate is considerably decreased.*

Glass and Hays [76]

The same research group also made trials of three-hole lance nozzles in a water modelling, the first with these characteristics available in the literature [82]. They developed four experimental converters for hot trials, Figure 2.17, and they confirmed the theory about the jet penetration and bath circulation stated in the previous water modelling publications, large scale trials in 55 t converter were also done. This research was relevant at that time because a different theory concerning only "surface blowing" was established, in which they believed that the oxygen jet did not penetrate deeply into the molten metal bath. The impingement area was limited to the bath surface [69]. Following the research, Rote [83] established the effects of the blowing conditions on dephosphorization, and also introduced the concept of soft and hard blowing in the BOF. Sharma et al. [70] also developed cold and hot simulations to observe bath circulation, jet penetration, and high-temperature reaction zone in BOF steelmaking, both works were in a good agreement.

Inada et al. [84], proposed a study on the rate of CO_2 absorption in $NaOH$ solution to investigate the fundamentals of gas-jet liquid reaction, different lancing and blowing operation conditions were simulated. The rate of CO_2 absorption was determined by continuously measuring pH values of the $NaOH$ solution. As the solution absorbs CO_2 from the jet, the pH value of the solution decreases. At least during the steady-state of decarburization, the oxygen supply rate controls the process, and the decarburization can be noted as oxygen supply absorption, which may be simulated by CO_2 absorption from
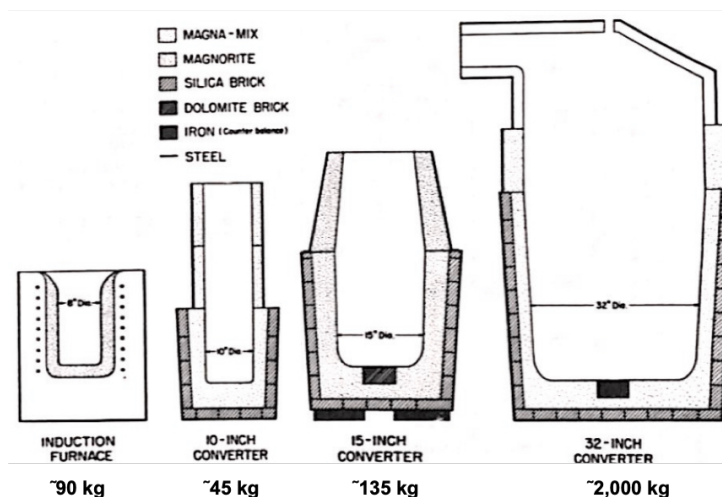
Figure 2.17: Schematic drawing of four test vessels used in laboratory hot metal tests [69].

the gas jet into $NaOH$ solution. The proposed mass transfer model was validated in a commercial VOD operation.

Koria and Lange [85] carried out essential research for the BOF process understanding, they performed a series of investigations for high-temperature and cold models, considering full criteria of similarity with industrial converters. They focused on three main domains, such as the behaviour of supersonic gas jet (Figure 2.18), impinging gas jets, and metal droplets mechanism. The authors also investigated the top blowing and bottom stirring parameter effects on the total mixing time.

General findings regarding the first topic were related to the description of the axial velocity decay characteristics of an under-expanded supersonic gas jet by the Gauss-error function. Authors proposed correlations, validated with industrial plants, to determine the nozzle design and the distance between bath level and lance tip and their variation during the blow. The depression diameter and depth produced by an impinging jet were measured for single or multi-nozzle jet and correlated with flow rate momentum dimensionless [86, 87, 88].

Experimental trials, with high-velocity oxygen blowing on molten pig iron, were performed to determine the penetrability of impinging gas jets, the mechanism of metal droplet production, evolution, and size distribution. They describe two stages, the build-up phase with a stable cavity and the stationary phase with massive expulsion of metal droplets depending on the impact pressure. These droplets are strongly oxidized, which help to build a slag rich in FeO in the early stages of blowing; they also observed slag/metal emulsion formation immediately after blow started. Blowing parameters such as oxygen supply pressure, lance distance, and the number of nozzles affect the drop size distribution. Particle diameter was correlated with Weber's number. The degree of droplet break-up and decarburization rate increased with an increase of Weber's number (e.g., jet velocity) [85, 89, 90, 91, 92, 93, 94]. The authors also developed top blowing and

bottom stirring simulations, and discussions are available in the next sub-sections.
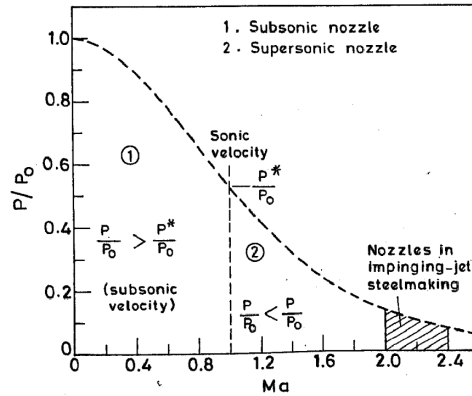
Figure 2.18: Classification of gas injection nozzles [88].

Many researchers concentrated on investigating the effect of nozzle design, lance height, and flow rate to investigate the penetration extent and the splashing height in water modelling during lance blowing. They also propose empirical equations for penetration depth and droplet generation considering different blowing conditions [95, 96, 97, 98, 99, 100, 101, 102, 103, 104, 105]. On the other hand, cold modelling simulations using liquids such as mercury were also adopted [106, 107, 108, 109, 110]. Ek and Sichen [111], carried out a cold modelling investigation employing a liquid alloy $Ga - In - Sn$, similar to the melted steel physical properties, and HCl solution to simulate the slag. They found a significant effect of the slag phase on the penetration depth.

Meidani et al. [65] studied the performance of shrouded supersonic jets in BOF water models; this study introduced new dimensional analysis and relevant dimensionless numbers. The dimensional analysis shows that the penetration depth produced by an impinging gas jet in a liquid melt is dependent on the Bath Level Distance (BLD). The dimensionless numbers such as Reynolds, Froude, and Weber reflected the proportions of viscous, gravity, and surface tension forces to the jet's momentum or inertial forces. The observed and predicted penetration depths were in a good agreement between the experiments and the mathematical model [68].

More recent researches have adopted cold model experiments and CFD simulations to study the cavity formation, shape and the spitting phenomena by the impinging jets [112, 113, 114, 115, 116, 117] as well as the effect of cavity shape on the stirring characteristics and the mixing time in the BOF [118, 119, 120]. Sabah and Brooks [121] developed a cold model to investigate various cavity modes based on the sound waveform analysis [122].

Maia [123] tried different nozzles design, even a twisted nozzle, to show the jet penetration and the mixing time [67, 124]. They developed different lance designs for trials and established the jet penetration equations for different conditions, as well as the investigation of splashing behaviour [125], and additionally proposed an energy balance equation considering the slag phase to determine the impacts of the jet penetration considering the

resistance to momentum transference between exit nozzle and metallic bath [64]. Zhong et al. [126], also performed trials with twisted nozzle, but in this case, they studied the effect on the slag splashing practice. Another cold model to study the slag splashing practice was proposed by Luomala et al. [127].

2.4.2 Top Blowing and Bottom Stirring

The first water modelling experiments, including both top blowing and bottom stirring, started in the early 80s. Mixing time and the mass transfer rate were investigated through different combinations of bottom tuyere designs and flow patterns and in some cases, different top blowing parameters and in many times they were focused on investigating the differences between BOF and Q-BOP process.

Nakanishi et al. [128], investigated different tuyere configurations, and they developed empirical relations for the mixing time and mixing energy based on the tuyeres number and the gas flow rate, as well as the mass transfer rate between the metal and slag. They found a closer thermodynamic equilibrium between metal and slag for the Q-BOP compared to the BOF process.

Kai et al. [129] assessed the impacts of the bottom stirring flow rate, melt depth, the number of tuyeres, and configuration, Figure 2.19, as well as the top blowing influence on splash behaviour and mixing characteristics. In shallow baths, they found high dependence of bottom stirring on the result of mixing time, which is not strongly influenced by other factors. The energy efficiency related to the top-blown gas is considered to be one-tenth for the mixing of the bath when compared to bottom stirring gas efficiency.
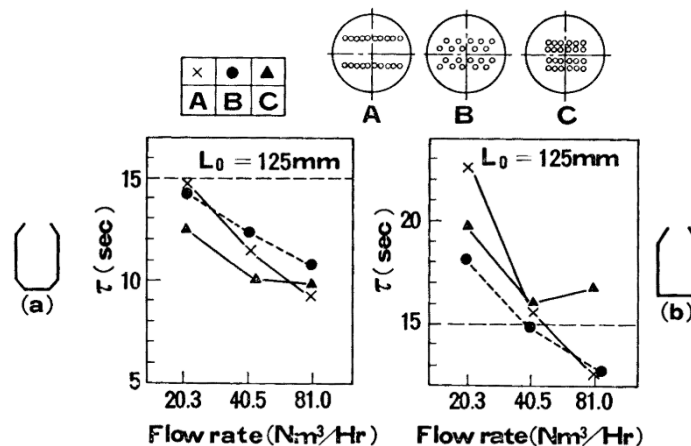
Figure 2.19: Mixing time results according to tuyere configuration, bottom design and gas flow rate, where L_0 = quiescent bath level [129].

Kyoji et al. [130] built a physical model similar to the industrial process (LD-KG and K-BOP) at Kawasaki plant. Tracer injection (CO_2) was used to evaluate the mixing time at different tuyere configurations, flow rate, and mode of blowing. The rate of mass transfer between slag (liquid paraffin containing $B - naphtol$ as a solute) and metal

(water) was determined by using different ratios of slag-metal volume. The modified Froude number was adjusted in the cold modelling to simulate the plant scale. Hot model experiments in a $5\,t$ experimental converter equipped with a top lance and bottom stirring elements were performed, Copper (Cu) was used as a tracer to calculate the mixing time in sophisticated hot experiments. After this hot model experiment, they performed industrial trials for various processes. The results comprising the cold model, hot model tests, and industrial trials were in a good agreement. They developed semi-empirical equations for mixing time and the respective mixing energy, considering the various process variations.

Ghosh and Singh [47], also developed a water model experiment to compare the mixing time between the regular BOF process (top blowing), BOF with five different bottom stirring configurations and the Q-BOP process. Mixing time was determined by the tracer technique; they found that the bottom gas flow rate per tuyeres and tuyere arrangement has a low effect on mixing time. On the other hand, the number of tuyeres had a pronounced effect on mixing time.
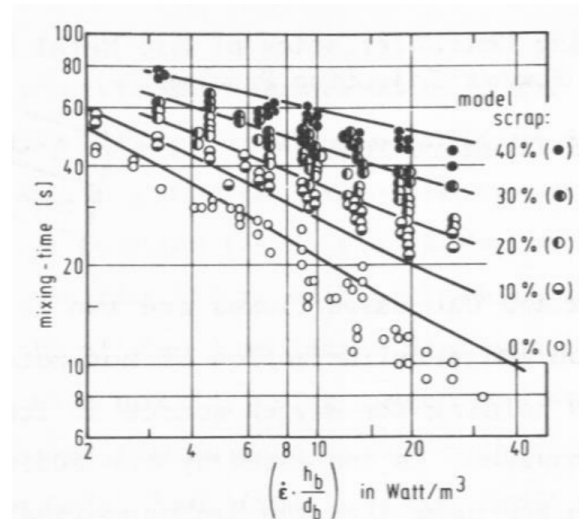
Figure 2.20: Effect of top blowing and bottom stirring parameters on the mixing time, according to different scrap ratios on the results of especific stirring energy (W/m^3_{bath}) [131].

As already mentioned, Koria and Lange [131] developed a wide range of cold and hot modelling; the following paragraph discusses the top blowing and bottom stirring investigations, individually or combined. They developed a cold model to investigate the mixing time and the correlation of blowing parameters and melting scrap. The mixing-time obtained by a chemical decolouration method, and model melting scrap consists of ice pieces containing small metal pieces in such a way that they sink in the model bath. Mixing time results considering scrap are correlated with the applied power density. The main factors affecting the mixing time for top blowing experiments are related to bath height, bath diameter, nozzle diameter, supply pressure, and lance distance. An increase in the supply pressure or decrease in lance distance at constant bath height and diameter

decreases the mixing time [132]. General findings related to bath height, bath diameter, gas flow rate, and amount of scrap for a given tuyere configuration considering the bottom stirring investigations were obtained. They additionally observed that a deep bath without or with scrap mixes easier than a shallow bath at all flow rates of the injected gas, Figure 2.20 [131]. Based on the results of cold model simulations, a hot model investigation was performed in an experimental converter (80 kg) to validate the previous works [72].

Koria and George [133] following their investigations, carried out cold models to determine the effects of bottom gas injection parameters and design, and the mass transfer rate between two immiscible liquids (water-oil) was employed to indicate the bath mixing conditions. Parameters such as gas-injection rate, tuyeres number, and their configuration in combination with top blowing were tested. They determined the mixing conditions of the bath by the cumulative influence of gas injection rate and the Pitch Circle Diameter - PCD (d/D), gas injection rate, and PCD are the most important parameters governing the mixing of the bath, Figure 2.21 [133]. The bath mixing power enhanced according to the increase of the top and bottom gas flow rates and decreased according to BLD increments [134, 135].
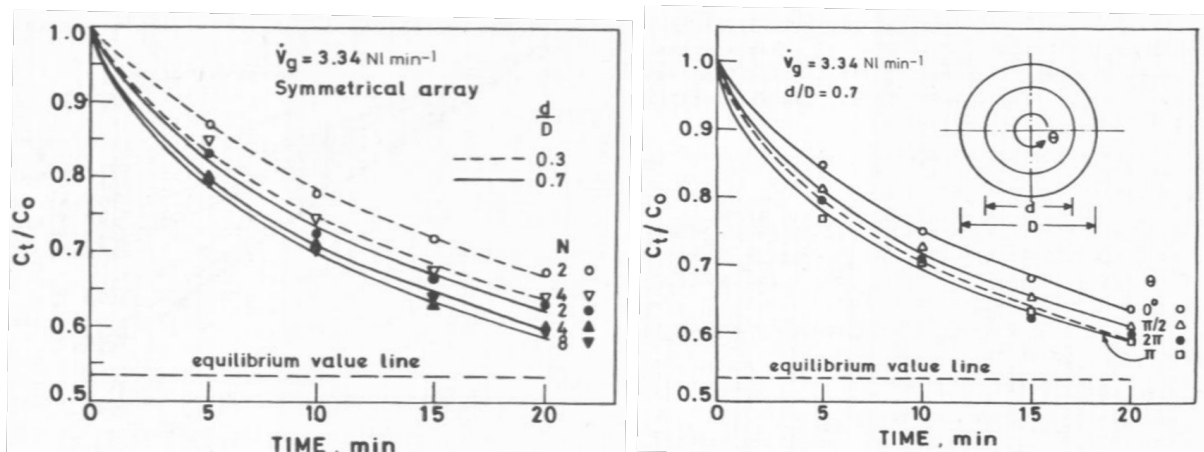
Figure 2.21: Mixing conditions for different tuyeres number (left) and arrangements (right), where C_t/C_0 is the fractional concentration of benzoic acid in water [133].

A series of cold model experiments were performed to simulate the top blowing and bottom stirring in dual or three-phase conditions. In the three-phase simulation, the use of oil to simulate the slag conditions is added to the dual-phase system (air-water). The rate constant for the process of mass transfer between two simulated immiscible liquids (water-oil) in the BOF process is employed to evaluate the bath-mixing intensity. Frohberg et al. [136], Schlarb and Frohberg [137], Gerlach and Frohberg [138], developed their studies based on the caprylic acid mass transfer rate among the phases of water and oil to study the different top blowing and bottom stirring strategies. Similarly, Koria and Pal [135], Martín et al. [139], and Wu et al. [140] developed their studies measuring the transfer rate of benzoic acid from water to oil. General findings were related to improved

mixing time for combined blowing, a small bottom stirring flow rate - comparing to the top blowing rates - has a significant influence on mixing time.

Roth et al. [141, 8], studied the effect of slag in the top blowing and bottom stirring parameters and found that according to the level of slag thickness in combination with the power of the top blowing momentum, the fluid flow is dominated by top blowing or bottom stirring. At the transition from the two-phase to the three-phase system, the influence of top blowing is lowered, because the slag simulation phase acts as a barrier.

Luomala et al. [100], developed an experimental apparatus to determine the splashing distribution on the walls of the BOF model, Figure 2.22. They investigated the effect of various top blowing and bottom stirring parameters on the splashing rate, which allowed discussions about refractory lining wear, metal losses, and skulling of the cone [142]. Next, bottom stirring, and the interaction with the top blowing lance were studied. The main focus was on splashing, homogenization, and oscillation of the bath. According to the results, the position of bottom stirring elements has a significant preponderance on the splashing and spitting direction and quantity [143].
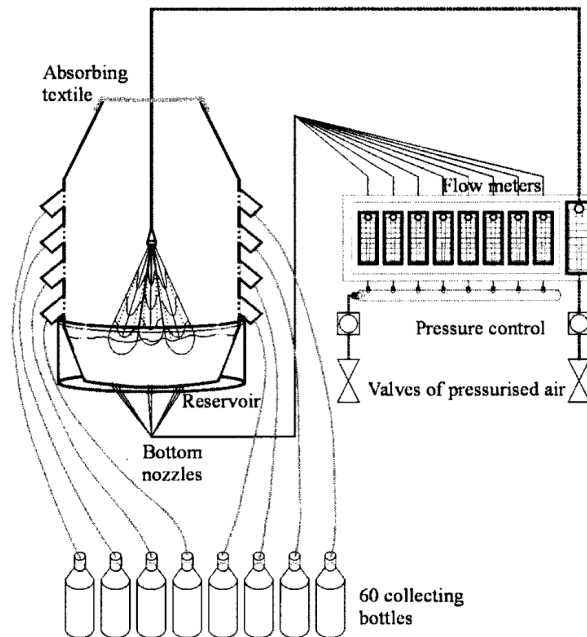
Figure 2.22: Experimental setup to measure splashing distribution in the BOF [142].

Olivares et al. [118] developed a BOF two-phase model to simulate top blowing, bottom stirring, and the combined top blowing-bottom stirring process. In top blowing, mixing time decreases as the gas flow rate increases, and the lance distance from the bath surface decreases, Figure 2.23. Lower and higher bath heights (H) were also tested, and different trends were observed. When bottom stirring was activated, the mixing times decreased according to the number of tuyeres and increased according to the risen of the gas flow rate and the bath height. In the combined top blowing-bottom stirring process, mixing time reduced considerably due to the recirculating flow developed by the effect of

the top jet and the submerged stirring [119].
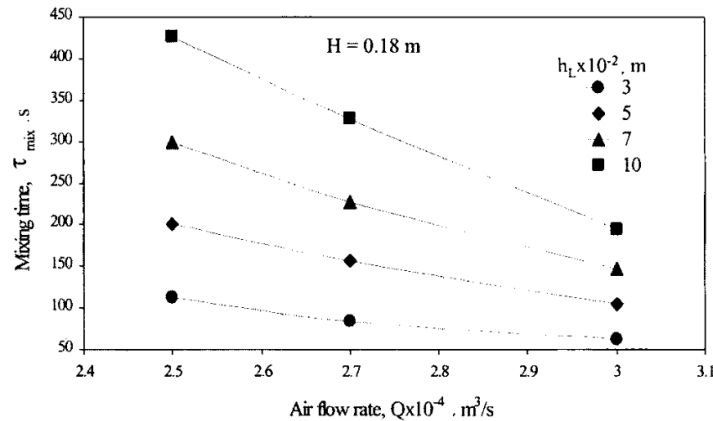
Figure 2.23: Effects of the lance distance from bath level (h_L), and the air flow rate on mixing time for top blowing experiments [118].

Martín et al. [144] studied a three-phase cold model, first investigated the formation of gas bubbles in the bulk of the liquid phase, emulsion and droplets, and the streamlines. Later, they determined the mixing time [27], and mass transfer rate [139] for different blowing conditions.

Ajmani and Chatterjee [145] developed a cold model similar to 130 t BOF in operation in a Tata Steel Jamshedpur, they simulated different top blowing and bottom stirring tuyere designs to determine the mixing time and mass transfer rate. Following, the same research group performed another cold model work comparing an existing bottom with six stirring elements versus a proposed bottom design with eight stirring elements. They implemented in the plant operation, the bottom with better results, and compared the metallurgical results [146]. A comparison of the interaction top lance with different radius distributions of bottom blowing plume was performed, and the cold model was confronted with mathematical model simulations [147].

Wei et al. [148] developed AOD cold models to investigate streamlines, mixing time [149], and mass transfer rate [28] for a series of different conditions of side and top combined blowing.

Bruckhaus and Lachmund [150] developed BOF cold model similar to Dillinger Huette (Germany) to investigate the arrangement of bottom-stirring after the exchange of the vessel in the plant. They observed the worst metallurgical results for the new vessel. To improve the metallurgical results with the new vessel design, they performed cold model investigations of bottom stirring radius arrangement, bottom stirring gas flow rate, and lance tip design, as well as the interactions between oxygen jet and heterogeneous plume [151]. Similar investigations were done by Oymo and Guthrie [152].

Zhou et al. [153] developed a physical model to study the mixing time of a 30 t converter, they experimented a new bottom tuyere design with an asymmetrical arrangement, and the CFD models were employed to study the characteristics of the fluid flow fields.

They also tried the side and bottom tuyere in combination with a top lance, and they found a reduced mixing time for the side-blown converter compared to the regular top blowing and bottom stirring converter [154, 155].

Carvalho et al. [156], developed a physical model similar to Ternium Brazil's 330 t BOF to investigate different top blowing and bottom stirring configurations for a dual-phase system.

Significant correlations of mixing time and decarburization areas were established to determine the best blow set-up for the main blow period. Furthermore, to investigate the decarburization at the end-of-blow, CO_2 desorption technique was adopted. Afterwards, a bottom stirring with a differential flow strategy was performed in the multiphase cold model and applied in industrial tests [157, 125, 64, 158, 30].

2.4.3 Bottom Stirring

Figueira and Szekely [159] studied in an AOD cold model, the turbulent fluid flow phenomena and used a laser velocimetry to determine the velocities, turbulent kinetic energy, and the Reynolds stresses in the system. To determine the local heat transfer rates, they measured the immersed ice rods melting rate, and the measurements showed nearly uniform velocity fields and stable distribution of the turbulent kinetic energy, resulting in the absence of dead zones.

Stišovic and Koch [160] performed cold model investigations to investigate a range of bottom stirring configurations such as centric nozzle, nozzle rings, and screen bottoms. They found good mixing time for increased blowing rate, increased eccentricity, larger nozzle diameter, and larger ratios of bath level versus bottom diameter.

Singh et al. [161], developed a BOF cold modelling to investigate different bottom stirring schemes, in a way that a linear flow gradient is imposed across the bath. They found improved mixing time and mass transfer rate for the differential flow rate, and industrial plant experiments were performed to evaluate the impact on dephosphorization. Later, they performed a CFD simulation to investigate the mixing in the dual-phase system (air-water), results were in good agreement with cold simulation [162].

2.4.4 Measurements Methods

Developments regarding experiment measurements are necessary. Outputs such as mixing time, mass transfer, and some other indirect measurements need to be known precisely. The review of cold modelling measurements developed to understand the available knowledge in literature is organized according to Figure 2.24.
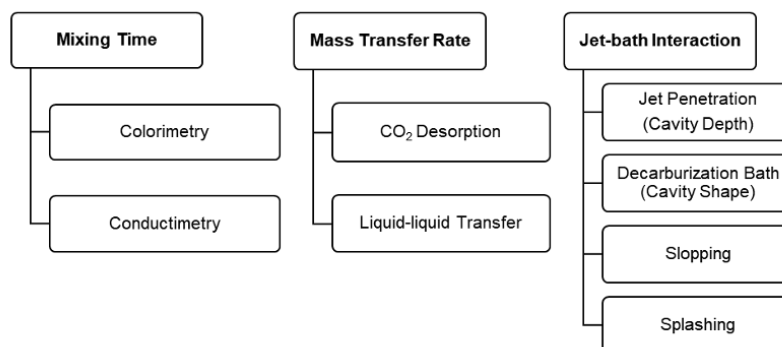
Figure 2.24: Measurement methods for BOF cold modeling.

2.4.4.1 Mixing Time and Stirring Behavior

The reactions placed in the BOF are heterogeneous and depend on mass transfer to occur. Mixing time is an essential parameter to refining operations that can help to attain a better efficiency of the process. According to Mazumdar and Evans [163], mixing time is used as a measure to assess the chemical efficiency, and it is defined as the time required for the bath to achieve a specified value of homogeneity, usually 95%. Singh et al. [147] confirms that bottom stirring performs an essential task over the BOF mixing process. According to the authors, bottom stirring is influenced by several parameters such as the amount of gas flow, the number of tuyeres installed, tuyere configuration and design, shape and size of the bath, and others. Numerous methodologies can be used to determine the mixing time in physical models [164], such as colourimetry, electrical resistance tomography, planar laser-induced fluorescence, thermography, luxmeter, conductivity meter, *pH* measurement, colourimetric and volumetric chemical analysis.

Colourimetry is one of the most common techniques used to measure this parameter [164, 131, 165, 166, 167, 168, 169, 170]. This methodology consists of an injection of a liquid solution and a fluid behaviour observation, and the tracer removes or changes the colour of the bath. In addition to the mixing time determination, this methodology makes it possible to qualitative visualization of the flow patterns, and uncover the presence of secondary flows produced under steady stirring such as well-mixed regions, isolated spots, and other segregated areas like stagnant of dead flow zones. In the literature, different kinds of experiments for colourimetry methodology are available, varying on the kind of tracer used, the stirring method, and the geometry of the reactor. Several authors used cylindrical vessels to carry out the experiments [165, 166, 169, 170], some others used scale models of steel reactors [167, 168].

The colour change promoted by *pH* control is also a well-studied tracer alternative [165, 166, 170], and it consists of adding a solution that changes the colour of the bath according to the *pH* conditions of the fluid. Another alternative is to add a solution that has a distinct colouration when compared with water, such as iodine starch [131], potassium permanganate, blue methylene [169], food colouring [168], and others. Recent

research shows a new way of determining the mixing time by colourimetry using low-density particles [167, 168]. Wuppermann et al. [168] performed experiments with two approaches, one to determine the mixing time in a scale vessel of an AOD converter, Figure 2.25, by adding food colouring and a photometer for data acquisition. The authors also determined the two-dimensions velocity field in the symmetry plane of the water-model through the addition of doped polyamide particles, and they monitored it through the Particle Image Velocimetry (PIV) technology.
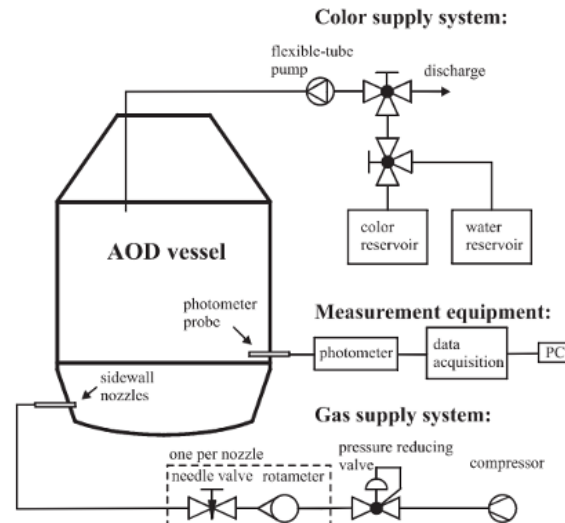
Figure 2.25: Gas supply system and measurement setup for the AOD water model system [168].

Holmes et al. [171] firstly reported the use of physical conductivity measurements for mixing effectiveness in a stirred vessel. They employed the conductivity meter to determine the time required for a tracer to complete the full circulation throughout the tank. The ionic tracer was inserted into the centre of the turbine and was distributed into all directions and detected by the conductivity probe.

The mixing time investigations through the conductivity meter technique have been applied in many different reactors cold modellings such as RH, EAF, BOF, gas-stirred ladles, and tundish. Paul and Ghosh [97] and Ghosh and Singh [47] published investigations regarding the mixing time of top blowing and bottom blowing, considering the Q-BOP and LD cold models. Chen et al. [172] summarized the study of many investigators using the conductivity meter to determine the mixing time for many different vessels and tracers employed.

The mixing time study is a valuable tool to support the BOF improvement, even for different types of stirring, such as top blowing, bottom stirring, or the combined top blowing and bottom stirring [145, 146, 161]. Some authors also employed the conductivity meter method to study mixing time on a system in which there is a phase simulating the slag layer [27, 141, 8].

Table 2.3: Details of the various physical modelings using colorimetry and conductivity investigations.

Method	Authors	Year	Reactor	System			Stirring Type				Dimensionless Number			Tracer	Ref.
				AW	AWO	O	T	B	TB	IS	Fr	Re	NP		
Colorimetry	Koria et al.	1984	Cylindrical vessel	•				•					•	Iodine starch	[131]
	Melton et al.	2002	Cylindrical vessel	•				•					•	Methyl red, Thymol blue	[165]
	Ascanio et al.	2004	Cylindrical vessel	•						•		•		Acid-base indicator	[166]
	Kuo et al.	2011	Gas-stirred ladle	•			•						•	Polyethylene particles	[167]
	Wuppermann et al.	2012	AOD	•					•		•			Food Coloring	[168]
	Kumar et al.	2014	Cylindrical vessel	•			•				•			Methylene blue	[169]
	Rosseburg et al.	2018	Cylindrical vessel	•					•		•	•		Phenolphthalein	[170]
Conductivity	Holmes et al.	1964	Turbine-stirred vessel	•								•		H_2SO_4	[171]
	Oymo et al.	1984	BOF	•				•	•		•			KCl, HCl	[152]
	Paul et al.	1986	BOF, Q-BOP	•			•	•			•			KCl	[97]
	Ghosh et al.	1988	BOF, Q-BOP	•				•			•			KCl	[47]
	Roth et al.	1995, 1999	BOF	•	•	•	•	•					•	$NaCl$	[141, 8]
	Olivares et al	2002	BOF	•			•	•			•			KCl	[118]
	Stisovic et al.	2002	BOF	•				•					•	$NaCl$	[160]
	Ajmanl et al.	2005	BOF, EOF	•	•		•	•	•		•			KCl	[145]
	Martin et al.	2005	BOF	•	•		•	•	•		•			KCl	[27]
	Choudhary et al.	2006	BOF	•					•		•			KCl	[146]
	Singh et al.	2007	BOF	•			•	•			•			KCl	[147]
	Chen et al.	2013	Gas-stirred ladle	•									•	KCl, $NaCl$	[172]
	Quiyoom et al.	2018	BOF	•				•			•			KCl	[162]

System	AW → Air-Water, AWO → Air-Water-Oil, O → Others.
Stirring Type	T → Top Blowing, B → Bottom Stirring, TB → Top Blowing + Bottom Stirring, IS → Impeller System.
Dimensioless	Fr → Froude Number, Re → Reynolds, NA → Not Available.

Olivares et al. [118] studied mixing time in 1/8 length scale of a BOF using a conductivity probe 180° from the tracer's injection point, and also proposed some equations correlating mixing time with blowing parameters. Oymo and Guthrie [152] performed conductivity measurements and proposed the mixing index, which allows comparing many mixing tests, other authors [165, 160], employed the normalized concentration to compare the mixing time of different tests and does not depend on the conductivity of the water used in the test.

Mathematical simulations of multiphase flows studying mixing time exhibited similar results when compared to physical simulations performed using conductivity meter to determine the mixing time [167, 162]. Table 2.3 summarizes all study references covered and presents the main characteristics of the tests performed to determine the mixing time using cold simulation.

It is important to note that cold simulation experiments mostly use reagents that require proper disposal. Therefore, aiming at sustainable development, whenever possible, the reuse of the components employed should be considered, if it is not possible, a proper dispose of the components is necessary.

2.4.4.2 Mass Transfer Rate

Mass transfer is another critical parameter in steel refining. The inert gas injection promotes bubble formation in the metal bath, which increases the gas-liquid contact and, as a consequence, supports the metallurgical reactions, such as decarburization, dephosphorization, and manganese oxidation.

The optimization of the combined top blow and bottom stirring is a mechanism for increasing the refining reactions based on mass transfer efficiency, and it is necessary to increase the bath agitation to promote the contact between particles.

A method named carbon dioxide (CO_2) desorption was developed mainly to analyze the behaviour of the decarburization rate by immersion lance for the bottom blown converter process. Operational conditions, converter design, nozzle diameter, and the gas flow rate design can present a significant impact on the efficiency of the gas-liquid reaction. An effective means to investigate the bubble-liquid reaction and the fundamentals of gas jet-liquid reaction is the use of $NaOH$ solution and the blown injection of CO_2 gas to evaluate the gas-liquid reaction efficiency by adopting the measurement of pH in solution [173, 84, 174]. The pH value of the solution decrease according to the CO_2 solution incorporation, introduced by the jet, and an electrode is responsible for measuring the CO_2 concentration. An alternative to $NaOH$ is the use of KOH in the solution [175] and Figure 2.26 introduces a typical relation between pH and blowing time for different CO_2 blow rate.

All studies confirmed the dependence of the gas jet on the efficiency of the absorption reaction. The authors considered the results sufficiently valuable to consolidate them as a
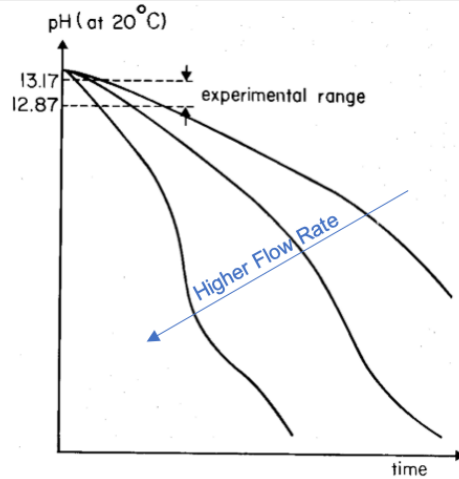
Figure 2.26: Typical pH-time curve during CO_2 absorption to KOH solution [175].

method that investigates the fundamentals of gas-liquid reactions because of its ability to measure gas absorption continuously. Nevertheless, the studies should be more conclusive about the impact of the tuyere flow and arrangement and the slag/metal interaction on the efficiency of the method.

Next, a technique was developed to investigate the mass transfer through a tracer diluted in the aqueous phase and extracted to the organic phase. The concentration difference between the two phases as a function of the processing time describes the mass transfer coefficient, and this is possible because of the dynamic similarity that allows the aqueous solution and oil to represent the steel and slag, respectively.

A method presented by Schlarb and Frohberg [137], uses caprylic acid as a carrier reagent which is added to the water prior to the addition of oil in a top and bottom stirring converter cold model. The mass transfer coefficient (β) was settled by the ratio between the transport coefficient (L) and the area of exchange (A). An equation was developed to determine the transport coefficient at known equilibrium concentration C by measuring the concentration C_W depending on the time in the condition $C_W \left(t = 0\right) = C_W^A$:

$$C_W = C_W^* + \left(C_W^A - C_W^*\right).exp\left(-\frac{L.t}{V_w}\right) \tag{2.29}$$

$$L = \frac{V_w}{t}.ln\left(\frac{C_W^A - C_W^*}{C_W - C_W^*}\right) \tag{2.30}$$

Where, C_W – concentration of caprylic acid in water ($mol.m^{-3}$), C_W^* – equilibrium concentration of acid ($mol.m^{-3}$), L – transport coefficient ($m^3.s^{-1}$), t – time (s), and V_w – water volume (m^3).

The authors assumed in the results that the distribution coefficient of caprylic acid was of nearly the same order as the metal-slag. A limitation pointed out in this method was that top blown only acts as an inert medium in the model, making it impossible to simulate the reaction between the top blown oxygen with carbon which is an additional

power to the bath circulation and consequently, mass transfer.

The tracer partition ratio in the cold modelling has the same magnitude as the one related to the phosphorus or sulfur between the steel and the slag in the steelmaking converters. It is proposed to describe the liquid-liquid mass transfer reactions, a practical experiment for a water-oil system with an easy analytical determination, which can be measured through a simple titration.

The system, as observed in Figure 2.27, exhibits gas bubbles formation, which is considered an essential factor in the gas-liquid mass transfer rate [144] and promotes the interaction between the triphasic system $(G - L - L')$ that contributes to the emulsion formation. A study to better understand the emulsion kinetics mechanism was performed considering the characteristics of the system [139]. Another approach adopts the application of a conductance meter and a dissolved oxygen meter into the water to measure the changes of benzoic acid and oxygen concentrations, respectively [176]. The studies provide illuminating results on the influence of bubble formation and how they affect bath emulsification. Authors considered bottom blowing more advantageous because it improves the bath circulation with the formation of smaller diameter bubbles.
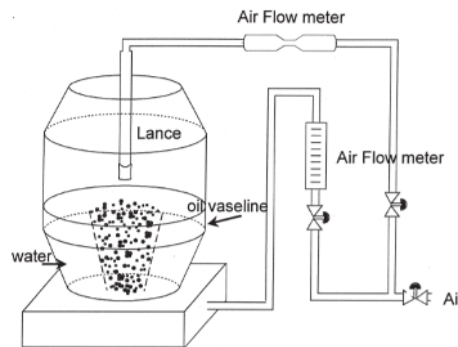
Figure 2.27: General diagram of the liquid-liquid transfer experimental setup [139].

The drop size in the gas-stirred system was considered an essential factor that impacts the mass transfer rate, and it became necessary to measure the size distribution of oil droplets and discuss the influence of the gas flow rate at the mass transfer rate. The methodology developed to perform this analysis employed a particular suction probe device [136]. It promoted an essential discussion about the importance of the volumetric mass transfer coefficients and their improvements based on the mechanism of drop size reduction and consequently enlarging the exchange area [138].

To improve the combined bottom stirring and top blown mass transfer rate, as introduced in other studies [145, 177, 140], it is essential to evaluate the parameters that affect the bottom gas injection in the steelmaking processes. The mass exchange is a method to estimate the gas injection efficiency according to the injection rate of the bottom stirring, as well as the number and configuration of the tuyeres [161, 133]. Those parameters promote a bath agitation that intensifies and can promote an impact on the mass transfer and the role of gas injection. Therefore, mass transfer measurement can be a method to

investigate the bath-mixing intensity as well as the influence of the bottom gas injection rate alone or the combined top and bottom gas-injection mechanisms [135].

It is possible to evaluate the mass transfer in different types of vessels such as Q-BOP and LD. The use of liquid paraffin and water is a method developed [128] to simulate the mass transfer between slag and hot metal by using naphthol as an exchange material. These investigations measured the naphthol concentration change in water extracted from liquid paraffin and concluded that the mass transfer rate between the slag and the metal phase was more close to the thermodynamic equilibrium in the Q-BOP than the LD process. It subsequently provided subsidies to compare the impact of a bottom blown converter and a top blown converter in the volumetric mass transfer coefficient [97]. Table 2.4 summarizes in more detail the methods used by each author to perform the mass transfer tests.

Table 2.4: Details of physical modeling for mass transfer investigations that used methods of CO_2 desorption and Liquid-Liquid Transfer.

Authors	Year	Focus		System		Blowing			Nozzle		Dimensioless Number				Ref.
		CD	LT	AW	AWO	B	T	TB	SH	MH	Fr	Re	We	NA	
Inada et al.	1976	•		•		•	•		•	•	•	•			[173, 84]
Nakanishi et al.	1980		•	•				•		•	•				[128]
Bessho et al.	1985	•		•		•			•					•	[174]
Schlarb et al.	1985		•		•	•		•		•		•			[137]
Paul et al.	1986		•		•	•	•			•	•				[97]
Koria et al.	1988		•		•			•		•	•				[133]
Zong et al.	1990	•		•				•		•	•	•			[178]
Frohberg et.al.	1990		•		•	•			•			•	•		[136]
Koria et al.	1991		•		•	•		•		•	•				[135]
Gerlach et al.	1993		•		•	•				•	•				[138]
Martín et al.	2002		•		•	•	•	•		•	•	•			[144]
Martín et al.	2004		•		•		•			•					[139]
Ajmani et al.	2005		•		•	•	•	•		•	•				[145]
Martín et al.	2005		•		•			•		•	•				[177]
Singh et. al.	2009		•		•	•				•				•	[161]
Wu et. al.	2010		•		•			•		•				•	[140]
Kawabe et. al	2017		•		•	•	•			•				•	[176]

Focus	CD → Carbon-Dioxide Desorption, LT → Liquid-Liquid Transfer.
System	AW → Air-Water, AWO → Air-Water-Oil.
Blowing	B → Bottom Stirring, T → Top Blowing, TB → Top Blowing + Bottom Stirring.
Nozzle	SH → Single Hole, MH → Multiple Hole.
Dimensioless	Fr → Froude Number, Re → Reynolds, We → Weber, NA → Not Available.

2.4.4.3 Cavity depth, cavity shape, splashing, slopping and projection rate

The jet penetration is a measure of how deep the lance oxygen jet penetrates the metallic bath, and different tuyeres configuration can result in different jet penetration values, those values usually are obtained in length. Jet penetration and jet impact are correlated, and usually, the jet impact reflects the stirring effectiveness of the oxygen jets

on metal and molten slag. These factors are adjusted by the change in lance height and gas flow rate; in other words, the blowing pattern [179]. An example of jet penetration measurement is shown on Figure 2.28.
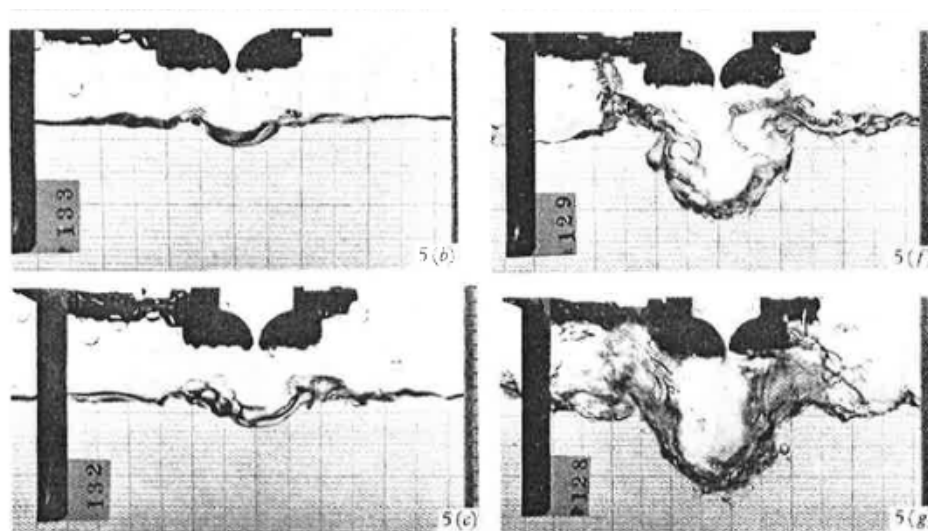
Figure 2.28: Experimental results to jet penetration into still water [180].

Jet penetration and decarburization area, also known as a cavity, have a significant relation with the interaction between the supersonic oxygen jet and the molten slag-metal bath, and it is crucial for a stable refining process and high operation efficiency [179].

Despite the relative reduction of the top blown jet as a source of stirring energy, after the introduction of the bottom stirring technology, the interest to develop the lance design, its operation, and the interaction among bottom stirring and top blowing has increased [181]. There are different publications available, and each author uses a different approach for the dimensionless number, such as Mach number [181, 182, 183] or Froude number [179, 180, 183, 96, 143]. Most of the authors evaluate the jet penetration and cavity using pictures of a water-gas system; besides that, some authors also calculated the depth using equations based on different variables and constants. The equations are based on momentum, lance height, fluid density, gravitational acceleration, and an independent constant [181, 96, 105] or even more complex to estimate the maximum depth of depression using fourteen variables [75]. Other analytical models can also be considered [180].

Some studies have developed more changes in the system, such as the lance angle or other different conditions. Banks and Chandrasekhara [180] studied the penetration of a high-velocity gas through a liquid surface using circular and plane jets penetrating a liquid surface in predetermined angles. They perform two kinds of experiments, one based on stagnation-pressure and the depth of surface depression and another related to the weight of the liquid displaced to the momentum of the jet. The different conditions in the system are also around the system, which can be different from water-gas. Luomala et al. [143] observed the splashing behaviour and distribution on BOF walls using connections in various places around the physical model, collecting splashes from the whole model cir-

cumference, considered significant when the cavities and bottom blowing/stirring plumes interaction results in irregular splashing distribution. Changes in the measurement techniques are also found, there are numerous ways to measure these parameters, from video and photo [180, 105, 75], sound frequency [121] to x-ray pulses [184].

Cheslak et al. [77] performed research concerning the cavities formed on liquid surfaces by a gaseous jet, and they studied two liquid surfaces, water, and wet fast-setting cement. The measurements using cement was stable because it could be obtained from a solidified structure. Some physical conditions and assumptions were combined to analyze the results. Ishikawa et al. [96] made a study aiming to observe jet penetration (cavity depth) and slopping in BOF using a water-nitrogen system. Cavity depth was measured using a scale on the wall of the vessel and observed the slopping region based at the maximum height in a uniform time spacing. The authors considered the reproducibility of the experiments low, so they considered a high error.

Some authors have also been studying jet stability and oscillation in industrial processes. They identified three different mechanisms related to the interaction between the top gas jet and the liquid surface, such as dimpling, splashing, and penetration behaviour, depending on the gas speed and the distance between the interface and the lance [183]. Regarding the slopping and projection rates, slag foaming is necessary for steel refining. However, when it occurs in excess, slopping, the projection of slag throughout the BOF mouth, may arise, disturbing the blowing operation in the BOF process [185]. While blowing, some metals droplets are ejected from the jet impact area, which generates droplets projection. As the slag is a heterogeneous system, with gas and some solid particles, the return of the droplets through the semi-liquid slag causes foaming and slopping [186].

Some of the investigations did not compare blowing parameters and just approached the methodologies. There are some interesting conclusions, Collins and Lubanska [75] showed that the maximum jet depression not necessarily has the highest mixing. Some authors [77, 104], have found relations between the jet momentum and the jet penetration in their results. Other authors have evaluated the wave formation effects. Li et al. [179] results showed the wave presence as gas-slag-metal interface instability reason. Lee et al. [183], has also evaluated the wave effects, but in refractory lining wear approach and concluded that the blowing generated waves could have its relation with refractory wear.

Comparing the parameters, Nordquist et al. [104] concluded that the jet penetration increases as the lance nozzles diameter and the lance height decreases, and also when the flow rate increases. Li et al. [179] showed that lance height and flow pressure have more influence on the interface behaviour and the cavity shape than superficial tension and viscosity. Evestedt and Medvedev [105] results showed that the jet penetration variance decreases as the lance height increases and increases as the gas flow rate increases.

Table 2.5 summarizes the literature review regarding jet-bath interaction.

Table 2.5: Jet-bath interaction authors and experiments details.

Authors	Year	Blowing		Angle		System			Focus				Dimensionless Number					Ref.
		T	TB	RA	AA	AW	AWO	O	CD	CS	SP	SL	Fr	Ma	Re	We	NA	
Collins et al.	1954	•			•	•			•								•	[75]
Banks et al.	1962	•		•		•			•				•				•	[180]
Cheslak et al.	1969	•		•		•		•	•	•							•	[77]
Ishikawa et al.	1972	•		•		•			•			•	•		•			[96]
Luomala et al.	2002		•	•		•					•		•			•		[143]
Lee et al.	2003	•			•	•		•	•				•	•	•	•		[183]
Evestedt et al.	2007	•		•		•			•	•							•	[105]
Naito et al.	2013	•		•		•			•	•				•				[181]
Belahouel et al.	2014	•	•					•	•	•						•		[187]
Li et al.	2015	•		•			•	•	•				•			•		[179]
Shi et al.	2016							•	•								•	[184]
Sabah et al.	2016	•		•		•	•			•							•	[121]
Wei et al.	2018	•		•		•			•	•				•	•			[182]

Blowing	T → Top Blowing, TB → Top Blowing + Bottom Stirring.
Angle	RA → Right Angle, AA → Another Angle.
System	AW → Air-Water, AWO → Air-Water-Oil, O → Others.
Focus	CD → Cavity Depth, CS → Cavity Shape, SP → Splashing, SL → Slopping.
Dimensioless	Fr → Froude Number, Ma → Mach, Re → Reynolds, We → Weber, NA → Not Available.

2.4.4.4 Others

Other different approaches are also found for the BOF cold modelling, Sabah and Brooks [121] developed a new methodology to determine the cavities in BOF using sound. This research is based on the analysis of the sound produced by the jet in a cold air-water model to distinguish various cavity modes. Wave analysis has shown that the amplitude of the sound increases as the mode changed.

2.4.5 Summary

Summarizing the cold model literature in Table 2.6, numerous researchers have studied the steel refining process. Most of the BOF cold models are mostly related to the effect of the jet at the bath surface or the design and pattern of top blowing lance and bottom stirring, individual or together. The main focus evaluated is related to the cavity shape, mixing time, mass transfer rate, mixing rate, and others such as supersonic nozzle jet, splashing rate, droplet size and amount, bath pattern, heat transfer. There are many measurement techniques available in the literature. Most of the measurements are related to image analysis, conductivity meter, mass transfer technique, droplet sampler, colourimetry, sound analysis, oscillograph, and others. Only a few researchers validated their experiments in hot models or industrial practices.

Complete similarity conditions, between the model and prototype, can be attained if key dimensionless numbers are the same. Considering the BOF physical modelling, the dynamic similarity is ensured by the Froude and Reynolds numbers equivalence. Weber's number is used to keep the interface state [19]. Many works did not evaluate the similarity conditions, but when this subject is evaluated, the Froude number was applied in most of them [128, 188, 119, 144, 148, 145, 112, 140, 115, 162]. Few researchers considered further dimensionless numbers such as Reynolds and Weber [133, 100, 65, 123, 157].

The simulation of oxygen blowing through the top lance, in many cases, was performed by a single hole and-or multiple hole lance. Nevertheless, there is limited literature regarding cold modelling blowing with multiple hole "laval" nozzle [69, 100, 144, 65, 123, 113, 115, 157]. Regarding the shape, many experimental cold modelling was performed in a cylindrical tank, and the BOF shape was available in few investigations [128, 144, 123, 140, 115, 162, 157].

Table 2.6: Review of the various BOF physical modeling publications.

Author	Year	BOF	T	TB	SH	MH	DBD	AW	AWO	O	CS	MT	MTR	ME	O	IA	C	MTT	DS	O	HM	ID	Reference
			Blowing		Nozzle			System			Focus					Measurement					Validation		
Newby et al.	1949		•		•			•			•					•							[74]
Collins et al.	1954		•		•			•			•					•							[75]
Glass et al.	1955, 1957	•	•		•				•	•	•				•	•				•	•	•	[78, 79, 80]
Banks et al.	1962, 1963	•	•		•			•			•				•					•			[189, 190]
Flinn et al.	1963, 1964, 1967	•	•		•	•		•			•				•	•				•	•	•	[76, 82, 69]
Ishikawa et al.	1972	•	•		•	•				•	•				•	•							[96]
Inada et al.	1976	•	•		•					•		•	•						•				[84]
Nakanishi et al.	1980, 1982	•		•		•	•	•				•	•	•			•		•		•	•	[128, 130]
Kai et al.	1983	•		•		•	•	•			•	•		•			•					•	[191]
Szekely et al.	1985							•							•				•				[159]
Schlarb et al.	1985	•		•		•			•			•	•						•				[137]
Koria et al.	1987, 1991	•		•	•	•			•		•	•	•	•		•					•		[94, 135]
Ghosh et al.	1988	•		•			•	•				•		•		•							[47]
Ramani et al.	1988	•		•		•		•				•				•							[188]
Gerlach et al.	1990, 1993	•		•		•		•			•	•	•					•					[138, 136]
Roth et al.	1995, 1999	•		•	•	•	•		•	•					•		•		•				[8, 141]
Koch et al.	2002	•		•			•								•		•						[160]
Martin et al.	2002, 2005, 2008	•		•		•	•	•				•	•	•	•	•	•		•	•			[144, 27, 139]
Morales et al.	2002	•		•	•			•			•	•					•		•	•			[119, 118]
Luomala et al.	2002	•		•		•		•							•				•				[100, 142, 127]
Meidani et al.	2004, 2005	•	•			•		•			•	•					•			•			[65, 68]
Chatterjee et al.	2005	•		•	•	•	•		•			•	•				•	•				•	[145, 146, 147, 161]
Wei et al.	2005, 2007, 2010						•	•				•	•				•						[148, 28, 149]
Nordquist et al.	2006	•	•		•			•			•					•							[104]
Bruckhaus et al.	2007	•		•		•		•							•	•						•	[150]
Evestedt et al.	2007	•	•		•			•			•					•							[105]
Maia et al.	2007, 2013, 2014	•	•			•		•			•					•				•			[123, 67, 124]
Asai et al.	2009	•	•			•		•				•				•							[112]
Wu et al.	2010	•		•		•	•		•			•	•	•					•				[140]
Asahara et al.	2011	•	•			•		•			•					•							[113]
Millman et al.	2011	•	•			•		•							•	•							[59]
Sichen et al.	2012	•	•		•					•	•				•	•							[111]
Zhou et al.	2014, 2015	•				•		•			•	•		•		•	•					•	[115, 153, 154, 155]
Brooks et al.	2016, 2017	•	•			•			•		•				•	•				•	•		[121, 114]
Carvalho et al.	2017, 2018, 2019	•		•		•	•		•		•	•	•		•	•	•	•	•	•		•	[157, 125, 64, 158, 30, 156]
Quiyoom et al.	2017	•					•	•				•				•							[162]
Cao et al.	2018	•	•			•			•		•	•				•	•						[120]

Blowing	T → Top Blowing, TB → Top Blowing + Bottom Stirring.
Nozzle	SH → Single Hole, MH → Multiple Hole
Bottom	DBD → Different Bottom Design or Pattern.
System	AW → Air-Water, AWO → Air-Water-Oil, O → Others.
Focus	CS → Cavity Shape, MT → Mixing Time, MTR → Mass Transfer Rate, ME → Mixing Energy, O → Others.
Measurements	IA → Image Analysis, C → conductivity meter, MTT → Mass Transfer Technique, DS → Droplet Sampler, O → Others.
Validation	HM → Hot Model, ID → Industrial Scale.

3 Objectives

The current work aimed at investigating the improvements on the BOF metallurgical results, introduced by improving the mixing time and mass transfer rate due to a gradient of apparent density, caused by different bottom stirring flow zones and slag layer. A new cold model was built, to make this investigation viable, considering the complete similarity and shape with the industrial BOF to attend the general theory of models mentioned in Section 2.3.1. The lance tip used for cold model blowing was a multiple-hole type developed with the same Laval nozzle characteristics as applied in the industrial process. A series of single and multi-phase experiments were carried out in the laboratory and validated in the industrial operations of Ternium Brazil, different configurations of top blowing, bottom stirring, and both together were evaluated. According to the literature review, there are a few references available with these characteristics. Experimental heats took place in a running plant with a production capacity of 5 million $t/year$, and challenging work was successfully performed considering all environmental aspects and workers' safety and health as a first priority.

According to previous publications, Section 2.4, cold modelling has been popularly applied to perform BOF investigations, and mixing efficiency has played a vital role in assessing the influence of each parameter. Individual studies of top blowing or bottom stirring are widely available, and the impact of each parameter is well known. The main factors to influence top blowing are related to lance parameters such as the number of nozzles, nozzle angle, critical diameter, back pressure, and distance between lance tip and bath level. Bottom stirring is main affected by total inert gas flow, bottom design, bottom element type, and others. Nevertheless, cold model investigations considering the top blowing and bottom stirring at the same time are limited. The aim of this work was to investigate the combined top blowing and bottom stirring of an Industrial 330 t BOF within cold model investigations and industrial validation.

3.1 Cold Modelling Results vs Industrial Results

This research work is divided into two main Work Packages (WP) to investigate the improvements on BOF metallurgical results introduced by different bottom stirring flow zone: Laboratory experiments at LaSiP (WP1) and Industrial experiments at Ternium BR Steel Plant (WP2). Figure 3.1 shows a schematic structure of the project, divided

into smaller different WP subtopics and presented in the next sections.
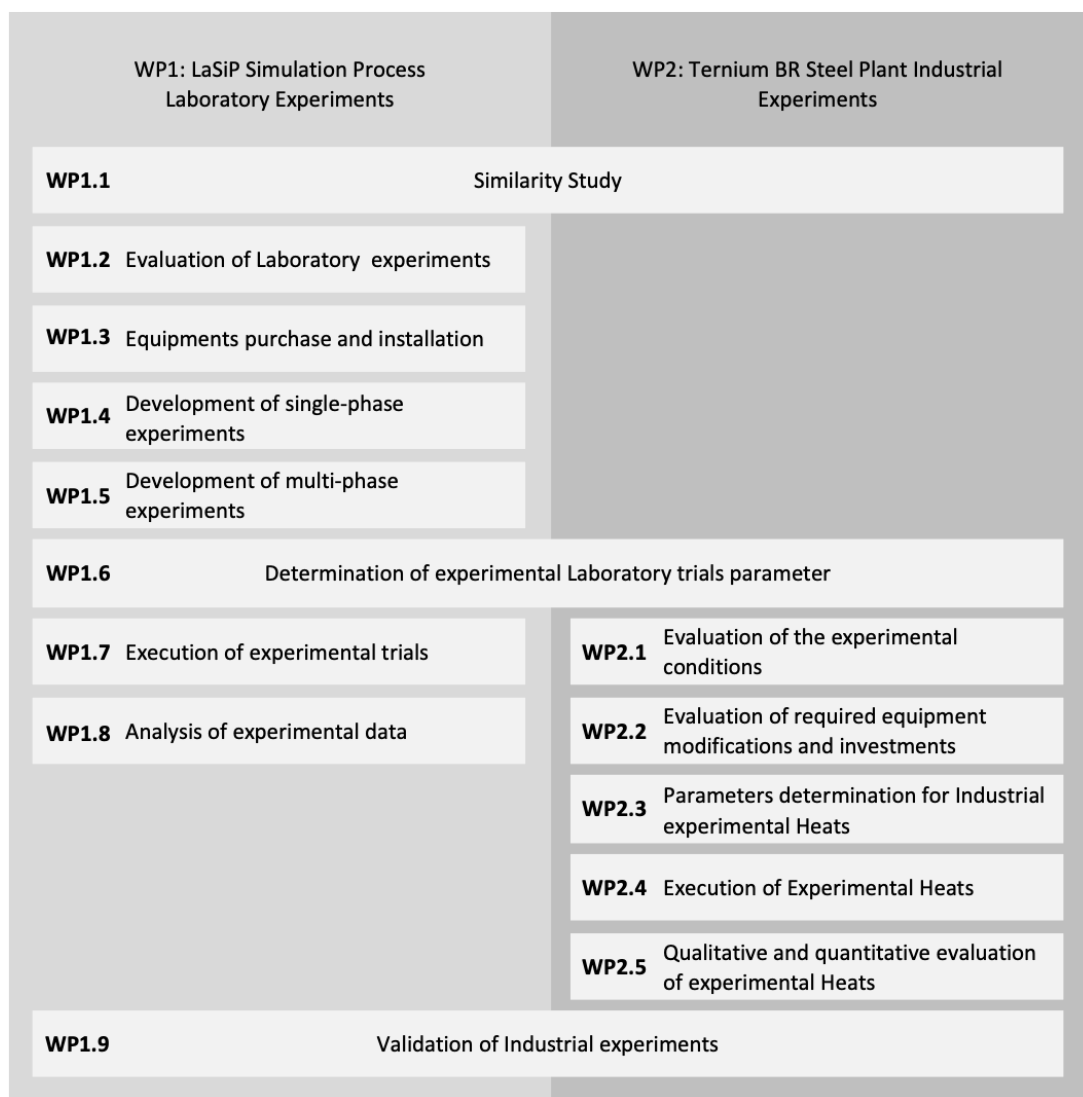
Figure 3.1: Schematic representation of the work packages.

3.1.1 LaSiP - Laboratory Experiments (WP 1)

The main task was to develop a suitable BOF cold model to investigate the mixing time and mass transfer under multi-phase conditions in similarity to the 330 t industrial BOF.

- A similarity study (WP 1.1) was developed for subsidising the construction of the cold model in a complete similarity with the industrial 330 t BOF to attend the general theory of models mentioned in Section 2.3.1.

- Evaluated the laboratory experiments (WP 1.2), necessary to assess the available laboratory equipment and resource conditions to define equipment purchase and installations.

- Developed the measurements methodologies. Essential developments regarding experiments measurements were necessary, outputs such as mixing time, mass transfer and some other indirect measurements needed to be known precisely. The measurement methods were defined, as well as the necessary modifications in the available equipment and layout.

- Developed the single-phase experiments (WP 1.4) consists in the cold simulation using water to reproduce the liquid steel behaviour and compressed air to simulate the oxygen blowing and bottom stirring in a plexiglass vessel, simulating the $330\,t$ industrial BOF. Development of the multi-phase experiments (WP 1.5), consists of the single-phase experiments plus oil-based element to simulate the slag phase.

- Determined the parameters of the experimental trials (WP 1.6), according to the industrial process requirements. A "brainstorm" at Ternium BR Steel Plant between the Managers, Process and Maintenance Engineers was necessary to understand the equipment and process capabilities as well as to equalise the expectations between both sides; research project and industry. This topic was necessary to determine the matrix of tests for the next topic.

- Execution of experimental trials according to previous items (WP 1.7).

- Analysis of experimental laboratory data (WP 1.8) was based in a qualitative and quantitative survey, according to the measurements available and previously defined in the (WP 1.4) and (WP 1.5). Qualitative analysis was defined through image analysis, and essential process patterns were shown. Statistics analysis were necessary to provide a reliable quantitative survey, crucial for this research work to determine precise configurations and parameters for the industrial experiments at the Ternium BR Steel Plant.

- Validation of Industrial Experiments (WP 1.9) in the laboratory was proposed to figure out some possible doubts after the execution of Industrial experiments (WP2).

3.1.2 Industrial experiments at Ternium BR Steel Plant (WP 2)

Industrial experiments at Ternium BR Steel Plant (WP2) were proposed to validate the Laboratory Simulations (WP1) results. The recommended configurations and parameters suggested in the Laboratory experiments were tested.

- Evaluation of the experimental conditions (WP 2.1) is a crucial step to understand the equipment and process capabilities using the available technology as well as all risks involved. Workers' safety and health were the first priority, and could not be neglected. It is essential to remind that the experimental heats were going to

take place in a running plant with the production capacity of 5 million $t/year$. Interference in the operational routine should be the minimum possible, and risk for the equipment was not acceptable. This topic was fundamental to determine the required equipment modifications and necessary investments (WP 2.2).

- Determine the parameters for the experimental industrial trials (WP 2.3) was proposed according to the results achieved in the Laboratory Simulations (WP 1).

- Execution of experimental heats (2.4) needed to be carefully conducted, parameters and configurations proposed in advance should be strictly followed and all instruments for measurement running according to the maintenance plan. It is also essential to observe all operational conditions to understand some outlier results; anomaly heats should be noted. All significant process and equipment variables available on HMI (Human Machine Interface) and Level 2 (Process Computer) needed to be tracked and saved for further analysis.

- Qualitative and quantitative evaluation of experimental heats (WP 2.5) was an important step to validate the results of Laboratory Simulations (WP 1), a statistical assessment of metallurgical results obtained in the experimental heats (WP 2.4) was the key for this topic. Regular process samples and measurements, as well as extra samples, could be used in this analysis. E.g., hot metal samples, in-blow and end-blow measurements and steel samples, as well as the slag samples at the end-blow.

3.2 Different bottom configuration to improve BOF reactions

Enhance the metallurgical results were expected by improving the mixing time, and mass transfer for the BOF process based on the knowledge developed through the Working Packages (WPs) proposed. Specific expected results for each WPs are shown below.

The main results expected through the Laboratory experiments at LaSiP (WP1) were;

- Development of Similarity criteria based on dimensionless numbers to build a new model based on the industrial 330 t BOF;

- Development of methods to measure mixing time and mass transfer for the single and multi-phase simulations;

- Execution of experimental trials according to the matrix defined in accordance to the Steel Plant team;

- Define precise configurations and parameters for the industrial experiments at Ternium BR Steel Plant.

The main results expected with the Industrial experiments at Ternium BR Steel Plant (WP2) were;

- Validate the configurations and parameters proposed by the Laboratory Experiments (WP1);

- Execution of experimental heats in the 330 t BOF with safety for the workers and no risk for the equipment;

- Statistical assessment of metallurgical results obtained in the experimental heats.

4 Modelling Developments and Trials

Formulating a robust similarity study to attend the general theory of models mentioned in Section 2.3.1 was required to assess the industrial BOF's cold model quantitative results. The primary condition analysed was the geometric similarity, also known as shape similarity, in which the ratio of any length in both systems is kept the same. It is then necessary to analyse the metallurgical parameters through the kinematic (motion) and dynamic (forces) similarity. Novel dimensionless numbers (Fr^*_{LaSiP}, Eo^*_{LaSiP}, We^*_{LaSiP}, Q^*, and E^*) were introduced considering the effects of the multi-nozzle supersonic lance, slag phase and bottom stirring gas to develop complete similarity.

It was also necessary to evaluate the available laboratory equipment and resource conditions, as well as understand the equipment and process capabilities using the current technology in the industrial plant to optimise the required equipment modifications and investments. Another critical step in developing this work was related to cold modelling experiment measurements, and the elaboration of the right methodology according to each simulation, with individual characteristics, was fundamental to get precise analyses.

4.1 Similarity between LaSiP (model) and Ternium BR (prototype)

This research adopted water to simulate the liquid steel for biphasic experiments, and oil to simulate the multiphase experiments' slag phase. The main reason to use the mentioned liquids is related to similar kinematic viscosity at ambient temperature, Table 4.1.

Table 4.1: Comparison between properties of the industrial process and cold model.

| Property | Symbol | Unit | | Industrial Process | | Cold Model | |
				Steel	Slag	Water	Oil [192]
Temperature	T	°C	-	1640	1640	25	25
Density	ρ	kg/m^3	$.10^3$	6.90 [193]	2.50 [194]	1.00 [195]	0.87
Dynamic Viscosity	μ	$kg/(m.s)$	$.10^{-3}$	5.50 [14]	82.50 [64]	1.00 [195]	55.30
Kinematic Viscosity	ν	m^2/s	$.10^{-6}$	0.80 [21]	33.00 [21]	1.00 [196]	63.6
Interfacial Tension	σ	N/m	-	1.150 [14]	0.300 [64]	0.073 [197]	0.052

LaSiP (Process Simulation Laboratory) has a tradition to simulate the BOF process

dating back to 2002. Before this work started, another BOF cold model setup was available, and it was built similarly with a 220 t BOF on a 1/8 scale. To feed the blowing lance with enough pressure, an air compressor of 22.5 kW was available. This equipment supplies a maximum pressure of $7.87x10^5$ Pa, a nominal flow rate of 189 Nm^3/h, and a maximum flow rate at lance nozzle of 160 Nm^3/h due to a pressure drop between the air compressor system and the lance nozzle [124]. Figure 4.5 shows the LaSiP plexiglass converter built on a scale of 1 : 10, in similarity to Ternium BR 330 t BOF.
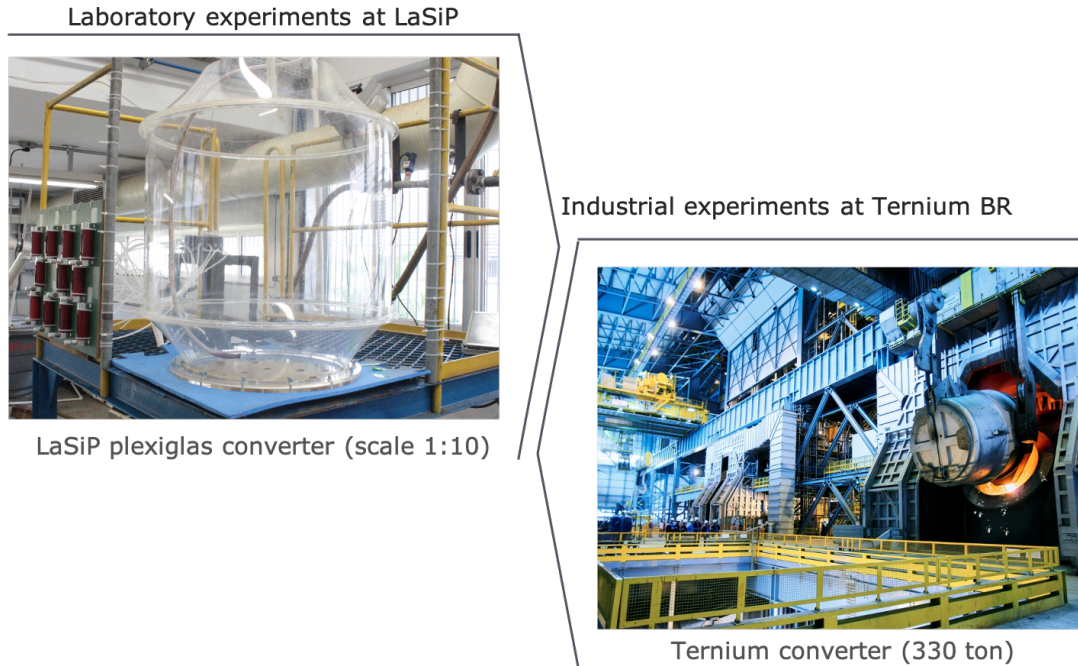
Figure 4.1: Cold physical model similar to Ternium Brazil's 330 t BOF developed at LaSiP.

4.1.1 Geometric Similarity

An investment in new air compressor was not feasible due to costs and laboratory infrastructure limitations. Consequently, this maximum lance flow rate defined the boundary conditions to build the new 330 t BOF cold modelling with a geometric scale of 1/10, Equation 4.1.

$$\lambda = \left(\frac{D_{cm}}{D_{ind}}\right)_{BOF} = \frac{1}{10} \tag{4.1}$$

Where, λ – scale factor $(-)$, D_{cm} – cold model diameter (m), and D_{Ind} – industrial BOF diameter (internal) (m).

Table 4.2, introduces the main dimensions for the industrial model (real scale) and the proposed cold model. The scale factor is assumed to be the trunnion ring area's internal diameter to perform the geometric similarity. Ternium Brazil BOF has an outstanding ratio of internal volume per tapped steel $(1\,m^3/t_{Steel})$. The cold model needs to consider this premise.

Table 4.2: BOF vessel similarity and scale relations.

Variable	Symbol	Unit	Industrial	Cold Model	Scale
BOF Diameter	D_{BOF}	m	7.156	0.716	1/10
BOF Height	H_{BOF}	m	10.086	1.009	1/10
Bath Height	H_{Bath}	m	1.715	0.1715	1/10
Bath Level Distance	H_{BLD}	m	2.20	0.451	1/20

After defining the BOF downscale and geometric similarity, the following step was the development of a plexiglass model project. The search for a viable project, considering a smooth execution with feasible costs, an adjustment in the internal profile to reduce the details such as small steps and bends was proposed. An increased number of details in the Plexiglass requires sophisticated machines and expert human resources, which reduces the number of companies available to execute the project, and increases costs and delivery time. Figure 4.2 shows the final dimensions of the industrial 330 t BOF.
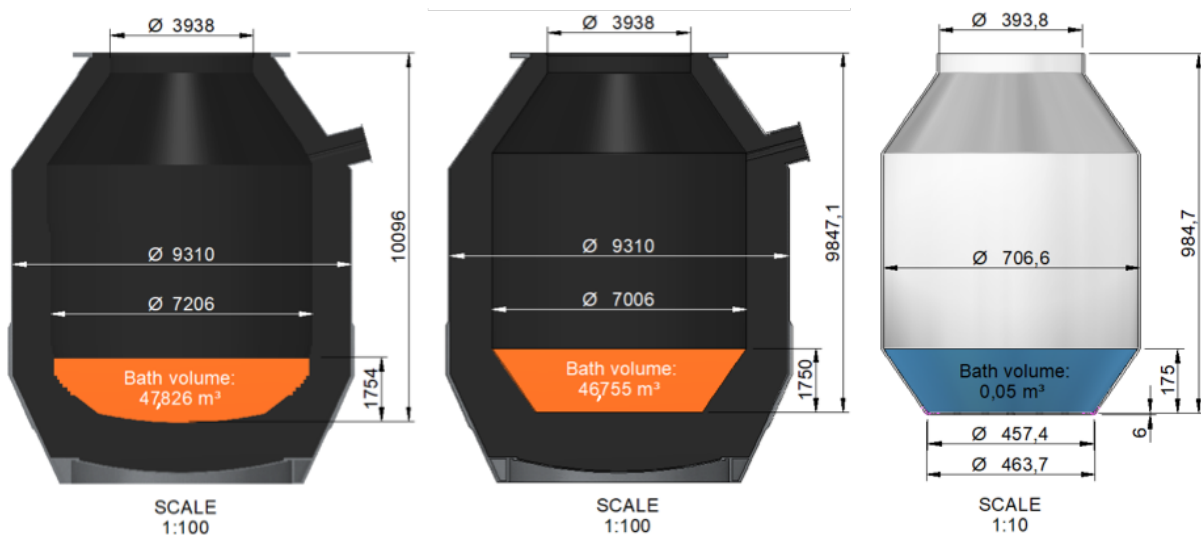
Figure 4.2: Ternium Brazil's 330 t BOF, downsize steps to build a similar cold physical model at LaSiP.

Despite the geometry and detail simplification, Figure 4.2, the main characteristics followed the original BOF available in the industry, keeping the same Bath Level ratio. The Plexiglass model project only considered the internal BOF dimensions because it defines the boundary volume where the fluid flow phenomena occur.

4.1.2 Nozzle Similarity

The lance nozzles of the physical model should be designed in such a way that the desired momentum input rate is obtained. Since the gas velocity at the nozzle exit is usually supersonic, compressible effects should be considered in the calculations [198].

It is usually assumed that the fluid is an ideal gas and that the flow in the nozzle is adiabatic and without viscous losses so that the fluid state change is isentropic. Under these assumptions, the following equations are valid [199]:

$$\frac{T_2}{T_1} = \left(\frac{p_2}{p_1}\right)^{\frac{\gamma-1}{\gamma}} \tag{4.2}$$

$$\rho_{gas} = \left(\frac{M}{1000}\right) . \frac{p}{RT} \tag{4.3}$$

Where, T – absolute temperature (T), p – pressure (Pa), γ – heat capacity ratio of the gas, $\gamma = \frac{C_p}{C_v}$, C_p – heat capacity at constant pressure ($J.kg^{-1}.K^{-1}$), C_v – heat capacity at constant volume ($J.kg^{-1}.K^{-1}$), the subscripts 1 and 2 stand for two generic states, M – gas molar mass ($g.mol^{-1}$), 1000 is a unit conversion factor, and R – universal gas constant ($J.mol^{-1}.K^{-1}$).

Also, a steady-state energy balance in the nozzle leads to [199]:

$$T_2 \left[1 + \left(\frac{\gamma-1}{2}\right).(Ma_2)^2\right] = T_1 \left[1 + \left(\frac{\gamma-1}{2}\right).(Ma_1)^2\right] \tag{4.4}$$

Where Ma is the Mach Number:

$$Ma = \frac{\overline{\nu_{gas}}}{\nu_{gas}} \tag{4.5}$$

$$\nu_{gas} = \sqrt{\gamma \frac{p}{\rho_{gas}}} = \sqrt{\gamma \frac{RT}{\frac{M}{1000}}} \tag{4.6}$$

Where, $\overline{\nu_{gas}}$ – local gas velocity ($m.s^{-1}$), and ν_{gas} – the speed of sound in the gas ($m.s^{-1}$).

There are at least three strategies for the nozzle design. The first considers a geometrically similar exit diameter, the second one assumes the equality of Mach number between the physical and industrial models, and the third one specifies the stagnant pressure. The last strategy is interesting since the stagnant pressure is determined by the compressor used in the experiments. Here, the calculation order will be presented for the third strategy. However, the same equations also apply to the other strategies [198].

In a hypothetical gas reservoir that feeds the nozzle (subscript 0), the fluid is virtually at rest, $Ma_0 = 0$. The temperature is equal to the ambient temperature, and the pressure is set by the system compressor so that Ma_0, T_0, and p_0 are known. At the nozzle exit (subscript e), the pressure p_e is known and equal to the ambient pressure. Also, at the nozzle throat of the convergent-divergent nozzle (subscript t), $Ma_0 = 1$ [198].

First, the temperature at the nozzle exit T_e is calculated from p_e, T_0, and p_0 using Equation 4.2. Then, the Mach number at the nozzle exit Ma_e is calculated from T_e, Ma_0, and T_0 using Equation 4.4. Subsequently, the gas density, the speed of sound, and

the gas velocity at the nozzle exit are successively calculated using Equation 4.3, 4.6 and 4.5. Finally, the nozzle exit diameter is calculated from the criterion of equality of the modified Froude number, Equation 4.10 [198].

Regarding the nozzle throat, the gas temperature T_t is calculated first from Ma_t, T_0, and Ma_0 using Equation 4.4. Then, the gas density, the speed of sound, and the gas velocity at the nozzle throat are successively calculated using Equation 4.3, 4.6 and 4.5. Finally, the throat diameter is calculated from a mass balance between the throat and the exit [198].

$$D_t = \sqrt{\frac{(\rho_{gas}.\overline{\nu_{gas}})_e}{(\rho_{gas}.\overline{\nu_{gas}})_t}}.D_e \qquad (4.7)$$

Where, D – local diameter of the internal transversal section of the nozzle (m).

Researchers often need to use the same laboratory structure (e.g. compressor and lance nozzles) to model different operational conditions of the same converter (e.g. bath-lance distance and gas flow rate) to study different converters. In this case, the criterion of equality of the modified Froude number may be attained changing the bath-lance distance of the physical model to the non-geometrically similar value [198].

This procedure is only valid if the model parameter K is independent of the bath-lance distance. When this hypothesis does not hold, an average K value might be employed to scale up the industrial equipment's physical model results. However, some errors may be introduced in the predictions [198].

The primary factor for lance nozzle modelling was the air compressor capacity with a maximum flow rate at lance nozzle of 160 $Nm3/h$. Due to the pressure differences between the industrial environment and the cold model conditions, the Mach number was impacted, Equation 4.5 makes it necessary to use an adapted geometric similarity between the converter and the lance tip. Table 4.3 introduces the jet properties comparing the industrial equipment and the cold model.
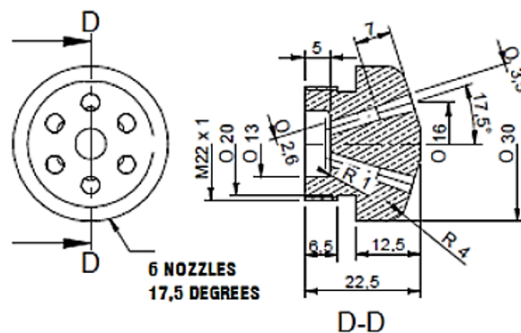
Figure 4.3: Laboratory supersonic lance nozzle design, values in millimeter (mm).

This work does not intend to describe the industrial lance tip design. Nevertheless, the lance tip similarity was designed considering the industrial model and the new plexiglass project, Table 4.4. Figure 4.3 shows the cold model converging-diverging nozzle design.

Table 4.3: Jet Properties [64].

Property	Symbol	Unit	Industry	Cold Model
Pressure dimensionless ratio	P_{exit}/P_0	-	0.07	0.15
Temperature dimensionless ratio	T_{exit}/T_0	-	0.47	0.59
Pressure of gas jet at the throat	P_0	Pa	833,000	443,000
Density of gas jet at the throat	ρ^*	$kg.m^{-3}$	12.86	6.19
Temperature of gas jet at the throat	T^*	K	249.37	249.37
Mach number	Ma	-	2.39	1.91
Area dimensionless ratio	A_{exit}/A^*	-	2.41	1.57
Pressure of gas jet at the nozzle exit	P_{exit}	Pa	108,300	123,800
Density of gas jet at the nozzle exit	ρ_{exit}	$kg.m^{-3}$	2.96	2.47
Temperature of gas jet at the nozzle exit	T_{exit}	K	141.00	174.00
Sound speed of gas at the nozzle exit	V_s	$m.s^{-1}$	225.00	264.00
Velocity of gas jet at the nozzle exit	V_{exit}	$m.s^{-1}$	540.00	503.00
Area at the nozzle exit	A_{exit}	m^2	$2.88x10^{-3}$	$8.60x10^{-6}$
Total area at the nozzle exit	A_{exit}^{total}	m^2	$1.73x10^{-2}$	$5.16x10^{-5}$
Gas flow rate	Q_{exit}^{total}	$m^3.s^{-1}$	9.34	0.03

4.1.3 Jet Penetration Similarity

Jet penetration is a measure of the bath surface deformation promoted by the high-speed gas jet's impact, which leaves the lance nozzle. Jet penetration is not only a physical model output of practical relevance, and an adequate prediction of jet penetration is also required to ensure the geometric similarity of the model regarding bath shape [198].

To introduce new terms related to the specific parameters available for each BOF operation, this research proposed an adaptation of the Froude and Weber numbers previously established by Meidani et al. [68] (Equations 2.26 and 2.28). Moreover, a new dimensional analysis through the Eötvös number for BOF converters was also proposed.

The new terms raised in Fr^*_{LaSiP}, We^*_{LaSiP} and the proposed Eo^*_{LaSiP} originated from the jet penetration energy balance proposed by [32], Equation 2.7, the most general equation for predicting jet penetration considering gas hold-up, slag phase and lance tip design parameters. After some simple algebraic manipulations, the Equation 2.7 can be rewritten as:

$$\frac{\pi}{2.K^2}.P^*.(1 + P^*)^2.\left[1 + (P^*)^{-2}.\frac{1}{Eo^*_{LaSiP}}\right] = Fr^*_{LaSiP} \qquad (4.8)$$

Where, P^* – dimensionless jet penetration, Eo^*_{LaSiP} – modified Eötvös number, and

Table 4.4: Supersonic multi-nozzle BOF lance similarity.

Variable	Symbol	Unit	Industrial	Cold Model
Number of nozzles	n	-	6	6
Diameter at the nozzle exit	d_{exit}	m	0.0606	0.0033
Diameter at the nozzle throat	d_{throat}	m	0.0439	0.0026
Divergent section height	h_{laval}	m	0.086	0.015
Angle of divergent section	$\alpha_{divergent}$	°	11.0	2.5
Angle of individual nozzle	θ_{nozzle}	°	17.5	17.5

Fr^*_{LaSiP} – the modified Froude number. These dimensionless numbers are given by:

$$P^* = \frac{P}{BLD} \tag{4.9}$$

$$Fr^*_{LaSiP} = \frac{Inertia\ Force}{Gravitational\ Force} = \frac{\pi}{4}.\frac{\rho_{gas}.(V_{exit}.d_{exit}.cos(\theta_{nozzle}))^2.n}{\rho_{mix}.g.BLD^3} \tag{4.10}$$

$$Eo^*_{LaSiP} = \frac{Gravitational\ Force}{Surface\ Tension\ Force} = \frac{\rho_{mix}.g.BLD^2}{2.cos(\theta_{nozzle}).\left(\frac{\sigma_{steel}+\sigma slag}{2}\right)} \tag{4.11}$$

To the best authors' knowledge, no form of the Eötvös number has been used for the BOF converters' dimensional analysis yet. Previous works have evaluated the relative importance of the surface tension effects through some form of the Weber number. For instance, one might adopt the modified Weber number defined as Equation 4.13. In this case, the dimensionless jet penetration equation would depend on $\frac{Fr^*_{LaSiP}}{We^*_{LaSiP}}$ $\left(= \frac{1}{Eo^*_{LaSiP}}\right)$. Note that the condition $(We^*_{LaSiP}) \gg 1$ is not enough to ensure that the surface tension effects are negligible since the term $\frac{Fr^*_{LaSiP}}{We^*_{LaSiP}}$ may not vanish if $(Fr^*_{LaSiP}) \gg 1$. So, the use of the modified Eötvös number is recommended [198].

$$We^*_{LaSiP} = \frac{Inertia\ Force}{Surface\ Tension\ Force} = \frac{Inertia\ Force}{Gravitational\ Force}.\frac{Gravitational\ Force}{Surface\ Tension\ Force} \tag{4.12}$$

$$We^*_{LaSiP} = Fr^*_{LaSiP}.Eo^*_{LaSiP} = \frac{\pi}{4}.\frac{\rho_{gas}.(V_{exit}.d_{exit})^2.cos\theta_{nozzle}.n}{BLD.(\sigma_{steel}+\sigma_{slag})} \tag{4.13}$$

Hence, the physical model will have the same P^* as the industrial BOF, and the geometric similarity of the bath shape will be attained if Eo^*_{LaSiP} and Fr^*_{LaSiP} of the physical model are equal to these values of the industrial BOF.

The equality criteria of the modified Eötvös number (Eo^*_{LaSiP}) restricts excessively the

working fluids that could be employed in the physical model. Fortunately, $Eo^*_{LaSiP} \gg 1$ for the systems studied so that the effect of (Eo^*_{LaSiP}) on P^* is very small. As a consequence, this criterion is usually neglected in practice. On the other hand, the criterion of equality of the modified Froude number (Fr^*_{LaSiP}) specifies the momentum input rate in the physical model. In general, this criterion should be satisfactory [198].

The concept of density of the slag-metal mix was previous explained in Equation 2.8. When the gas hold-up and slag phase are considered in Equations Fr^*_{LaSiP}, We^*_{LaSiP} and the proposed Eo^*_{LaSiP}, the density of the slag-metal mix is affected by the bottom stirring gas injection, and the density is lower for higher bottom stirring flow rates, causing more movement in the bath level.

Where, ρ_{gas} – density of the gas at the nozzle exit $(kg.m^{-3})$, V_{exit} – velocity of gas jet at the nozzle exit $(m.s^{-1})$, d^2_{exit} – diameter at the nozzle exit (m), θ_{nozzle} – angle of individual nozzle $(°)$, n – number of nozzles in lance tip $(-)$, ρ_{steel} – bath density $(kg.m^{-3})$, g – gravity acceleration $(m.s^{-2})$, BLD – Bath Level Distance (m), H_{BL} – height of static bath level (m), H_{SL} – height of static slag level (m), σ_{steel} – liquid steel interfacial tension $(N.m^{-1})$, σ_{slag} – slag interfacial tension $(N.m^{-1})$, P – jet penetration (m), ρ_{mix} – density of the slag-metal mix $(kg.m^{-3})$, BLD – Bath Level Distance (m), W_{gas} – mass of bottom stirring gas (kg), W_{bath} – mass of static steel bath (kg), W_{slag} – mass of static slag layer (kg), $V_{static.bath}$ – volume of static steel bath (m^3), Q_{gas} – bottom stirring gas flow rate $(m^3.s^{-1})$, and V_{slag} – volume of static slag layer (m^3).

4.1.4 Bottom Stirring Similarity

In the BOF process, bottom stirring may be carried out by multiple tuyeres with a relatively low flow rate per tuyere (a mathematical definition for "low flow rate" is given later). In this case, the gas's momentum input rate does not contribute significantly to the bath mixing. Instead, the buoyancy force due to the difference of densities between the bath and the injected gas is responsible for the stirring. In this context, the following ratio controls the system [198].

$$\frac{Inertia\ force\ of\ the\ bath}{Buoyancy\ force} \approx \frac{\rho_{bath}.(V_{bath}.H_{bath})^2}{(\rho_{bath} - \rho_{gas}).g.H^3_{bath}} \tag{4.14}$$

Where, ρ_{bath} – density of the bath $(kg.m^{-3})$, V_{bath} – characteristic bath velocity $(m.s^{-1})$, H_{bath} – height of static bath level (m), ρ_{gas} – density of the gas at the nozzle exit $(kg.m^{-3})$, and g – gravity acceleration $(m.s^{-2})$. Since $\rho_{bath} \gg \rho_{gas}$, Equation 4.14 can be simplified to:

$$\frac{Inertia\ force\ of\ the\ bath}{Buoyancy\ force} \approx \frac{(V_{bath})^2}{g.H_{bath}} \tag{4.15}$$

According to the dimensional arguments of Asai et al. [200], for convection-dominant

flows,V_{bath} is related to the mixing power density of the system, ε^* (W/m^3), by:

$$V_{bath} \approx \left(\frac{\varepsilon^*.H_{bath}}{\rho_{bath}} \right)^{\frac{1}{3}} \tag{4.16}$$

According to the analysis of Mazumdar and Evans [163]:

$$\varepsilon^* = \frac{Energy\ input\ rate}{Bath\ volume} \approx \frac{(\rho_{bath} - \rho_{gas}).g.Q_{total}.H_{bath}}{(H_{bath})^3} \tag{4.17}$$

Where, Q_{total} is the total tuyere gas flow rate $(m^3.s^{-1})$, or the individual tuyere flow rate Q_{tuyere} times the number of available tuyeres n_{tuyere}. Substituting the Equation 4.17 in the Equation 4.16 and simplifying the result $\rho_{bath} \gg \rho_{gas}$, one gets:

$$V_{bath} \approx \left(\frac{g.Q_{total}}{H_{bath}} \right)^{\frac{1}{3}} \tag{4.18}$$

Substituting the Equation 4.18 in the Equation 4.15 and manipulating the powers, the final result is obtained:

$$\frac{Inertia\ force\ of\ the\ bath}{Buoyancy\ force} \approx \left[\frac{Q_{total}}{g^{1/2}.(H_{bath})^{5/2}} \right]^{2/3} \tag{4.19}$$

Equation 4.19 suggests the use of the non-dimensional gas flow rate Krishnapisharody and Irons [201], Q^*, during the design of BOF physical models:

$$Q^* = \frac{Q_{total}}{g^{1/2}.(H_{bath})^{5/2}} \tag{4.20}$$

Specifically, the total gas flow rate of the tuyeres of the physical model should be set imposing the equality of Q^* between the physical model and the industrial BOF. Also, the fractions of the total gas flow rate injected in each tuyere should be equal in the two cases to provide the same special distribution of the mixing power in the physical model and the industrial BOF.

When the tuyere gas flow rate is very high, the injected gas forms a jet over the tuyere, which transfers a significant amount of momentum (and kinetic energy) to the bath stirring [198].

The ratio between the kinetic energy input rate of the gas injected through a tuyere and the buoyancy work rate done by the tuyere gas is [163]:

$$E^* = \frac{\rho_{gas}.Q_{tuyere}.(\frac{1}{2}).(V_{tuyere})^2}{(\rho_{bath} - \rho_{gas}).g.Q_{tuyere}.H_{bath}} \approx \frac{\rho_{gas}}{\rho_{bath}}.\frac{(V_{tuyere})^2}{2.g.H_{bath}} \tag{4.21}$$

$$E^* = \frac{8}{\pi^2}.\frac{\rho_{gas}}{\rho_{bath}}.\frac{(Q_{tuyere})^2}{(D_{tuyere})^4.g.H_{bath}} \tag{4.22}$$

Where, V_{tuyere} – gas velocity at the tuyere exit $(m.s^{-1})$, Q_{tuyere} – gas flow rate of a

single tuyere ($m^3.s^{-1}$), and D_{tuyere} – tuyere exit diameter (m).

When $E^* \ll 1$ for the industrial BOF, it is necessary to ensure that $E^* \ll 1$ for the physical model, but different exit tuyere diameter could be used (e.g. a geometrically similar exit diameter). In this case, the gas flow rate can be considered relatively low, and the tuyere exit diameter does not affect the fluid flow significantly in the BOF as occurs also in the ladle metallurgy [202].

Otherwise, e.g. if $E^* > 0.1$, the tuyere exit diameter of the physical model should be chosen so that the dimensionless number E^* is equal in the physical model and industrial BOF. This may occur for "strong" bottom-stirring processes (e.g. TBM) and bottom-only blowing processes (e.g. Q-POP) [11]. Therefore, the parameter E^* has practical relevance for the steelmaking converters' dimensional analysis.

Note that the use of a geometrically similar tuyere exit diameter in the physical model only satisfies the two similarity criteria for bottom stirring if the density ratio $\frac{\rho_{gas}}{\rho_{bath}}$ is equal in the physical model and the industrial BOF. It is also noteworthy that in calculating the gas flow rates, the average bath temperature and pressure should be considered [163].

Table 4.5 exhibits the summary of the dimensionless numbers used to perform the similarity study regarding this project.

Table 4.5: Summary of the dimensionless numbers applied to perform the similarity.

Equation	Dimensionless Number	Symbol	Industrial	Cold Model
4.5	Mach	Ma	2.39	1.91
4.10	Froude Biphasic	Fr^*_{LaSiP}	0.129	0.129
4.10	Froude Triphasic	Fr^*_{LaSiP}	0.097	0.069
4.11	Eotvos	Eo^*_{LaSiP}	$1.583x10^5$	$1.589x10^4$
4.13	Weber Biphasic	We^*_{LaSiP}	38.61	3.70
4.13	Weber Triphasic	We^*_{LaSiP}	30.62	2.20
4.20	Gas flow rate*	Q^*	0.995	0.705
4.22	Mixing energy*	E^*	0.0636	0.0034
2.27	Reynolds	$Re^*_{Meidani}$	$8.52x10^5$	$8.28x10^4$

Reynolds number, Equation 2.27, was adopted to assure the similarity of turbulent fluid flow. This equation reflects only the single-phase melt. The different Reynolds between the cold model and the industry are related to the considerable difference between the density of the water and steel. The cold model speed is also limited to the little pressure of the air compressor. This was not a problem since both values calculated are turbulent.

The modified Froude number, Fr^*_{LaSiP}, was used to assure the dynamic similarity. The distance between the lance tip and the quiescent bath (BLD) was adopted as a tuning

parameter to keep the same Froude number, and this was the reason for the different Bath Level Distance scale available in Table 4.2.

4.2 Laboratory Developments

All the laboratory experiments were carried out at LaSiP (Process Simulation Laboratory) in the dependencies of UFMG (Universidade Federal de Minas Gerais) in Brazil.

4.2.1 BOF Cold Model Equipment Details

As already mentioned in Section 4.1, another BOF cold model was available before this project started. New plexiglass and individual bottom stirring flowmeters were ordered to perform the current experiments. Figure 4.4 introduces the experimental set-up used to execute the experiments.

The individual gas flow rate control of each bottom stirring element was mandatory to perform the laboratory investigations similar to the industrial plant. Therefore, twelve new flowmeters were included in the new project.

1 – Plexiglass cold model
2 – Supersonic jet lance
3 – Tuyeres
4 – Tuyeres flow rate control
6 – Flow rate analogic sensor
8 – Pressure vessel
9 – Air compressor - Screw
10 – Air compressor – Piston
5, 7 , 11 – Manual valve
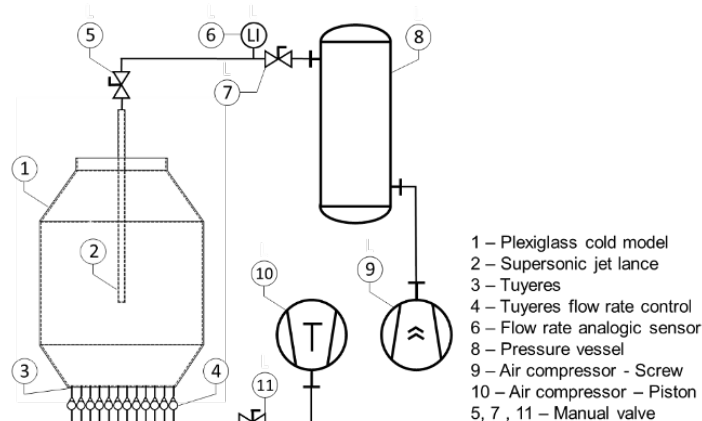
Figure 4.4: Experimental aparatus layout.

Figure 4.5 introduces the BOF Plexiglas model, built with the design that emerged from the similarity study performed in Session 4.1.

4.2.2 Measurement Methodologies developed at LaSiP

This section describes the measurement methodologies developed at LaSiP (Process Simulation Laboratory) to perform the proposed cold simulation trials, as already introduced in Section 4.1, different system conditions and goals have required specific approaches for measurement. Table 4.6 summarises the methodologies developed to measure the mixing time, mass transfer rate, jet penetration, decarburisation area, slopping, and projection rate over different blowing conditions. Trials included the biphasic air-water
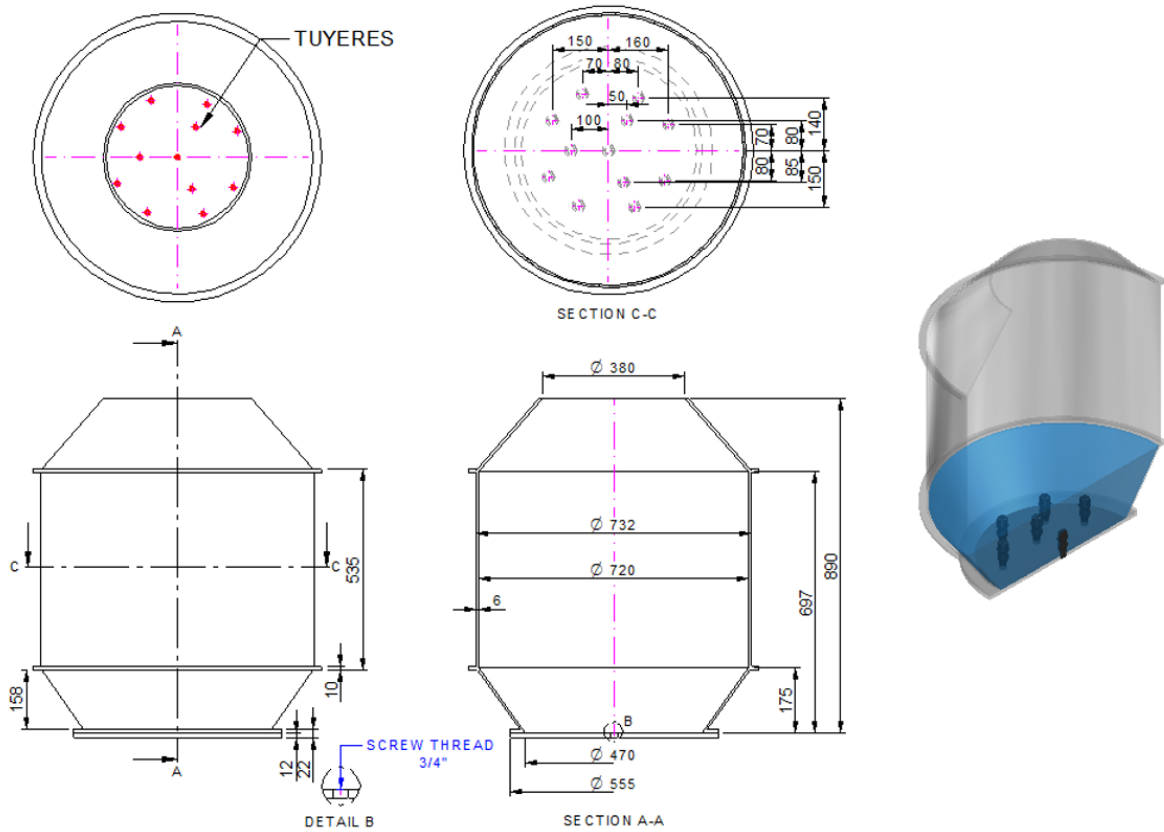
Figure 4.5: BOF Plexiglass model similar to Ternium Brazil's 330 t converter developed at LaSiP.

(AW) bath and the triphasic air-water-oil (AWO) system, as well as bottom stirring (B), top blowing (T), and combined bottom stirring and top blowing (TB).

Table 4.6: Summary of Laboratory measurement methodologies developed to perform the trials.

| Focus | Technique | Section | Bath Phase | | Tracer/ | Blowing | | | Year | Ref. |
			AW	AWO	Exchange Mat.	T	TB	B		
Mixing Time	Colorimetry	4.2.2.1	•		$KMnO_4$ liquid	•		•	2017	[203, 204]
	Conduct.	4.2.2.3	•		KCl liquid		•	•	2019	NA
			•		$KMnO_4$ liquid			•	2019	NA
	Luxmeter	4.2.2.2	•		$KMnO_4$ solid	•	•	•	2019	NA
				•	-			•	2019	[205]
Mass Transfer	Desorption	4.2.2.4	•		CO_2		•	•	2017	[203]
	Titration	4.2.2.5		•	Benzoic Acid		•	•	2018	[206]
Decarb. Area	Filming	4.2.2.6	•	•	-	•	•		2017	[203, 204]

4.2.2.1 Mixing Time – Colorimetry

Colourimetry trials were performed to check the top blowing and bottom stirring pattern influence, and different approaches for each condition were considered. Figure 4.6 introduces the schematic setup and the tracer injection point. To execute the experiments the plexiglass reactor was filled with water, 0.049 m^3, to simulate molten steel and a small volume, $4x10^{-5}$ m^3, of aqueous potassium permanganate ($KMnO_4$) solution,

316 $mol.m^{-3}$, was added as tracer because of its distinct water colour.
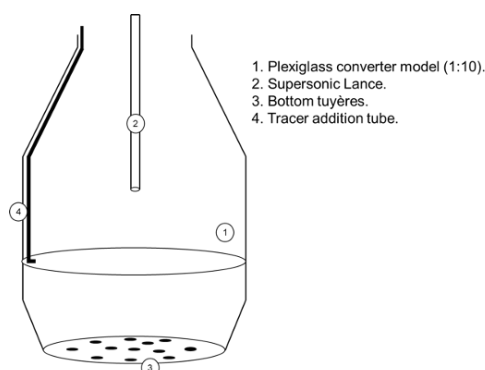
Figure 4.6: Schematic setup to determine the mixing time through the colorimetric method.

To carry out the top blowing trials; a 90° angle separated two light reflectors positioned behind the vessel, and a high definition digital camera was positioned in front to make a video record for further analysis. Similarly, to perform the bottom stirring trials, the light reflectors were positioned in the same way, and a GoPro® camera was fixed at the top and inside the reactor to record the images.

A typical bath mixing analysis through the colourimetry method is shown in Figure 4.7 for the top blowing trials. This image compares two top blowing patterns, the green one with a lower mixing time and the red one with higher mixing time.
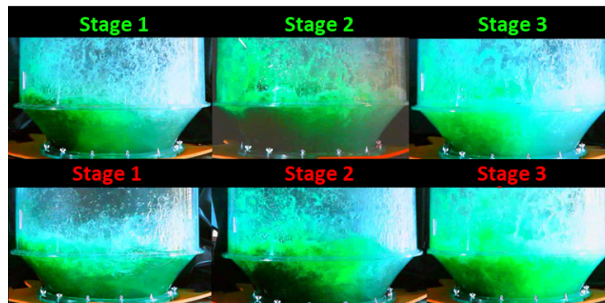
Figure 4.7: Mixing time determination for top blowing experiments through the colorimetric method.

Figure 4.8 shows a typical image of the colourimetric method for the bottom stirring analysis, and detail of tracer addition start until bath homogenisation.

Figure 4.8: Mixing time determination for bottom stirring experiments through the colorimetric method.

A video editing software (Sony VegasPro®) was applied to split the video into short time intervals for accurate analysis and reduce the brightness and promote an easier visualisation of the dead zones. Figure 4.9 shows the differences between the images with and without the contrast filter.

Figure 4.9: Image comparison before and after the video editing.

Through the video recorded during the experiments and after video editing, the mixing times were visually determined by three observers, considering the time interval between the tracer addition until the bath reached a uniform colouration.

4.2.2.2 Mixing Time – Luxmeter

As previously discussed, the colourimetry method was based on the visual inspection of three different observers. To reduce the deviation in the simulation results, the development of a new method was fundamental to increase the results' confidence. The luxmeter method is a novel low-cost technique developed at LaSiP [205] and inspired by the experiments proposed by Wuppermann et al. [168]. This technique employs the difference of light captured by a sensor to determine the mixing time in physical cold models.

The luxmeter, or light meter, is a commercial device used to measure the amount of light and is widely used to determine the proper exposure. It is composed of an amperemeter connected to a photoelectric cell that generates an electric current when the light passes through it. A difference of current is generated and converted to lux by the sensor.

A dark tracer is inserted in the aqueous phase to start a new experiment. After a particular period of time, the bath homogenises and becomes completely dark. The luxmeter measures the light difference during the whole simulation, and the period between tracer injection and bath homogenisation determines the mixing time. Two-phase and three-phase experiments employed the luxmeter method.

The reactor was filled with water ($0.049 \ m^3$), to execute the three-phase tests, and dyed soy oil ($0.009 \ m^3$) was mixed with blue aniline, to simulate the molten steel the slag phase, respectively.

A LED spotlight ($50 \ W$) was installed behind the model to homogenise the light. Two digital luxmeters (Tl-600 supplied by HLL) were fixed on the opposite side of the

spotlight in the cold model external wall, Figure 4.10, and a high definition digital camera was positioned in front to make a video record for further analysis.

Initially, when the bottom stirring flow was activated, a decrease in the luxmeter values was observed. Data recording and top blowing only started after stabilisation of the luxmeter values. The position of the luxmeter sensor was crucial for the experiment. It should be positioned parallel to the light source at the bottom of the vessel to capture the luminosity difference in the bath's deepest regions.
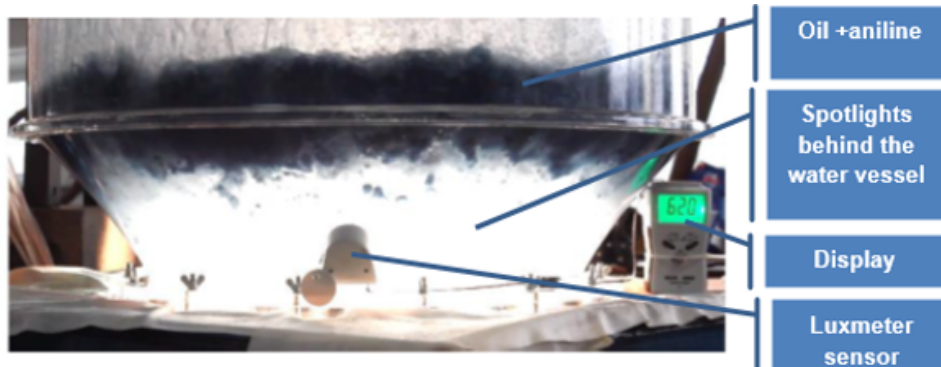
Figure 4.10: Schematic setup to determine the mixing time through the luxmeter method [205].

Potassium permanganate ($KMnO_4$) tracer in the liquid and solid-state was employed to perform the biphasic tests. Other tracers, such as food colouring, were tested, but potassium permanganate was chosen due to its staining intensity. The dispersion of a liquid tracer in a system with strong turbulence is fast. To retard tracer dispersion, $KMnO_4$ in the solid-state was employed to facilitate the identification of the dead flow zones in the bath. The solid-state tracer developed was an ice cube of potassium permanganate supersaturated solution with a concentration of 63.28 $mol.m^{-3}$, above the potassium permanganate solubility in water.

The equipment setup was according to the three-phase experiments. The bottom stirring and the supersonic top lance were activated. After the luxmeter stabilisation, the solid-state tracer was added through the top of the cold model, and the data acquisition started.

The mixing time was defined based on the non-dimensional light intensity ($L*$), calculated according to Equation 4.23, which is plotted as a function of time [205].

$$L^* = \frac{L_i - L}{L_i - L_f} \tag{4.23}$$

Where, L^* – dimensionless light intensity ($-$), L_i – initial light intensity ($cd.m^{-2}$), L – instantaneous light intensity ($cd.m^{-2}$), and L_f – light intensity at the end of the test ($cd.m^{-2}$).

Initially, for the tests employing liquid tracer, a calibration curve was built to correlate the luminosity and tracer concentration. The conductivity meter method was employed

to evaluate the luxmeter technique accuracy and build the mentioned calibration curve because of its extensive previous literature availability.

The initial proposal was to perform tests using the two techniques to obtain calibration curves that would make the comparison plausible. As the addition of tracer occurs, it is possible to build the bath concentration variation curves. The tracer used for the lux meter method was the potassium permanganate and was injected gradually $2x10^{-4}$ kg of $KMnO_4$ until the final mass added in the bath was 0.002 kg. At each addition, the lux variation could be observed according to the mass of the tracer added.

For the conductivity meter method, a calibration curve was built to relate electric conductivity with tracer concentration, Figure 4.11. Bench-scale tests were performed using a 1 L beaker, and masses of $2.5x10^{-5}$ kg of potassium chloride (KCl) were added until the final mass of $22.5x10^{-5}$ kg was obtained. The conductivity values were recorded according to the addition of salt and homogenisation in the vessel. Finally, a curve was plotted for each technique, lux meter, and conductivity meter, according to Figure 4.9
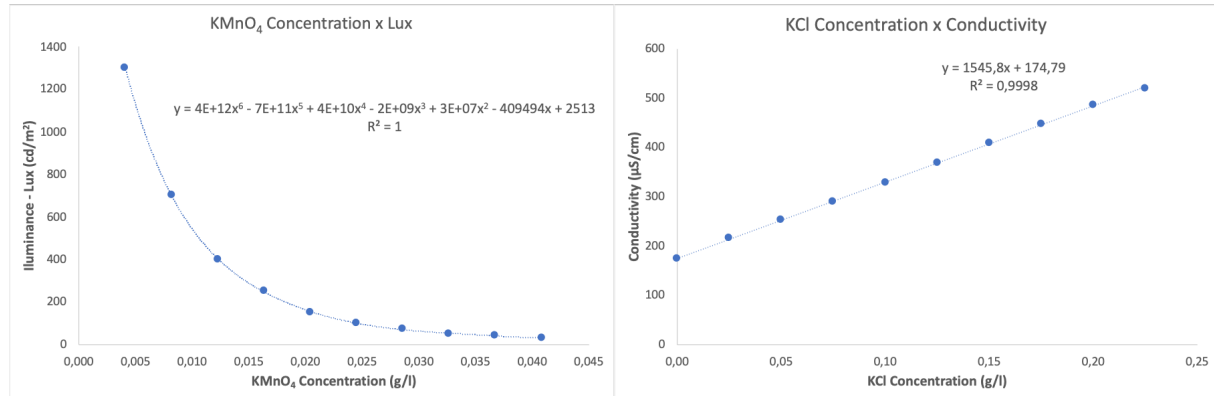
Figure 4.11: Calibration curves for the luxmeter, and conductivity meter method.

The calibration curve obtained was a sixth-degree polynomial regression, and the concentration was used to obtain the dimensionless concentration (C^*), Equation 4.24 [205].

$$C^* = \frac{C - C_i}{C_f - C_i} \qquad (4.24)$$

Where, C^* – dimensionless concentration $(-)$, C_i – initial tracer concentration $(mol.m^{-3})$, C – instantaneous tracer concentration $(mol.m^{-3})$, and C_f – final tracer concentration $(mol.m^{-3})$.

The different tests performed for mixing time determination using the luxmeter technique were summarised in the Table 4.7.

Using the dimensionless concentration, Equation 4.24, a graph of (C^*) as a function of time was plotted, Figure 4.12. Two horizontal lines were observed to indicate the interval of deviation as $\pm5\%$. The mixing time was determined when the (C^*) remained stable inside the accepted deviation interval.

Table 4.7: Different tests performed using the luxmeter technique.

System	Tracer	Blowing Condition
Air-Water	$KMnO_4$ liquid solution	Bottom stirring.
Air-Water	$KMnO_4$ solid solution	Top blowing and combined bottom stirring and top blowing.
Air-Water-oil	Dyed soy oil	Combined bottom stirring and top blowing.
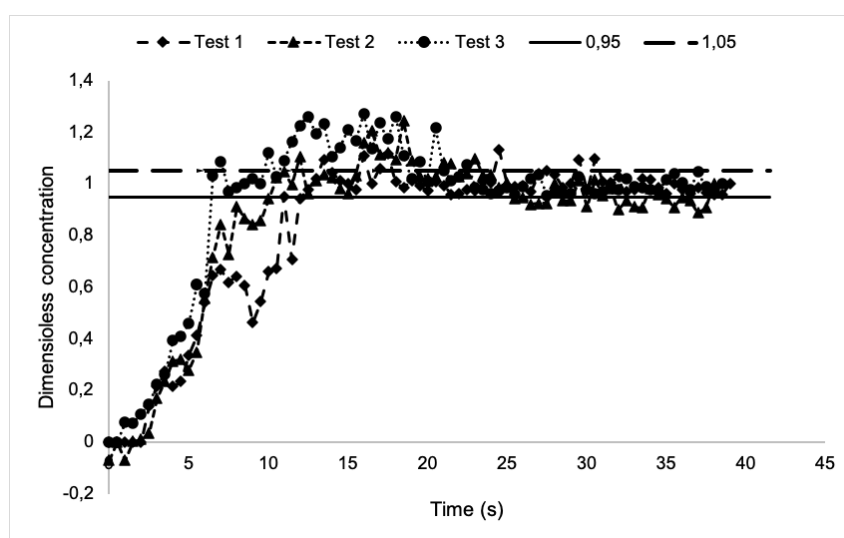
Figure 4.12: Typical curve for mixing time determination through the luxmeter method.

Tests were performed in triplicate for each bottom stirring configuration, and the mixing time was considered the average value obtained in the graph. In the first stage, there was a significant decrease in the lux; in the second stage, it was possible to observe that there was still a decrease of the lux, but the sensor was not capable of measuring the lux difference due to its sensitivity.

4.2.2.3 Mixing Time – Conductivity Meter

The conductivity meter is the most popular method for the mixing time's studies in cold modelling, KCl and $NaCl$ are the most common tracers employed within this technique. KCl was the tracer chosen for this research because it is easy to manage, and the solution can be discharged in a sewage system without previous treatment. Two probes were utilised in two different positions, one diametrically opposite the tracer injection point, and the second was placed perpendicular to the first, as shown in Figure 4.13.

Initially, a calibration curve was built to relate the electric conductivity meter with the tracer concentration. The tests were performed on a bench scale, and $2.5x10^{-5}$ kg of potassium chloride was added to a one-litre beaker until the final mass added reached $22.5x10^{-5}$ kg, the conductivity probe measured the electrical conductivity meter. The obtained linear regression defined the calibration curve.
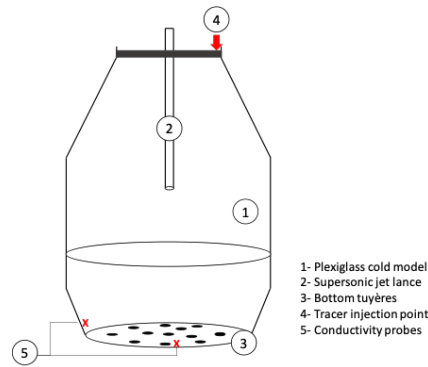
Figure 4.13: Schematic setup to determine the mixing time through the conductivity meter method.

The tests were performed by inserting $2x10^{-5}$ m^3 of the tracer with a concentration of 3.35 $mol.m^{-3}$ of KCl. Injection speed was standard, and location determined and kept constant in all tests. The experiments were carried out in the following order: initially adjusted the bottom gas flow rate according to the configuration to be tested, then 0.049 m^3 of water were added to the vessel, and the bath ceased for 5 minutes to eliminate residual speeds. Following the tests, the gas flow rate was initiated, and the data registered. This methodology was used to perform bottom stirring and the combined top blowing and bottom stirring trials for the biphasic bath system.

The concentrations were determined from the regression made with the calibration curve, and graphs were obtained as a function of dimensionless concentration (C^*) and time, two horizontal lines were plotted to indicate the interval of variation as ±5%. The mixing time was determined when the dimensionless concentration (C^*) remained stable inside the variation interval. Figure 4.14 shows the typical curve using the conductivity meter to measure mixing time.
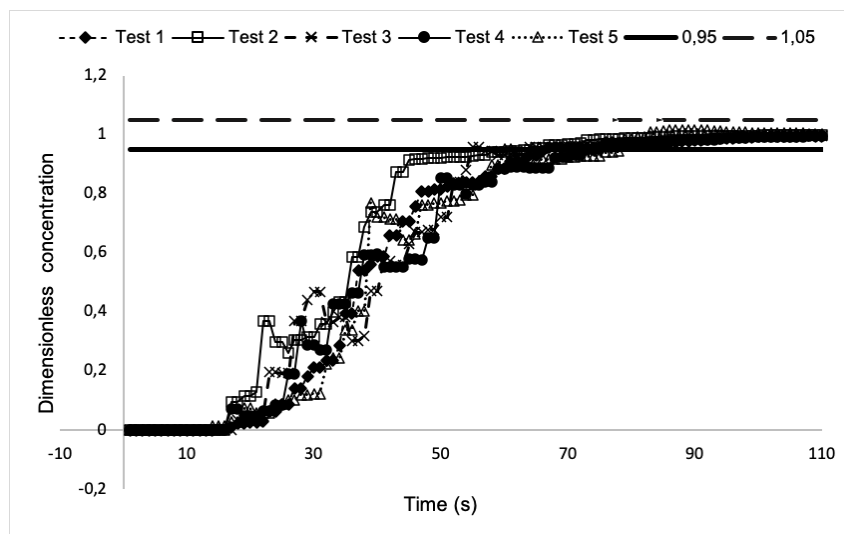
Figure 4.14: Typical curve for mixing time determination through the conductivity meter method.

The mixing time obtained in each probe showed different values, and the longest time

was considered. Seven trials were performed for each configuration, and only the data of the five tests in which the mixing time had lower dispersion from the average time were considered for the analysis.

4.2.2.4 Mass Transfer Rate – CO_2 Desorption

In the last part of the blow, mass diffusion phenomena influenced the oxygen distribution among all elements when the carbon content dropped below a critical value. In this phase, a first-order equation was considered to control the carbon mass transfer.

The CO_2 desorption method was proposed to evaluate this last blowing phase in the BOF cold modelling. As already mentioned in Section 2.4.4.2, the system principles work with a known concentration of sodium hydroxide ($NaOH$) solution that provides the initial pH of the cold model's bath. A small amount of phenolphthalein, an acid-base indicator that changes its colour according to the system's pH to support visualisation of the bath turning point, was also employed. As the $NaOH$ solution is basic, the bath initially presented a pink colour. The experiment acid/basic reactions are described according to Equation 4.25 and 4.26,

$$CO_2(g) + H_2O(l) \Rightarrow H_2CO_3(aq) \tag{4.25}$$

$$2.NaOH(aq) + H_2CO_3(aq) \Rightarrow Na_2CO_3(s) + 2.H_2O(l) \tag{4.26}$$
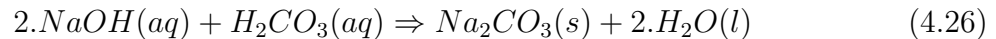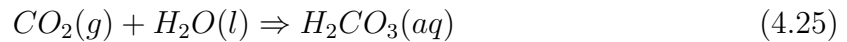
The carbon dioxide injection reacts with the water in the solution until it becomes colourless, demonstrating that the pH decreased. The reached pH was about 6.5, and a sample was taken for measurement. When the aimed value was achieved, the cold model combined bottom stirring, and top lance blow starts, resulting in CO_2 desorption generating in pH value increment.

The CO_2 concentration in solution reached equilibrium when no significant pH variations were observed, and the test was ended, experiments were performed in triplicates, and during the tests, pH variation was recorded by a pH-meter with a pre-determinate time interval until it reached the equilibrium.

To carry out a kinetic study through the recorded pH values, a mathematical approach to convert pH into CO_2 concentration values was necessary. Tavares [207] proposes a calibration curve to convert pH to CO_2 concentration, according to the Equations 4.27 and 4.28.

$$A = \frac{pH}{5} \tag{4.27}$$

Since A is a conversion constant, this value is then used to obtain a CO_2 concentration. The best fit was achieved by linearisation approximating a power equation obtaining the

values of CO_2 concentration as a function of pH, Equation 4.28.

$$C_{CO_2} = 37294.A^{-14.234} \qquad (4.28)$$

The initial concentration ($C_{CO_2}^i$) at a specific time ($C_{CO_2}^t$) and equilibrium concentration ($C_{CO_2}^{eq}$) was obtained at the end of the experiment, when significant variations were no longer observed, were used to draw the calibration curve, through the relation shown in Equation 4.29. There was no preference for the equation units because the result was presented as a dimensionless coefficient.

$$-ln\left[\frac{C_{CO_2}^t - C_{CO_2}^{eq}}{C_{CO_2}^i - C_{CO_2}^{eq}}\right] = K_{tm}.t = G \qquad (4.29)$$

Based on this equation, it was possible to plot a linear curve, and through the curve regression, determine the value of mass transfer coefficient (K_{tm}), denoted as the axis slope.

4.2.2.5 Mass Transfer Rate – Benzoic Acid Titration

Triphasic tests were performed to simulate the metal/slag blowing interaction based on the solvent extraction process, and the experiments were performed with an aqueous solution in contact with the soybean oil, an organic phase. The aqueous phase was enriched with known benzoic acid concentration, and, according to the organic phase transfer phenomenon over time, the concentration difference was monitored. According to the dynamic similarity, the aqueous solution and the soybean oil represented the steel and slag.

Initially, it was considered to adopt paraffin oil to run the tests. However, it presented a very slow mass transfer and disposal problems, which led to the choice of soybean oil, easier to purchase and recycle. Another attempt was to measure the pH variation in the bath using a $pH - meter$ and build a calibration curve from the acid concentration shift. This option was not feasible because the samples taken from the aqueous phase had a considerable amount of oil, which limited the $pH - meter$ measurement since the ions could not pass through the membrane.

The methodology chosen employed aqueous solution samples collected at uniform time intervals using a peristaltic pump and a stainless-steel pipe in the same sampling position, as shown in Figure 4.15. The samples were taken from the beginning until the end of the bottom stirring tests that lasted about 20 minutes. Instantaneous acid samples concentration was determined by titration with sodium hydroxide solution ($C_{NaOH} = 24.7\ mol.m^{-3}$).

The values of concentration and partition obtained in bench tests were applied, and the mass transfer coefficient was determined through the modified Equation 4.30, proposed
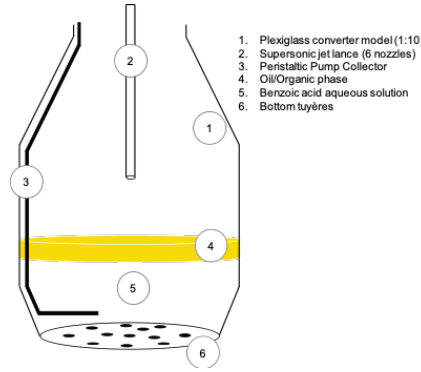
Figure 4.15: Schematic setup to determine the mass transfer rate through the benzoic acid titration method.

by Kim and Fruehan [208].

$$\frac{ln\left[\left(1 - \frac{h.V_W}{V_O}\right).\frac{C_W}{C_W^O} - \frac{h.V_W}{V_O}\right]}{1 + \frac{h.V_W}{V_O}} = \frac{K_w.A}{V_W}.t \tag{4.30}$$

Where, C_W^O – initial aqueous solution concentration ($mol.m^{-3}$), C_W – instant aqueous solution concentration ($mol.m^{-3}$), k_W – mass transfer coefficient ($m.s^{-1}$), V_W – aqueous phase volume (m^3), V_O – organic phase volume (m^3), $h = \frac{C_W'}{C_O}$ – partition ratio ($-$), C_W' – concentration at the water interface ($mol.m^{-3}$), C_O – organic phase concentration ($mol.m^{-3}$), and t – elapsed time (s).

4.2.2.6 Others – Jet Penetration, Decarburization Area

In previous experiments regarding jet penetration, researchers employed the image analysis technique to measure cavity depth and shape, through scales or squared reference by the side or behind the cold modelling [75, 190, 105]. To increase the results' reliability, some authors used equations from mathematical models to calculate the estimated value for depth and shape [75, 181].

On the other hand, the methodology developed at LaSiP has a different approach to measure cavity depth and shape. It was based on the scale between the cold model size and the equivalent number of pixels in the images, making the results more reliable and the analysis easier. Previous researchers have developed at LaSiP new jet penetration mathematical description based on this experiment, previously mentioned in Section 2.2.2.

This novel technique to define these parameters is a significant improvement compared to previous works. The methodology setup is the same, Figure 4.16, but the measurement technology itself is more precise and uses image software to determine the jet penetration and decarburisation area.

To carry out the experiments; a 90° angle separated two light reflectors positioned behind the vessel, and a high definition digital camera was positioned in front to make a video recording for further analysis.
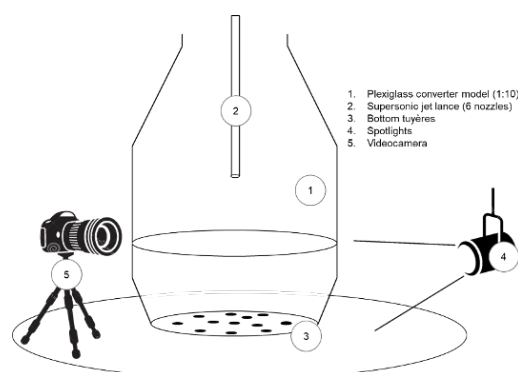
Figure 4.16: Schematic setup to determine jet penetration and decarburization area.

The trial recorded images were uploaded to the software ImageJ®, very useful for image treatment and scale measurements, based on the pixel rate. That is why it was necessary to use the same computer screen and have the same resolution when treating it. In these tests, the user sets the scale, based on the diameter of the model and use the software commands such as "line" and "handsfree" to measure the jet penetration and the decarburisation area, as shown in Figure 4.17. The static bath has a defined height, using this value as a range (pixels to centimeters), it was possible to define the penetration and the decarburisation area using the delimitation tool offered by ImageJ®, described before.
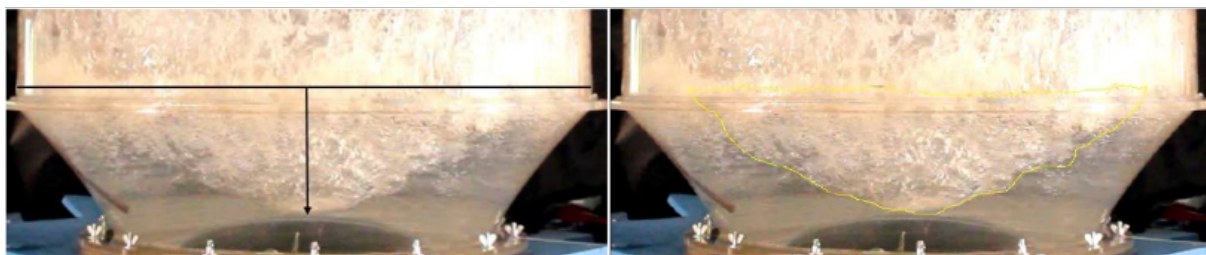
Figure 4.17: Typical jet penetration (left) and decarburization area (right) measurements.

Different measurements were necessary according to each blowing step because it is a static determination. Performing this measurement for each step of the blowing pattern, a complete jet-bath interaction description through the entire blowing process was viable.

4.3 Industrial BOF Operations - Ternium BR Steel Plant

The 5 *mtpy* (million ton per year) state-of-the-art steelmaking complex of Ternium Brazil, former thyssenkrupp CSA, located in Santa Cruz, Rio de Janeiro city, started up in 2010 from a greenfield, Figure 4.18. The Steelmaking Plant includes two plants of Hot Metal Desulfurization ($2xHMD$) and two Basic Oxygen Furnace ($2xBOF$) converters in the Primary Metallurgy. The Secondary Metallurgy is composed by two Ladle Treatment Stirring ($2xLTS$), two vacuum degassers ($2xRH$) and one Aluminum Heating Facility ($1xAHF$), and finally two Continuous Casting Machines ($2xCCM$). Despite the nominal

heat-size of 330 t of liquid steel tapped per heat ($t/heat$), the current heat size average is 340 $t/heat$.

The modern BOF supplied by Primetals Technologies was designed considering up-to-date technology. The available technologies related to the processes are sublance, automated off-gas system, pneumatic slag stoppers, slag detection system for tapping, and the TBM bottom stirring technology. TBM is the commercial name of Thyssen Blowing Metallurgy. The dry-type primary dedusting cleaning system, designed to clean and recover the gas, was the first in operation in Latin America. The converter off-gas heat also generates steam in a boiler plant.

Figure 4.18: Ternium Brazil, Rio de Janeiro, 5 $mtpy$ state-of-the-art steelmaking complex.

4.3.1 Automation and Control Systems

The BOF is fully automated and highly integrated; all the systems and equipment are controlled through the basic automation system (Level 1) and the Steel Expert Process Models® (Level 2), Figure 4.19. Due to the high automation and variables control, the process engineer has a wide range of process optimisation actions. An excellent example is the individual gas flow control for each bottom stirring element, the objective of this thesis.

The Level 2 optimisation system is responsible for high reproducibility between the heats blown. The available online models run all the time, monitoring the metallurgical
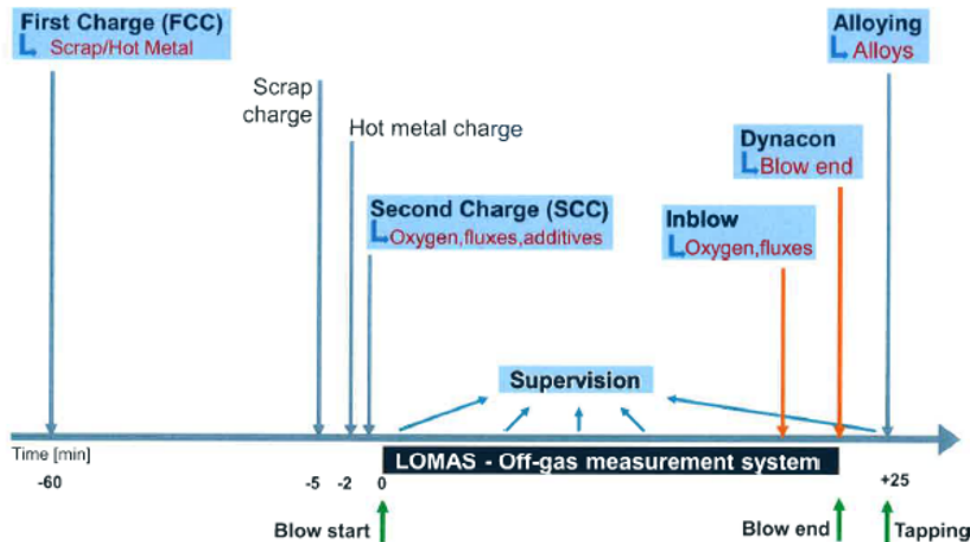
Figure 4.19: Steel expert process models®, Level 2. Source: Primetals documentation.

process. Model calculations are adjusted according to all raw material additions while blowing and available measurements, such as sublance and off-gas information.

The sublance technology allows the measurement of temperature, oxygen activity, carbon, and melt sampling without the oxygen blowing interruption (in-blow measurement) as well as after the end of the blow (end-blow measurements). The in-blow measurements are used for the dynamic model to adjust the parameters to determine the ideal end-blow point.

The automated off-gas system (LOMAS technology) measures and analyses the off-gas during the oxygen blowing process. The mass spectrometer measures the relevant off-gas composition precisely, and this information is fundamental for the Dynacon model to precisely adjust the end-blow point.

All these technologies standardise the BOF production operations, reduce human interference, and improve the end-of-blow hitting rate for steel carbon content and bath temperature, fundamental parameters to measure the performance of this thesis proposal.

4.3.2 Oxygen Top Blowing Description

The top oxygen blowing lance is automated, and the blowing patterns are defined inside the Level 2 system, which contains the setup for oxygen flow rate and Bath Level Distance (BLD), according to each blow phase, and metallurgical needs. The top oxygen lance design ranges between 900 and $1,200$ $Nm^3.min^{-1}$, back pressure in the blowing phase ranges between 11 and 14.5 bar. Bath Level Distance (BLD) ranges between 3.4 to 2.2 m. Usually, the oxygen lance blow in the slag phase formation starts with 3.4 m and remains 2.2 m in the main decarburisation phase until the end of the oxygen blow. Figure 4.20 shows a typical time for each blowing phase.
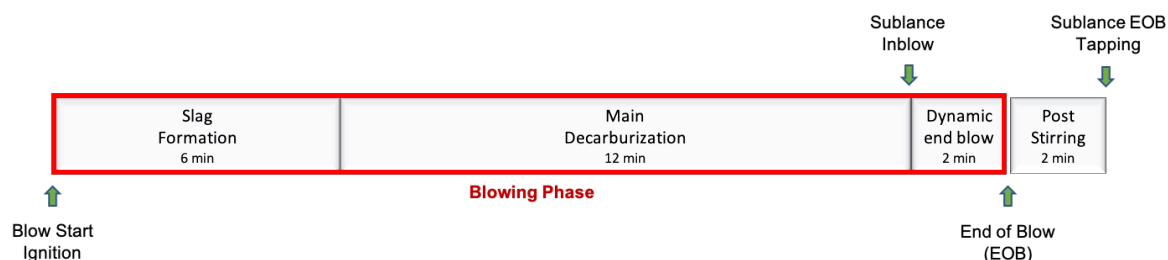
Figure 4.20: Schematic phases of the BOF oxygen blowing and post stirring.

4.3.3 Bottom Stirring Description

At Ternium Brazil, the available bottom stirring technology is the Thyssen Blowing Metallurgy (TBM), which adopts the Single Hole Plug (SHP) as a purging element. There are twelve available bottom stirring elements, displaced in one central plug (12) and two outer circles, the inner circle has three plugs (9, 10 and 11), and the external one has eight plugs (1, 2, 3, 4, 5, 6, 7 and 8), Figure 4.21.

The equipment fundamentally contains a valve station inside a modular container and a rotary joint in the trunnion axis. Argon and Nitrogen are available as the inert gas, and the buffer pressure is 17 and 16 bar, respectively. Individual gas pressure and flow control are available to offer high operational flexibility; the advanced instrumentation and automation maintain constant flow rates for each line, avoiding the bottom stirring element obstruction. The bottom stirring gas flow rate and the gas type (N_2 or Ar) set-points depend on the process phase and the metallurgical aims. Each bottom stirring element flow rate ranges between 0.5 and 1.2 $Nm^3.min^{-1}$, to avoid clogging the bottom stirring element with sticky slag, the minimum flow rate value is defined. In the blowing phase, each bottom stirring element's measured pressure depends on the flow rate, and the condition of obstruction of each one, maximum pressure is around 17 bar.
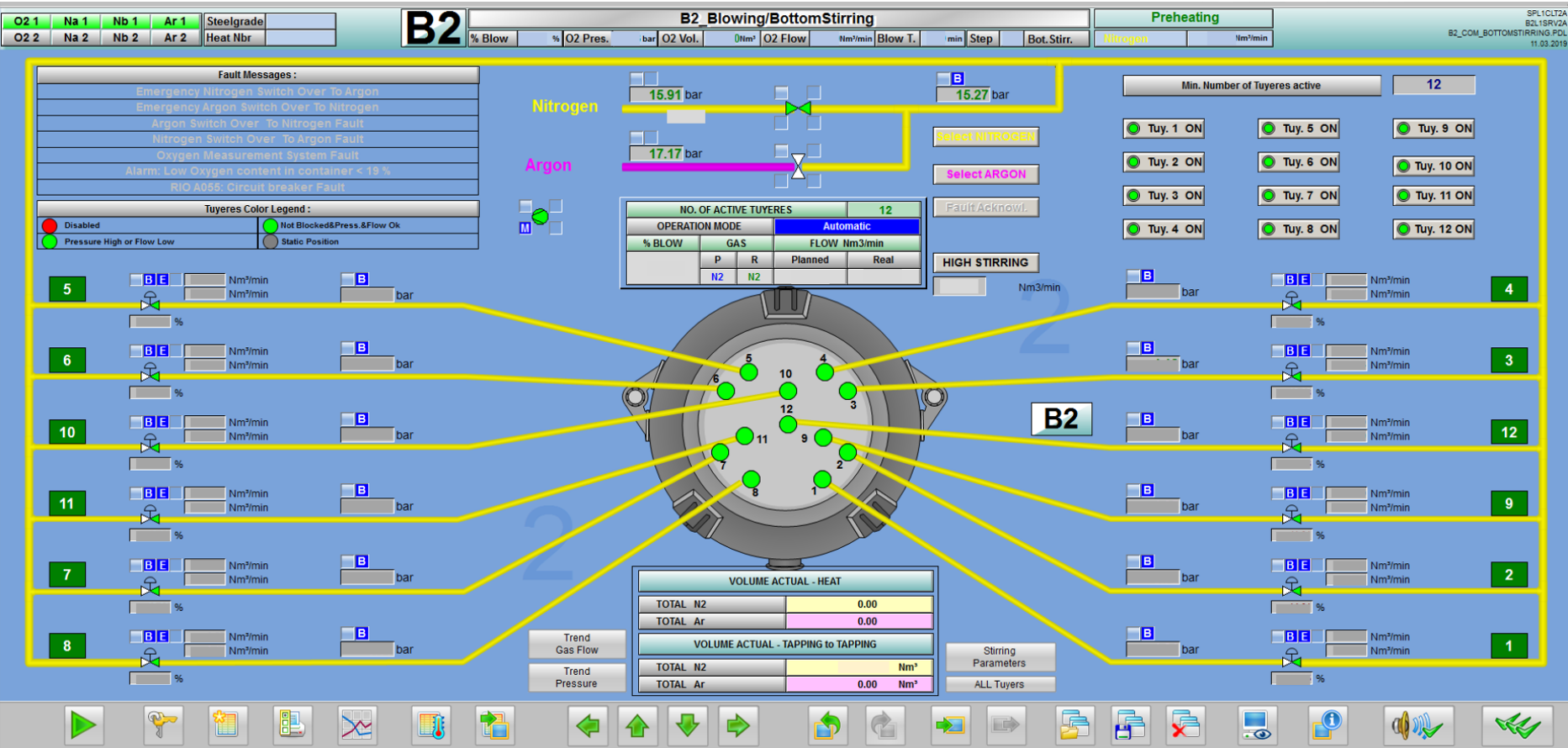
Figure 4.21: Bottom stirring HMI - Ternium Brazil Plant.

5 Results and Discussions

This section describes the performed experiments and is organized between the results and discussions related to the cold model simulation trials performed at LaSiP, Section 5.1, and the industrial heats blown at the BOF of Ternium BR, Section 5.2.

5.1 Laboratory Trials

Three different phases divided the laboratory experiments and considered specific blowing conditions, methodology, and goals, such as mixing time, mass transfer rate, jet penetration, decarburization area, slopping, and projection rate over different system conditions, Table 5.11.

Table 5.1: Summary of performed BOF cold simulations.

#	Blowing	System		Focus				Measurements						Section
		AW	AWO	MT	MTR	DA	JP	CL	CN	LX	DS	TT	IA	
Phase 1	T	•		•	•	•	•	•			•		•	
	B	•		•	•			•			•		•	5.1.1
	TB	•		•	•	•	•	•			•		•	
Phase 2	T													
	B		•		•						•	•		5.1.2
	TB													
Phase 3	T													
	B	•	•	•					•	•			•	5.1.3
	TB	•	•	•					•	•			•	

Blowing	T → Top Blowing, B → Bottom Stirring, TB → Top Blowing + Bottom Stirring.
System	AW → Air-Water, AWO → Air-Water-Oil.
Focus	MT → Mixing Time, MTR → Mass Transfer Rate, DA → Decarburization Area, JP → Jet Penetration.
Measurements	CL → Colorimetry, CN → conductivity meter, LX → Luxmeter, DS → Desorption, TT → Titration, IA → Image Analysis.

The first phase of the laboratory experiments, Section 5.1.1, focused on biphasic experiments to simulate the top blowing patterns and the different proposals for the bottom stirring gas flow rate and design. The performance was measured through the mixing time, mass transfer rate, jet penetration, and decarburization area employing different

techniques such as the colourimetric analysis, CO_2 desorption, and image analysis, respectively. Phase 2, Section 5.1.2, aimed to investigate the different patterns and configurations proposed for the BOF bottom stirring experiments performed in the tri-phasic system to investigate the steel-slag mass transfer, employing the benzoic acid titration, and image analysis technique. The third phase, Section 5.1.3, aimed to investigate the mixing time through experiments correlating the top lance blowing patterns with the different bottom stirring setups proposed in Phase 2. The luxmeter and the conductivity meter measurement techniques were employed in a biphasic and triphasic system, and to find relevant results, adaptations were proposed to improve the system visualization, and the conductivity meter method introduced to validate the luxmeter method results.

5.1.1 Phase 1

The tests simulated the BOF blowing patterns employed at Ternium BR, the main focus was on the main decarburization phase and the end of the blowing phase, just after the critical carbon, as shown in Table 5.2. The modified Froude number Fr^*_{LaSiP}, proposed in Section 4.1, was used to establish the laboratory blowing pattern through the conversion of the industrial blowing pattern.

Table 5.2: Standard blowing pattern simulated [30].

Blowing stage	DBL Ternium BR (m)	DBL LaSiP (m)	Flowrate Ternium BR (Nm³/minute)	Flowrate LaSiP (Nm³/minute)	Flowrate TBM Ternium BR (Nm³/minute)	Flowrate TBM LaSiP (NL/minute)
Decarburization	2.3	0.400	900	120	14	60
End of blow	2.2	0.451	1,200	160	14	60

It is important to note, as opposed to the industrial practice, the lance rises in the final blow stage in the laboratory experiments, and the lance parameters to meet the similar Fr^*_{LaSiP} dimensionless number ratio explains the difference, Equation 4.10, a compensation between the flow rate and the bath level distance (BLD or DBL) was necessary. Table 4.5 exhibits the summary of the dimensionless numbers used to perform the similarity study regarding this project.

5.1.1.1 Mixing Time - Colorimetric Analysis

The definition of mixing time is the interval between tracer addition until the time when the bath colour becomes uniform. Tables 5.3 and 5.4 introduce the results of mixing time for each blowing stage, flow rate, bath level distance (BLD), and the bottom stirring (TBM) configuration adopted, summing up the flow rate of the 12 stirring points. It is important to remark that the experiments were performed duplicated to validate the results obtained, and the mixing time exhibited below corresponds to the average values for each experiment and the respective arrangement.

Table 5.3: Mixing times for the main decarburization phase [30].

Test	Lance flowrate (Nm³/hour)	DBL (mm)	TBM flowrate (NL/minute) Ext, Int, Central	Mixing times (second)	Standard deviation
TerBR 3-14	120	400	Max, Off, Off (40)	18.25	2.63
TerBR 3-15	120	400	Off, Max, Max (20)	17.00	1.41
TerBR 3-16	120	400	Max, Max, Max (60)	17.75	1.71
TerBR 3-17	120	400	Var, Var, Var (42)	18.50	1.29

Mixing times for the final blow phase (160 Nm^3/h) were lower than the times reported in the decarburization stage (120 Nm^3/h). The observed results may be related to the lance flow rate's predominant effect on the mixture's progression compared to the BLD and the bottom stirring configuration and flow rate. Some similarities with different lance flow rates were observed when comparing the tests for the same bottom stirring configurations.

Table 5.4: Mixing times for the dynamic end blow phase [30].

Test	Lance flowrate (Nm³/hour)	DBL (mm)	TBM flowrate (NL/minute) Ext, Int, Central	Mixing times (second)	Standard deviation
TerBR 3-10	160	451	Off, Max, Max (20)	7.67	1.53
TerBR 3-11	160	451	Max, Max, Max (60)	16.75	1.26
TerBR 3-12	160	451	Max, Off, Off (40)	15.25	1.71
TerBR 3-13	160	451	Var, Var, Var (42)	14.75	1.26

The experiments $TerBR\ 3-10$ and $3-15$ (Off, Max, Max 20 Nl/min) exhibited the lowest mixing times for the end blow and main decarburization, respectively. The image analysis allows observing that the tracer, when injected, flows to the centre of the converter and then faces an influence of a barrier produced by the activated internal bottom stirring elements. However, due to the higher lance flow rate of $TerBR\ 3-10$ (160 Nm^3/h), the tracer spreads more vigorously than in the $TerBR\ 3-15$ (120 Nm^3/h), where the tracer tends to flow in the outer circle of the acrylic.

Figure 5.1 illustrates the behavior of the tracer for the combined top blowing and bottom stirring for two experiments with similar lance flow rates (160 Nm^3/h), $TerBR\ 3-10$ (20 Nl/min) and $3-11$ (60 Nl/min) at three different time steps ($25\%, 50\%\ and\ 75\%$). The $TerBR\ 3-10$ (20 Nl/min) is attractive for the process since, for 75% of the mixing time (T_{mix}), the tracer was substantially mixed. Moreover, the flow rate was lower than the other bottom stirring patterns, which means a reduced inert gas consumption and, consequently, less refractory wear, reducing the process's costs.

5.1.1.2 Jet Penetration and Decarburization Area

Tables 5.5 and 5.6 correlate the jet penetration and the decarburization area for each blowing pattern, describing the BLD and the bottom stirring configuration employed for
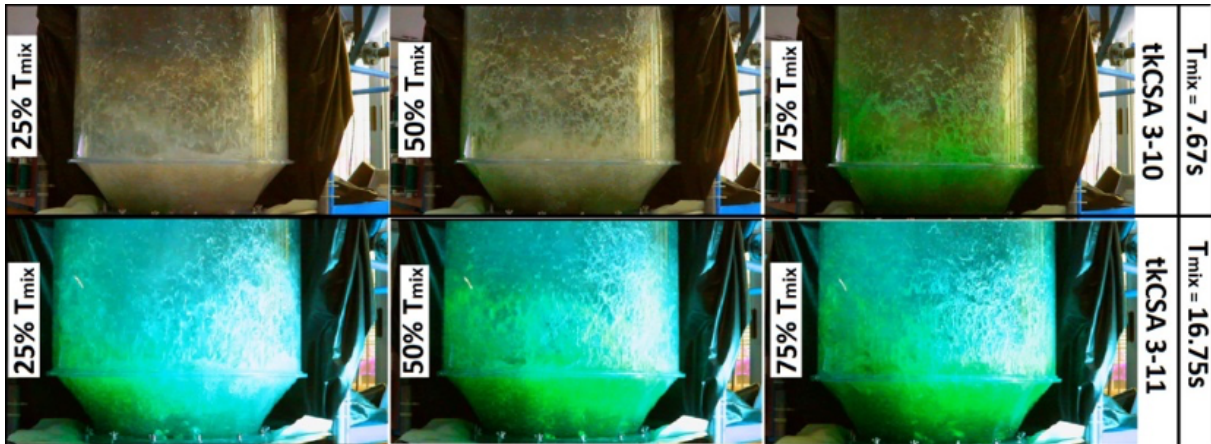
Figure 5.1: Tracer behavior comparison [30].

each experiment.

Table 5.5: Decarburization area and jet penetration for the main decarburization phase [30].

Test	LaSiP DBL (mm)	LaSiP flowrate (Nm³/hour)	Tuyeres configurations (NL/minute)	Decarburization area (%)	Jet penetration (mm)
TerBR 3-14	400	120	Max, Off, Off (40)	60.4	136.6
TerBR 3-15	400	120	Off, Max, Max (20)	60.4	140.6
TerBR 3-16	400	120	Max, Max, Max (60)	57.8	134.7
TerBR 3-17	400	120	Var, Var, Var (42)	61.3	139.3

Table 5.6: Decarburization area and jet penetration for the dynamic end of blow phase [30].

Test	LaSiP DBL (mm)	LaSiP flowrate (Nm³/hour)	Tuyeres configurations (NL/minute)	Decarburization area (%)	Jet penetration (mm)
TerBR 3-10	451	160	Off, Max, Max (20)	66.7	126.4
TerBR 3-11	451	160	Max, Max, Max (60)	69.8	133.1
TerBR 3-12	451	160	Max, Off, Off (40)	64.4	124.5
TerBR 3-13	451	160	Var, Var, Var (42)	66.9	128.5

Considering the results available in Tables 5.5 and 5.6, the higher values for jet penetration were observed in the trials employing top blowing patterns with a lance flow rate of 120 Nm^3/h and 400 mm of bath level distance (DBL). On the other hand, higher values of decarburization area were observed in the trials blown with a higher lance flow rate (160 Nm^3/h) and bath level distance (451 mm), this behaviour is illustrated in Figure 5.2.

The jet penetration, Figure 5.2-a, did not reach a large area because of the smaller bath level distance; the consequence is smaller decarburization areas and larger jet penetrations. Figure 5.3 schematically represents, for both cases, the place of the jet penetration. Figure 5.2-b shows minimized dead zones areas in the lower acrylic sides due to the higher amplitude of the jet penetration.
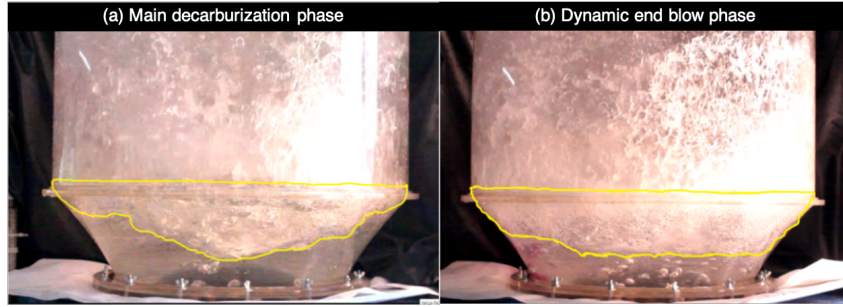
Figure 5.2: Comparison of decarburization area and jet penetration: (a) $TerBR\ 3-15$, and (b) $TerBR\ 3-13$ [30].

Due to the larger bath level distance and lance flow rate, the jet impacts a larger bath area, which offers higher resistance for jet penetration, increasing the droplets generation and consequently the water-gas interaction area [30]. Therefore, the top blowing pattern setup with 160 Nm^3/h may be more suitable for slag formation and dephosphorization.
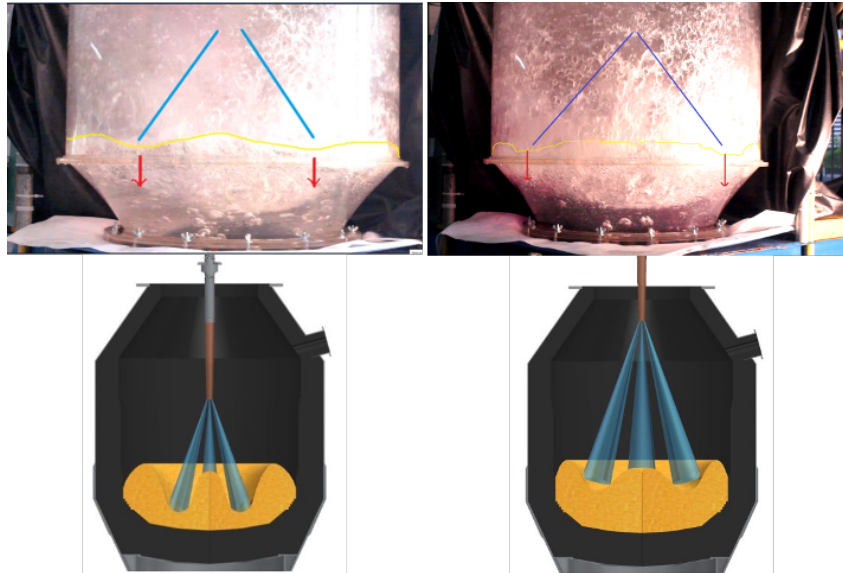
Figure 5.3: Jet impact scheme [30].

Due to the higher jet impact area in the outer radius of the plexiglass vessel, considering the blowing pattern employed at the final blow stages (160 Nm^3/h), a hypothesis regarding the bottom stirring influence on the jet penetration and the decarburization area is made. It is observed through the image analysis a possible shock between the top jet and the bottom stirring bubbles from the external radius, which may reduce the jet penetration and the decarburization area. This hypothesis is supported by the trial $TerBR\ 3-12$, in which lower values of jet penetration and decarburization area were related in a setup in which only the external bottom stirring elements were operating. Comparing the trials $TerBR\ 3-12$ and $TerBR\ 3-10$, it is important to highlight the better results found for the trials $TerBR\ 3-10$, focused on the central and internal radiuses of the bottom stirring elements, which suggests the preponderance of the internal and central radiuses of the bottom stirring elements.

Regarding the main decarburization phase ($BLD = 400\ mm$), similar results for the decarburization area were observed. These results indicate a preponderance of the top lance flow rate instead of the bottom stirring patterns, suggesting the use of $TerBR\ 3-15$ pattern, employing a minimal bottom stirring flow rate with satisfactory results for jet penetration and decarburization area.

5.1.1.3 Mass Transfer Rate - CO_2 Desorption

The desorption technique is adopted to simulate the decarburization process, especially in the final phase of the BOF blowing process, because the reaction takes place through the diffusion of the gas in the liquid metal.
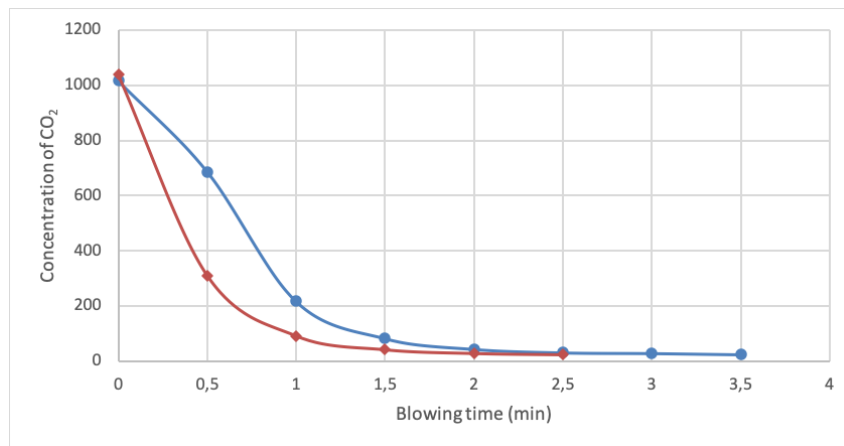
Figure 5.4: CO_2 Concentration x Blowing Time (blue TerBR 3-4; red TerBR 3-8) [30].

Figure 5.4 shows the measurements for two experiments, the concentration reduction rate for the CO_2 is more intense for the $TerBR\ 3-8$ trial, and it is justified by higher total blowing flow rate ($162.52\ Nm^3/h$), when compared to $TerBR\ 3-4$trial ($121.2\ Nm^3/h$). The higher flow rate is responsible for greater mixing energy, which increases the kinetics of the reactions. Therefore, increasing the flow rate is recommended for industrial practice to enhance decarburization.

A first-order kinetic equation was plotted considering the values of pH, and $[CO_2]$, in which the line slope describes the mass transfer constant (K_{tm}) for each configuration proposed, and tests were performed in triplicate. Figure 5.5 shows an example for the two trials, the mean and the standard deviation results for the mass transfer constants (K_{tm}) are shown in Table 5.7.

According to Table 5.7, experiments with higher lance flow rate ($160\ Nm^3/h$) showed higher values of mass transfer constants (K_{tm}) when compared to the lower lance flow rate ($120\ Nm^3/h$). This higher lance flow rate increased the mixing energy and the mass movement, supporting better decarburization in the blow's final phase. These results evidenced the top blowing influence on the mass transfer constants instead of the bottom stirring. The trials $TerBR\ 3-3$ and $TerBR\ 3-5$ showed higher values for the mass
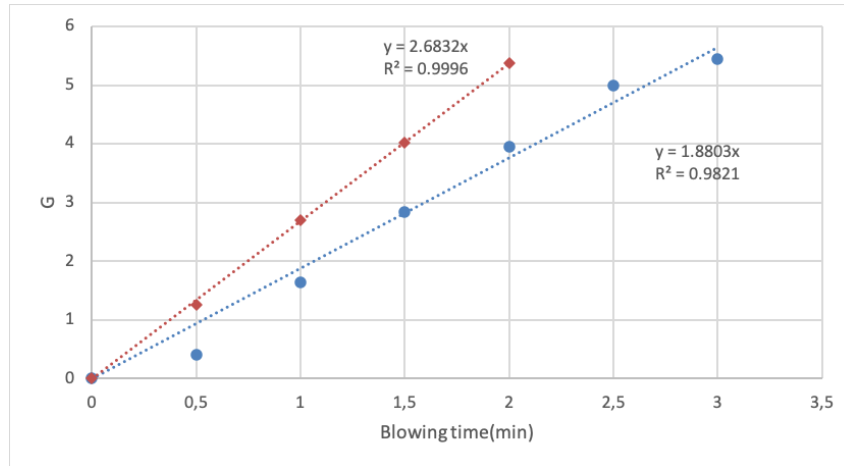
Figure 5.5: G (K_{tm} x t) x Blowing time (blue $TerBR$ $3-4A$; red $TerBR$ $3-8A$) [30].

Table 5.7: Experimental mass transfer (K_{tm}) rate coefficients [30].

Test	Lance flowrate (Nm³/hour)	TBM flowrate (NL/minute)	Total flowrate (Nm³/hour)	Mean K_{tm}	Standard deviation
TerBR 3-9	160	42	162.52	2.460	0.149
TerBR 3-8	160	20	161.2	2.425	0.222
TerBR 3-7	160	60	163.6	2.568	0.166
TerBR 3-2	160	40	162.4	2.349	0.160
TerBR 3-3	120	40	122.4	1.977	0.242
TerBR 3-4	120	20	121.2	1.902	0.025
TerBR 3-5	120	60	123.6	1.849	0.234
TerBR 3-6	120	42	122.52	1.934	0.157

transfer constants K_{tm}, despite having a lower bottom stirring (TBM) flow rate.

It is important to highlight the $TerBR$ $3-8$ and $TerBR$ $3-4$ experiments, both with bottom stirring flow rate of 20 Nl/min exhibiting equivalent mass transfer constants K_{tm} when compared to experiments with higher bottom stirring flow rate, $TerBR$ $3-8$ trial had a mass transfer constant higher than the $TerBR$ $3-2$ trial, both simulating the last phase of the blowing. However, the bottom stirring flow rate of $TerBR$ $3-2$ trial is the double of $TerBR$ $3-8$. Considering the main decarburization phase, trial $TerBR$ $3-4$ compared to $TerBR$ $3-5$ exhibited higher mass transfer constant results, even with lower bottom stirring flow rate, 20 Nl/min versus 60 Nl/min, respectively.

Through the analysis of the influence of the bottom stirring (TBM) on the CO_2 desorption trials, no correlation was found between the mass transfer constant (K_{tm}) and the total flow rate. Nevertheless, the bottom stirring configuration performed a significant role in the mass transfer constant (K_{tm}) results, and at the end of the blowing phase, it was observed a significant influence was observed of the central and the internal radius of the bottom stirring elements in the results of the mass transfer constant (K_{tm}).
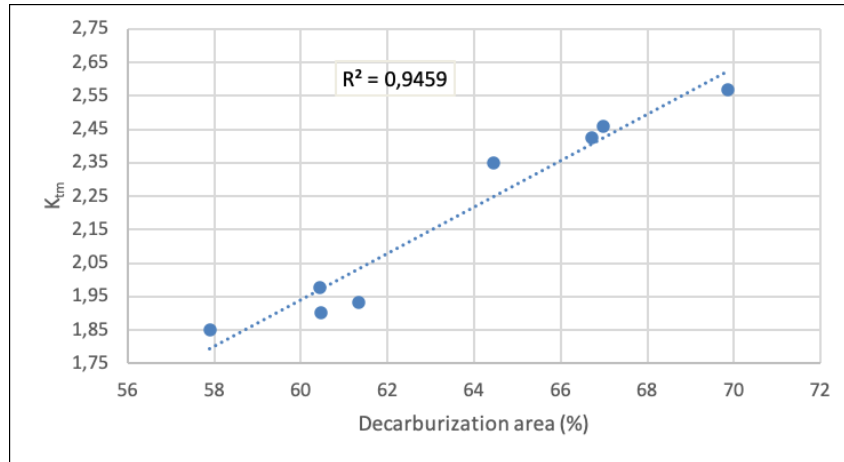
Figure 5.6: Mass transfer coefficient (K_{tm}) versus the decarburization area [30].

On the other hand, the main decarburization phase experiments exhibited another behaviour. A possible explanation is related to the different bath level distance (BLD), a smaller surface area of the bath is reached when the BLD decreases, impacting predominantly the central area of the vessel, which may negatively interfere the performance of the internal and central radius bottom stirring elements. Only the external radius of the bottom stirring elements was operating in the experiment $TerBR\ 3-3$, and this experiment illustrates the aforementioned behaviour in which a more extensive mass transfer constant K_{tm} result was faced.

Another analysis employed was the comparison between the decarburization area versus the mass transfer constant (K_{tm}), Figure 5.6, and a linear correlation was observed between the decarburization area and the mass transfer constant (K_{tm}).

5.1.2 Phase 2

Phase 2 experiments focused on the bottom stirring experiments in the tri-phasic system to replicate and evaluate bath homogenization, and the BOF mass transfer reactions. The efficiency of the refining reactions controlled by the mass transfer, linked to a kinetic knowledge, were examined over different bottom stirring element configurations and flow rate patterns.

The experiments consisted of a solvent extraction technique in a tri-phasic (water, soybean oil, and air) system. According to the similarity study, Section 4.1, the water and the oil express the liquid steel and the slag phase, respectively. A known benzoic acid solution was inserted into the water, and the concentration difference was controlled over the processing time while the benzoic acid was carried to the oil phase. The data of the proposed experiments were registered, and a plot for each trial was made to determine the mass transfer coefficient, defined by the slope of the linear fit for each experiment, Figure 5.7. The difference of magnitude for mass transfer coefficient comparing to Figure 5.6 was related to the different system, Figure 5.7 includes oil to simulate the slag phase.
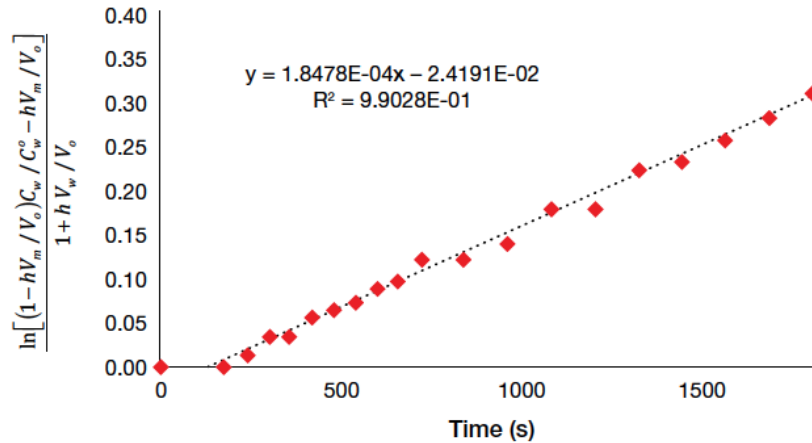
Figure 5.7: Mass transfer coefficient (K_{tw}) over time determination [209].

This section investigates and compares the mass transfer coefficients for different bottom stirring configurations and patterns (gas flow rate). First trials, section 5.1.2.1, focused on the influence of the total flow rate, and the bottom stirring flow rate setup performed with equal values for each element, the range of the total system flow rate was between 12 to 60 Nl/min, in steps of 12 Nl/min. In a second moment, to check the influence between the bottom stirring configuration and the mass transfer coefficients, trials were performed considering four different configuration setups, and a constant total flow rate of approximately 33 Nl/min, section 5.1.2.2. Table 5.8 shows the bottom stirring setpoints for all experiments performed to evaluate the bottom stirring configuration's influence.

Table 5.8: Bottom stirring pattern for each laboratory trial [209].

Trial	Tuyeres and individual flowrate				Total (Nl/min.)
	Internal and central (Nl/min.)		External (Nl/min.)		
LaSiP 1	4 x 2.8		8 x 2.8		33.6
LaSiP 2	4 x 1.6		8 x 3.3		32.8
LaSiP 3	4 x 5.0		8 x 1.6		32.8
Vortex	2.6 and 11	1.5 and 10	4.8 and 9	3.7 and 12	33.3
	3.6	3.0	2.5	2.0	

The trials employing the Vortex configuration had individual and gradual flow rate setpoints for each bottom stirring element, and the purpose of this gradual flow rate pattern was to induct an angular velocity component and then, a greater mixing area and gas residence time in the bath as well. Figure 5.8 shows the experimental bottom stirring schematic patterns, the bottom stirring elements labelled from 1 to 8 designates the external radius, 9 to 11 the internal radius, and number 12 describes the central

bottom stirring element.
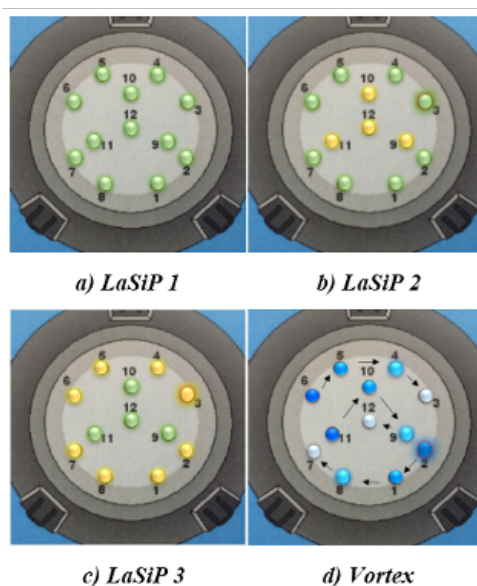
Figure 5.8: Schematic bottom stirring pattern [209].

The mass transfer coefficients were defined for all bottom stirring experiments, performed in duplicate to determine the average and the standard deviation. The experiments exhibited a confidence interval of 85% and 15% of tolerance.

5.1.2.1 Bottom Stirring Total Flow Rate Sensitivity for Same Setups

This section describes the influence of the bottom stirring total flow rate on the mass transfer coefficient. The bottom stirring setup employed the same configuration for all experiments, which means an equal distribution of the total flow rate between the twelve bottom stirring elements.
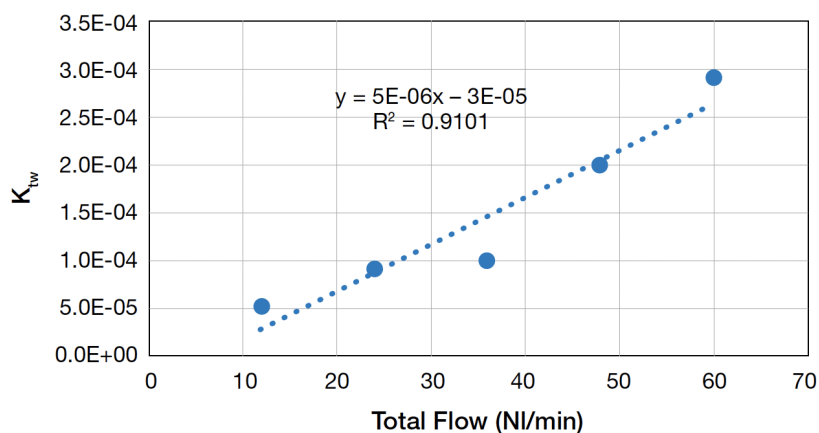
Figure 5.9: Mass transfer coefficients (K_{tw}) and total flowrate [209].

Figure 5.9 shows the experimental results for the mass transfer coefficients as a linear function of the total flow rate, and the mixing energy explains this behaviour. Larger flow

rates contribute to a more significant bath movement, which supports a greater interaction between water and oil phases, speeding up the benzoic acid transfer and the mass transfer coefficients.

5.1.2.2 Bottom Stirring Constant Flow Rate For Different Setups

This section describes the influence of the bottom stirring configuration on the mass transfer coefficient. The bottom stirring employed four different configurations, and a constant total flow rate of approximately 33 Nl/min for all experiments. Table 5.9 shows the experimental mass transfer coefficients, and LaSiP 1 registered the best performance.

Table 5.9: Mass Transfer Coefficients (K_{tw}) according to the bottom stirring configuration [209].

Configuration	Flowrate (Nl/min.)			Mass transfer coefficient	Standard deviation
	Internals	Externals	Total		
LaSiP 1	11.2	22.21	33.4	1.63 E-04	1.55 E-05
LaSiP 2	6.4	26.40	32.8	1.57E-04	4.03 E-07
LaSiP 3	20.0	12.80	32.8	1.08E-04	1.67 E-05
Vortex	11.0	22.00	33.0	1.52E-04	1.15 E-05

Supported by evaluating the oil/water interface through the recorded video, Figure 5.10 schematizes the observed flow pattern for each experiment.

Based on the interface behaviour, the pattern LaSiP 1 exhibited a more significant bath disturbance and a smaller stagnant area, represented by the light blue in Figure 5.10. The reduced flow rate in the internal radius of the bottom stirring elements in the LaSiP2 configuration demonstrated a decreased bath disturbance and a stagnant zone observed (through the video analysis) in the vessel's central area. On the other hand, LaSiP 3 exhibited an intense mixing near the internal radius of the bottom stirring elements and a larger stagnant zone near the converter walls, which is explained by the lower flow rate setpoint in the external bottom stirring radius. A flow pattern exhibiting a bath rotation behaviour was observed for the Vortex configuration, and the flow path starting in the bottom stirring elements with higher flow rate setpoints. The interface agitation was similar to LaSiP 2.

The results' analysis shows a more uniform gas distribution for configurations with higher bottom stirring flow rate, promoting a better interaction between the water and the oil phases, resulting in more significant mass transfer coefficients.

The bottom stirring configurations with higher mass transfer coefficients displayed less stagnant zones. Despite the interface similarity between the Vortex and LaSiP 2 bottom stirring setup, the flow produced by the Vortex mixed the bath horizontally, which limited the mixing between the oil/water interface, reducing the mass transfer coefficients. LaSiP 1 and LaSiP 2 exhibited very close results. A suitable decision would consider the cost
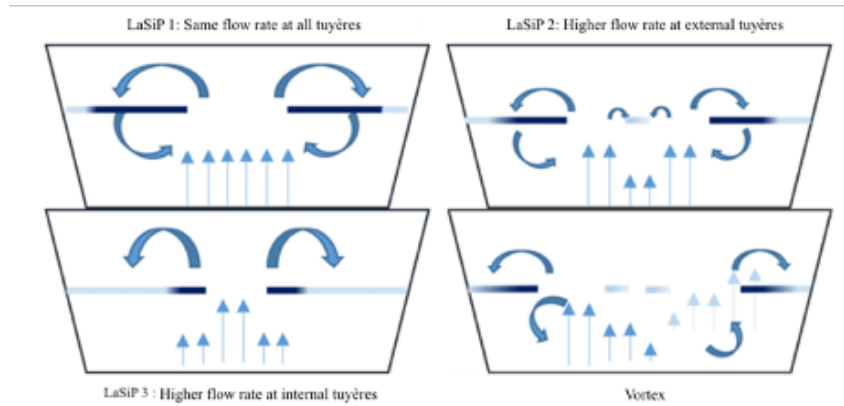
Figure 5.10: Schematic flow behavior according to each bottom stirring blowing pattern [209].

and the benefits of implementing LaSiP 2 setup, since this configuration holds a good bath mixing, and would reduce the refractory in the internal bottom stirring circle.

Another relevant process impact was related to the outer bottom stirring circle, the bottom stirring setups with a higher flow rate in the outer circle exhibited higher mass transfer coefficients, showing a direct impact on reducing the stagnant zones. It is important to remark that Phase 2 considered only the bottom stirring in all experiments, and the trials did not employ the blowing from the top lance.

5.1.3 Phase 3

Biphasic and triphasic tests were performed to understand the influence of the top lance blowing patterns on the bottom stirring setups previously discussed in Section 5.1.2, the investigations employed the luxmeter and conductivity meter measurement techniques to investigate the mixing time.
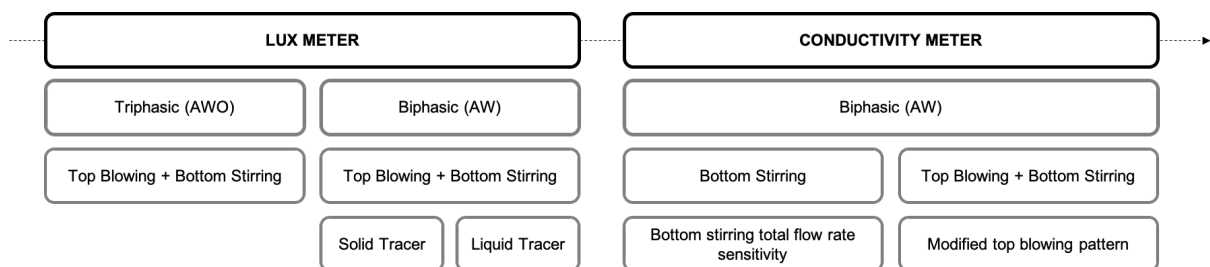
Figure 5.11: Chronology of laboratory phase 3 experiments.

Firstly, the triphasic system's trials employed the luxmeter technique applying the liquid tracer, to increase the system visualization by decreasing the homogenization speed, a change to the solid-state tracer was made. Next, the conductivity meter technique was introduced to validate the luxmeter method's results for biphasic experiments. Figure 5.11 illustrates the chronology of the experiments.

According to Figure 5.11, trials were focused on the combined top blowing and bottom stirring. The top blowing setups' laboratory parameters are shown in Table 5.10, and the

Table 5.10: Top blowing pattern parameters.

Top Blowing Parameters	Unit	Setup #1	Setup #2	Setup #3	Setup #4
Bath Level Distance	m	0.40	0.45	0.40	0.45
Oxygen Flow Rate	$Nm^3.h^{-1}$	120	160	160	120

bottom stirring parameters are illustrated in Figure 5.12, all experiments were labelled employing this nomenclature.
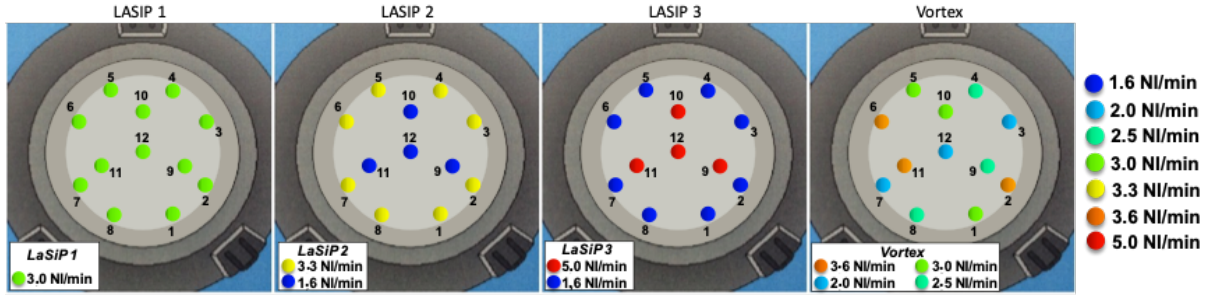
Figure 5.12: Bottom stirring pattern parameters.

5.1.3.1 Luxmeter

The experiments employing the luxmeter measurement technique was performed in a triphasic and biphasic system, both for the combined top blowing and bottom stirring simulations. Figure 5.13 shows the luxmeter results for the Vortex and LaSiP 3 bottom stirring patterns, both employing *Setup* #1 for the top blowing parameters. Just after the bottom stirring flow rate activation, depending on the bottom stirring configuration employed, a decrease of luminance measurement was observed.
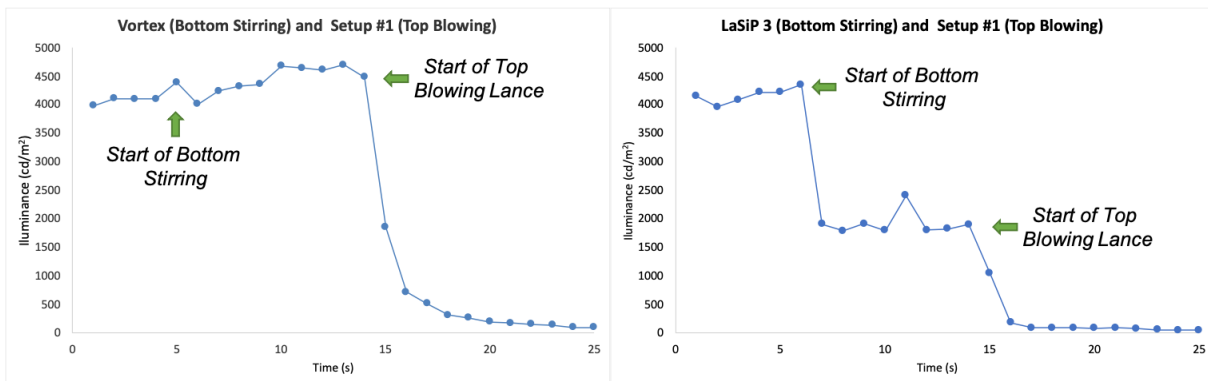
Figure 5.13: Behavior of the light measurement employing Vortex and LaSiP 3 configuration, and both with *Setup* #1 top blowing parameters.

As shown in Figure 5.13, this behaviour was observed in the LaSiP 3 configuration and occurred because the bubbles pass over the sensor, which affected the light measurement, exposing the equipment's sensitivity in the macrosystem modifications.

Assuming the mixing criteria as $\pm 5\%$, according to Figure 5.14 the mixing time results for LaSiP and Vortex arrangements were 6 seconds. It was also possible to observe the reduction of the lux measurements around 3 seconds after the process started, and considering the data collection of 1 input per second, which may suggest an inappropriate frequency for data collection, requiring to change the luxmeter sensor or the technique in order to investigate the proposed process.
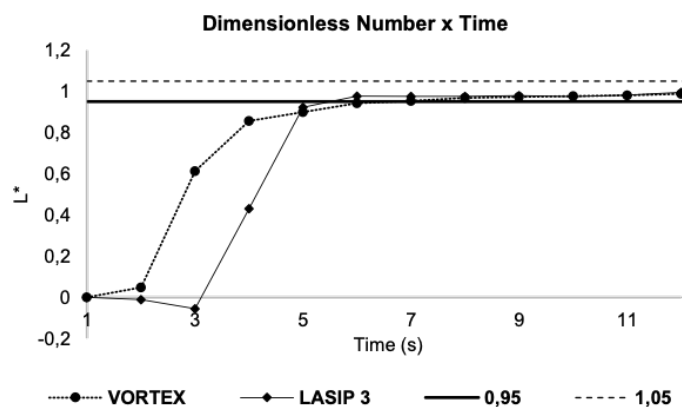
Figure 5.14: Mixing time for different bottom stirring arrangements using the liquid tracer, and employing the luxmeter dimensionless number L^*.

An inconsistency regarding the mixing time was observed when comparing the experimental data measurements and the recorded video. At a specific time, the bath was considered homogenized through the data analysis. However, the video analysis did not indicate a complete homogenization at the bottom of the vessel, Figure 5.15.
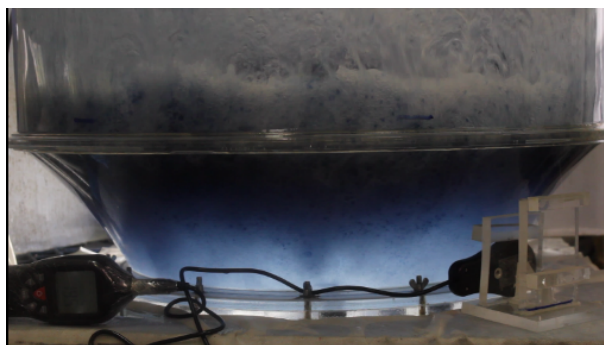
Figure 5.15: Bottom of the cold modelling at a especific time when the bath was considered homogenized through the luxmeter data analysis.

According to the expectation, the mixing time measurements increased after adopting the solid tracer, prepared with a potassium permanganate supersaturated solution. However, the evaluation of the curves for each bottom stirring configuration, plotted using the dimensionless lux numbers, did not accurately distinguish the best bottom stirring configuration simulated, Figure 5.16.

It is important to remark that Figure 5.16 shows the results for the bottom stirring simulations, the combined bottom stirring and top blowing experiments were performed

similarly and, as expected, it was more challenging to define the best configuration, due to the shorter mixing time results.
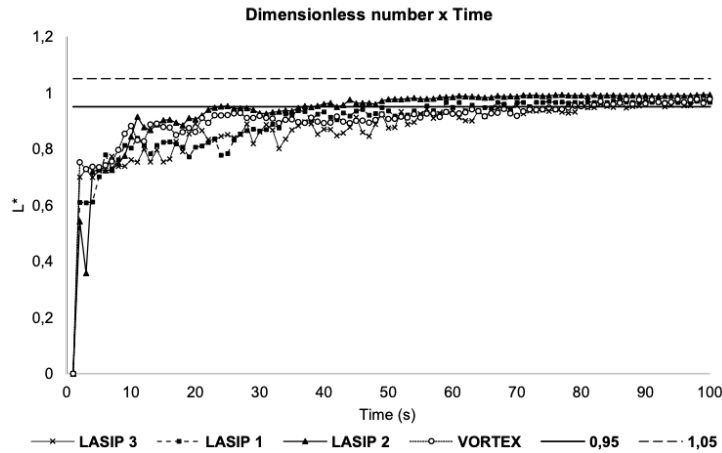
Figure 5.16: Mixing time for different bottom stirring arrangements using the solid tracer, and employing the luxmeter dimensionless number L^*.

5.1.3.2 Evaluation Of The Measurement Methods

Because of the uncertainty to define the best configuration employing the luxmeter technique, Section 5.1.3.1, it was proposed to introduce the conductivity meter measurement methodology to evaluate and compare the luxmeter technique. Bottom stirring experiments were performed in triplicate for both methodologies, Figure 5.17 introduces the comparison for the dimensionless concentration (C^*) during the processing time for both methodologies, in this example, employing the bottom stirring Vortex pattern.
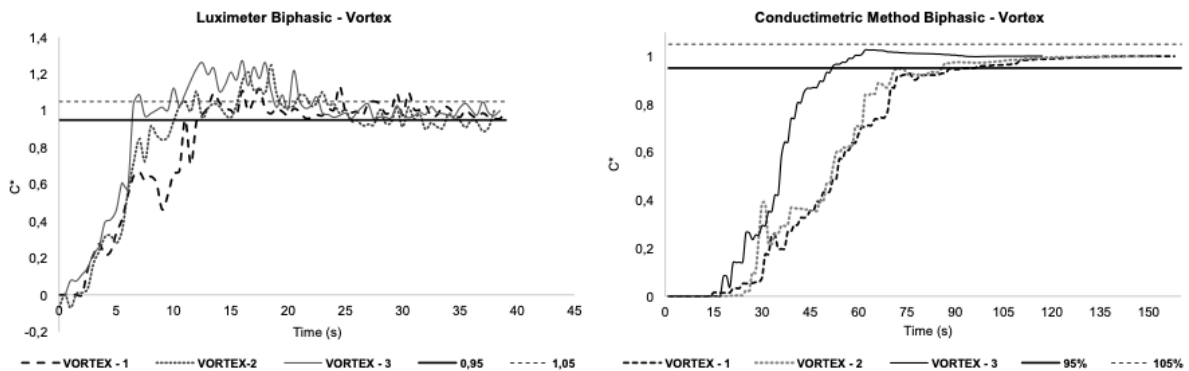
Figure 5.17: Triplicate of the biphasic tests using the luxmeter and conductivity meter technique for the Vortex configuration.

Figure 5.18 shows the average mixing time results comparing bottom stirring experiments employing both measurements methodologies. The luxmeter results exhibited shorter mixing times, which may indicate an incomplete homogenization, even after an extended period, with complete homogenization of the bath, the lux values varied widely, which may indicate the equipment's inevitable inaccuracy.
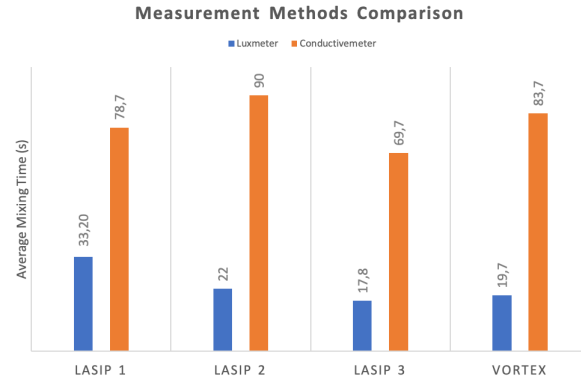
Figure 5.18: Average mixing time (s) for bottom stirring experiments employing both measurement methodologies.

Through evaluation of the regressions obtained in the calibration curves, Figure 4.11, it was possible to observe the luxmeter inefficiency to capture the light difference for particular tracer's concentrations, and the video analysis showed the bath already coloured without complete homogenization, which impaired the mixing time determination.

5.1.3.3 Conductivity meter - Biphasic System

Based on the comparison of the luxmeter and the conductivity meter measurement methodologies, Section 5.1.3.2, a more in-depth evaluation of the different configurations using the conductivity meter technique was necessary to define the best configuration.
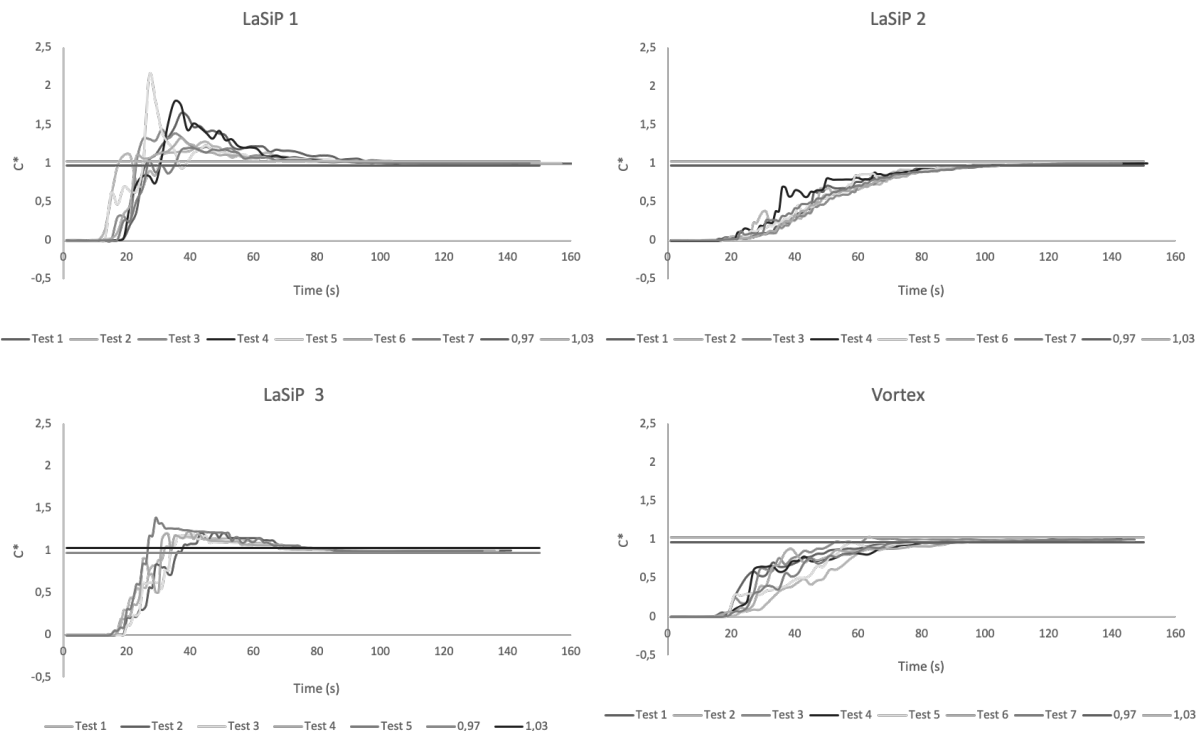
Figure 5.19: Dimensionless concentration (C^*) for different bottom stirring configurations, employing the conductivity meter technique.

The first trials were focused on the bottom stirring total flow rate sensitivity analysis, Figure 5.19 shows the mixing time for the different bottom stirring configurations, the graphs exhibit the obtained dimensionless concentration (C^*) versus time.

The data generated by the conductivity meters were compared, and the mixing time defined for each configuration using the values of the equipment in which the highest average results were conferred. Figure 5.20 displays the box-plots of the measured mixing times for the different configurations.
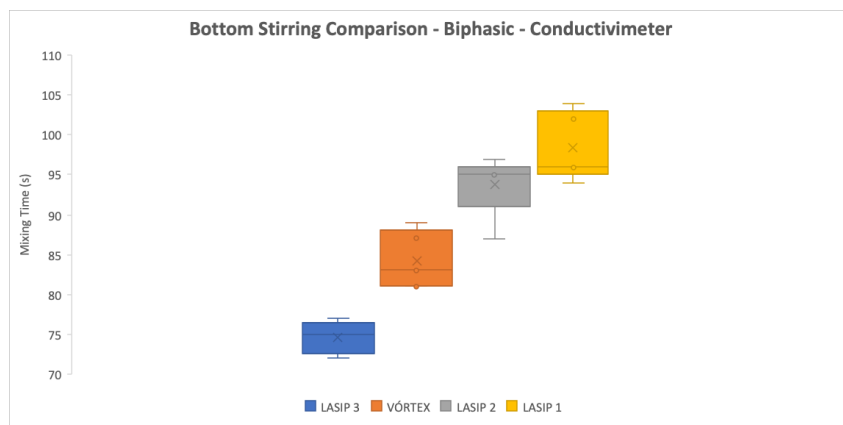
Figure 5.20: Mixing time (s) box-plot for each bottom stirring configuration.

Through analysis of the graph, a considerable difference in the mixing times was observed when changing the bottom stirring arrangement. The LaSiP 3 configuration showed the shortest mixing time in the tests performed. According to Figure 5.12, the bottom stirring's internal and central radiuses were configured with the maximum flow rate and the external radius set up with a minimum flow rate.

The same methodology was applied to investigate the flow rate sensitivity analysis for LaSiP 3 and Vortex configurations, Figure 5.21 and 5.22 respectivelly shows an expected shorter mixing time for higher flow rates.
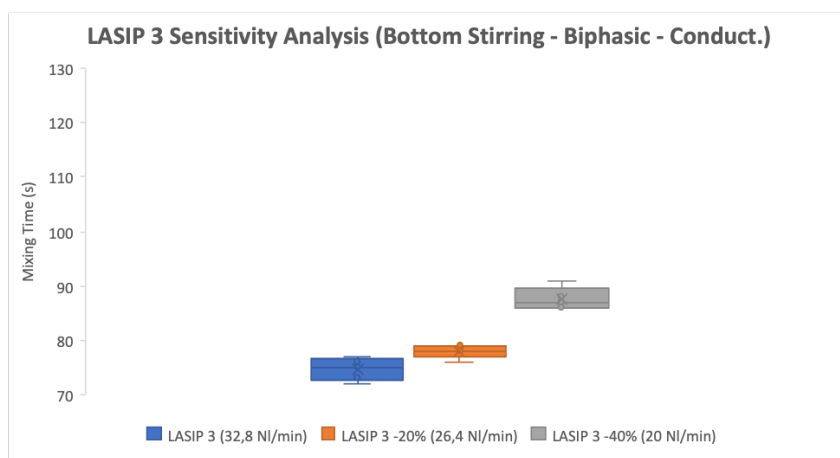
Figure 5.21: Bottom stirring flow rate sensitivity analysis for LaSiP 3 configuration.

The second phase of the trials focused on the combined top blowing and bottom

stirring trials. Combination of different top blowings, Table 5.10, and bottom stirring setups were investigated, Figure 5.12.
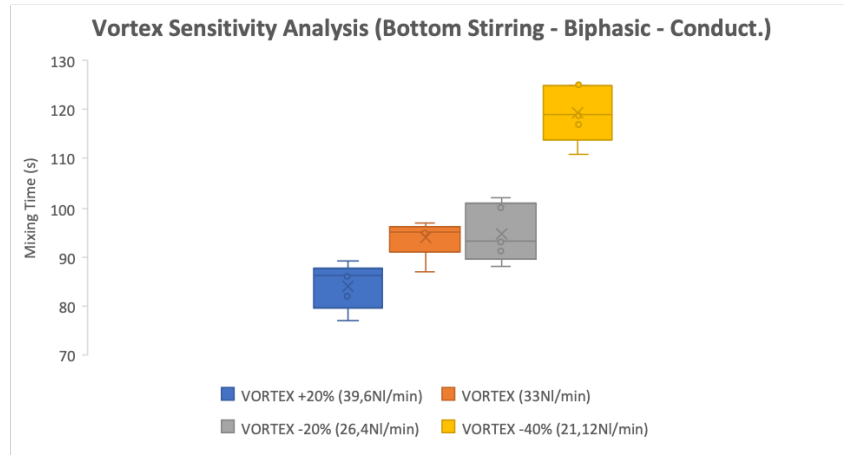
Figure 5.22: Bottom stirring flow rate sensitivity analysis for Vortex configuration.

The mixing time investigations for the different top blowing setups, keeping a constant bottom stirring pattern (LaSiP 3), showed a significant influence of the lance flow rate, and a reduction of approximately 20% in the mixing time was observed when changing the lance flow rate from 120 to 160 $Nm^3.h^{-1}$, Figure 5.23. On the other hand, the bath level distance (BLD) did not show enough differentiation to determine the mixing time under these specific conditions.
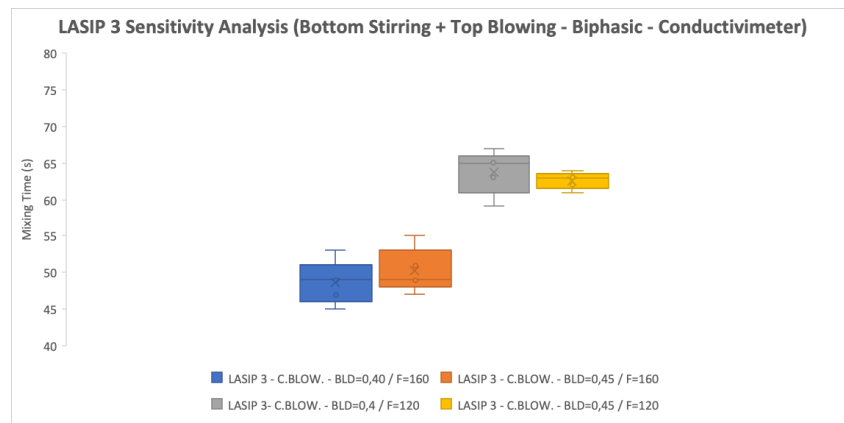
Figure 5.23: Box-plot analysis comparing mixing times for different top blowing setups, results for fixed bottom stirring pattern (LaSiP 3).

Once defined the two top blowing setups, investigations of different bottom stirring configurations to evaluate the mixing time were performed. The bottom stirring patterns did not significantly influence the mixing time results considering the combined process with the top blowing, employing *Setup* #1 and *Setup* #2, Figure 5.24 and 5.25 respectively.

Both tests showed that the lance flow rate, during the combined top blowing and bottom stirring, was the parameter with the most significant influence on the mixing time

compared to the injection through the bottom stirring and different bath level distances (BLD).
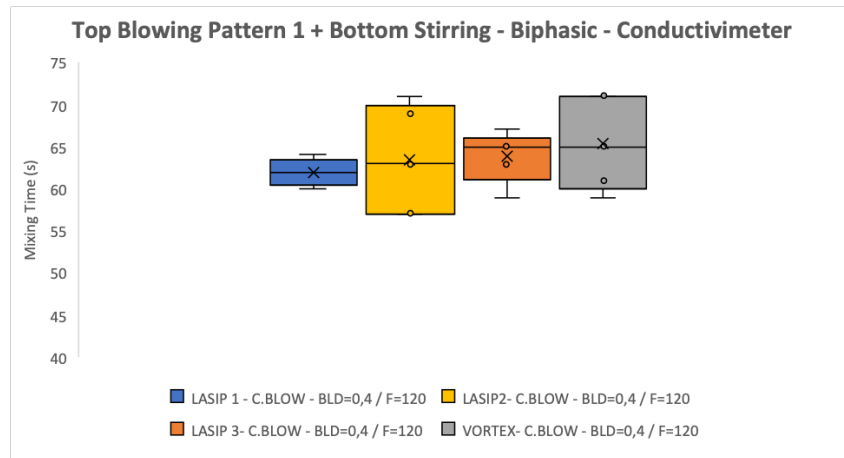
Figure 5.24: Mixing time box-plots comparing different bottom stirring patterns for top blowing Setup #1.
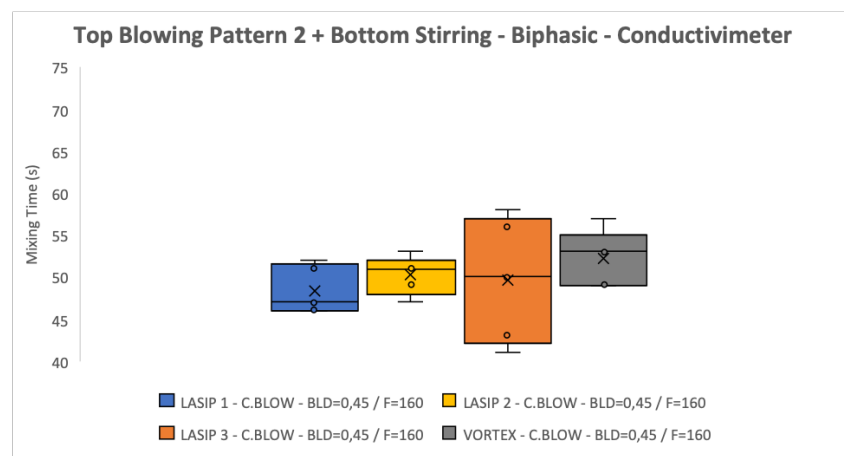
Figure 5.25: Mixing time box-plots comparing different bottom stirring patterns for top blowing *Setup* #2.

5.2 Industrial Tests

Industrial-scale production of 1750 trial heats, Table 5.11, was performed in the 330 t BOF to validate and investigate the different configurations and patterns proposed as results of the laboratory experiments, Section 5.1. The first phase of the trials, Section 5.2.1, aimed to replicate the same bottom stirring patterns employed for the laboratory experiments, Section 5.1.2. This phase aimed to run a minimum number ($\approx 100 - 150$) of heats to have the chance to execute all the proposed patterns, and sufficient enough to provide data for further statistical analysis.

The experimental heats of Phase 2, Section 5.2.2, were defined according to the industrial outcomes of phase 1, Section 5.2.1, and the results of laboratory experiments

Table 5.11: Summary of the performed industrial BOF trial heats.

#	Configuration	Trial Heats	Bottom Stirring Elements	Section
Phase 1	TerBrK2	150	12/12	
	LaSiP 1	127	12/12	
	LaSiP 1.1	59	11/12	
	LaSiP 1.2	136	11/12	5.2.1
	LaSiP 2	102	11/12	
	LaSiP 3	142	11/12	
	Vortex	145	12/12	
Phase 2	LaSiP 3	450	12/12	
	Regular	447	12/12	5.2.2

of phase 3, Section 5.1.3. This experimental phase focused on performing one bottom stirring pattern for a longer-term, and the higher number of data allowed to perform a deeper statistical analysis, which included a machine-learning algorithm to check the performance between the experimental and regular production.

5.2.1 Phase 1

Industrial trials were proposed to replicate the bottom stirring laboratory examinations performed in phase 2, Section 5.1.2. Usually, the bottom stirring total flow rate shifts according to the blowing process phase, and adaptations in the industrial bottom stirring patterns were necessary to perform the experiments. A constant flow rate of $10 \ Nm^3.min^{-1}$ was defined through the blowing process to reduce the complexity of the trials. Figure 5.26 displays the regular and the proposed bottom stirring patterns.
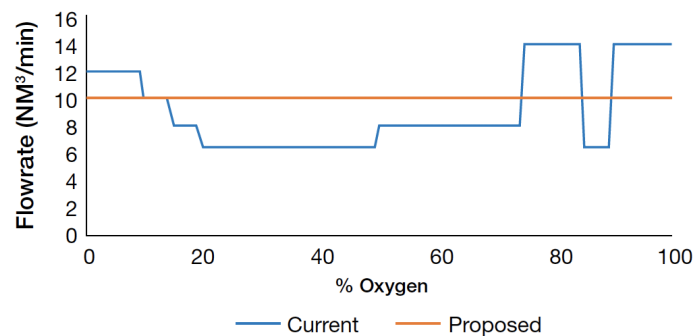
Figure 5.26: Regular and proposed bottom stirring industrial patterns [30].

The configurations tested in the cold model were replicated at the BOF converters of Ternium Brazil. Figure 5.27 exhibits a schematic drawing of the replicated tests configuration. It was decided that the tests were carried out in converter 2, at that time, the

reactor with lower lining time and better bottom blowing performance.
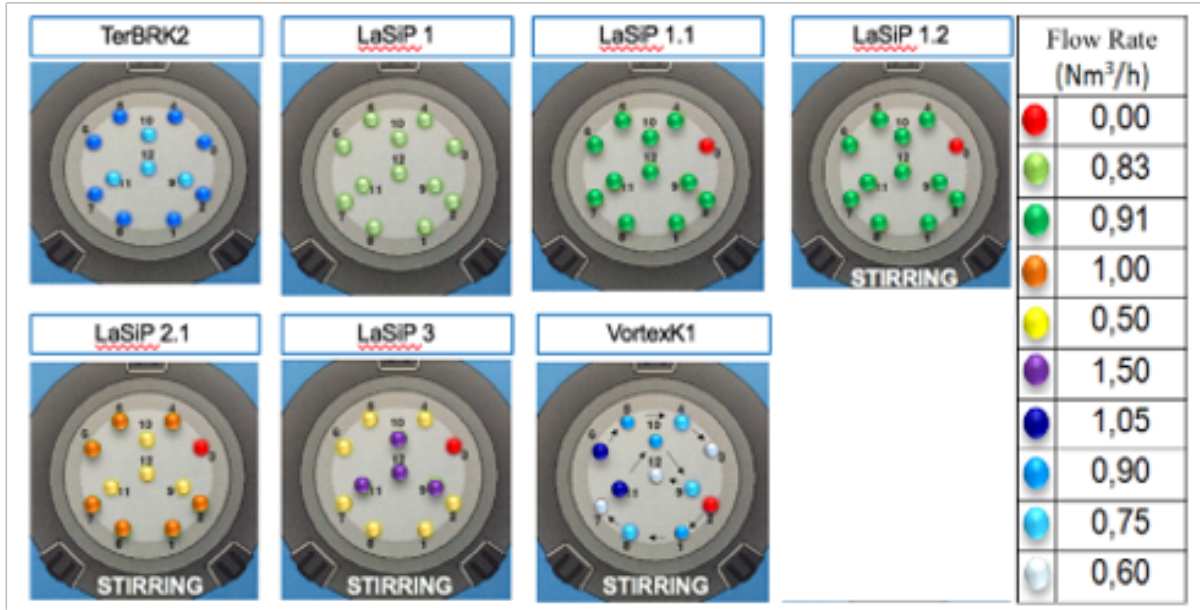
Figure 5.27: Bottom stirring schematic patterns setup for industrial experiments [30].

Due to process restrictions and sudden industrial difficulties, modifications were required. After starting the trials, the obstruction of one of the bottom stirring elements was faced (LaSiP 1.1 afterwards), and the implementation of the constant flow rate for the stirring phase was not fully completed before LaSiP 1.2. The step between the end of top blowing and the tapping is the stirring phase, a crucial process phase in which only the bottom stirring is active to remove the gas from the bath and improve segregation between metallic bath and slag, improving the metallurgical results. The regular process bottom stirring patterns, $TerBRK2$, was also evaluated, in which 20% of the internal radius bottom stirring flow rate is transferred to the external bottom stirring radius.

After defining the setup of the trials, key performance parameters were delimited to evaluate the influence of each bottom stirring pattern during the process. Dephosphorization degree (η_P), manganese oxidation (η_{Mn}), CxO ratio and slag oxidation levels (Fe_T) were determined as key parameters.

The dephosphorization degree (η_P), and the manganese oxidation (η_{Mn}), were defined according to the ratio between input (hot metal) versus the output (steel) of phosphorus and manganese content, Equations 5.1 and 5.2 respectively.

$$\eta_P = \frac{P_{input} - P_{output}}{P_{input}} \tag{5.1}$$

$$\eta_{Mn} = \frac{Mn_{input} - Mn_{output}}{Mn_{input}} \tag{5.2}$$

Where, η_P – dephosphorization degree (-), P_{input} – initial phosphorus content input from hot metal (%), P_{output} – final phosphorus content measured in the steel sample (%),

η_{Mn} – manganese oxidation (-), Mn_{input} – initial manganese content input from hot metal (%),and Mn_{output} – final manganese content measured in the steel sample (%),

The maximum values to be obtained in Equations 5.1 and 5.2 are equal to one (1), equivalent to 100% removal. Considering an ideal and hypothetical metallurgical performance, a high dephosphorization degree associated to a high manganese recovery is the aim of the process, which means η_P closer to one (1), and η_{Mn} closer to zero (0). Therefore, this investigation focused on defining the bottom stirring configuration in which a higher dephosphorization is performed combined with a good manganese recovery.

Two steel samples are regularly collected in the BOF process through the automatic sublance sampling system. Just before the end of the blow, after the critical carbon (around $85 - 90\%$), the inblow sample is taken and labelled as sample 200 at Ternium Brazil. After the blowing end, around two minutes of bottom stirring is planned before collecting the end of blow sample, labelled as 210.

Unlike the cold simulations, the regular industrial process is performed through the combined top blowing and bottom stirring, and several parameters and noisy data influence the industrial process measurements and results.

According to Equation 5.1, Dephosphorization degree correlates the steel phosphorus removal, higher values of η_P means more efficient dephosphorization. On the other hand, maintaining the Manganese (Mn) in liquid steel is desired to reduce the Mn alloying after tapping. According to Equation 5.2, lower values of η_{Mn} implies in a higher recovery of Mn in the steel bath, and it is important to highlight that this plant does not adopt additions of different manganese sources over the blowing process. The manganese source comes basically from the hot metal and scrap sources.

The results for the manganese recovery and dephosphorization degree in the BOF process are inversely proportional, and a suitable bottom stirring configuration would deliver a good dephosphorization (η_P) degree with a proper manganese recovery (η_{Mn}). Table 5.12 exhibits the results for the Dephosphorization (η_P) degree, Manganese oxidation (η_{Mn}), slag oxidation level (Fe_T) and CxO ratio.

Table 5.12: Dephosphorization and Manganese oxidation levels at in-blow (200) and end-blow (210) sample, slag oxidation level (Fe_T) and CxO ratio [30].

Configuration	ηP (200)	ηP (210)	ηMn (200)	ηMn (210)	Fe$_T$ (%)	CxO
TerBRK2	0.56±0.16	0.87±0.04	0.28±0.01	0.68±0.07	18.20±2.11	15.80±4.47
LaSiP 1	0.65±0.16	0.87±0.04	0.43±0.02	0.72±0.06	19.06±1.99	17.51±6.25
LaSiP 1.1	0.60±0.16	0.86±0.04	0.34±0.02	0.69±0.06	17.84±1.99	19.26±3.70
LaSiP 1.2	0.67±0.14	0.87±0.04	0.44±0.02	0.73±0.07	18.09±2.40	17.97±5.20
LaSiP 2	0.59±0.14	0.82±0.05	0.32±0.04	0.66±0.05	18.52±1.54	19.77±5.40
LaSiP 3	0.71±0.14	0.87±0.04	0.40±0.02	0.71±0.08	18.66±2.38	20.81±4.83
Vortex	0.59±0.11	0.88±0.04	0.17±0.01	0.63±0.10	18.13±2.27	15.56±4.49

Considering the inblow sample (200), LaSiP 3 performed the highest dephosphoriza-

tion (η_{P-200}) degree, while the best manganese recovery (η_{Mn-200}) was observed for the Vortex configuration. Regarding the end of the blow sample (210), Vortex configuration was the most efficient for both parameters. Nevertheless, it is important to remark the close results for the end of blow dephosphorization degree (η_{P-210}) when comparing LaSiP 3 and Vortex configuration. To support the direct tapping decision, LaSiP 3 is highly recommended because it delivers a very good dephosphorization (η_{P-200}) degree already in the inblow measurement, reducing processing time.

The average results of slag oxidation levels (Fe_T) were similar, so regardless of the configuration selected, the metallurgical results would be satisfactory. The Vortex configuration showed the best results for the CxO product. The obtained industrial results assessed some specific process variables, which correlated to the steel-slag mass transfer, as well as to the decarburization process.

5.2.2 Phase 2

According to the results of the first industrial tests, Section 5.2.1, and the third phase of the laboratory trials, Section 5.1.3, a larger scale test was proposed, and approximately 900 heats were blown in the industrial 330 t BOF of Ternium Brazil. The sequence of the trials started in heat number 160 after the relining. It means, in the trials, new bottom stirring elements were available and performing according to plan, Figure 5.28.

Figure 5.28: BOF bottom stirring elements after relining (12 of 12 available).

LaSiP 3 pattern was selected for the 450 trial heats due to the previous results, and another 450 heats were blown according to the regular blowing pattern, Table 5.13.

According to Figure 5.29, both groups of heats had a similar $\%Si$ in the hot metal, and the same average temperature at the end of blow T_{EOB} (°C), essential parameters to

Table 5.13: Industrial Bottom Stirring - Flow Pattern.

Step	Trigger	Regular Process - 447 heats		Trials - LaSiP 3 - 450 heats		
		Total	Individual	Total	Internal	External
#	$\%O_2$	$Nm^3.min^{-1}$	$Nm^3.min^{-1}$	$Nm^3.min^{-1}$	$Nm^3.min^{-1}$	$Nm^3.min^{-1}$
1	5	8	0.67	6.67	0.67	0.50
2	15	8	0.67	6.67	0.67	0.50
3	25	8	0.67	6.67	0.67	0.50
4	30	8	0.67	6.67	0.67	0.50
5	40	8	0.67	6.67	0.67	0.50
6	50	8	0.67	6.67	0.67	0.50
7	75	8	0.67	6.67	0.67	0.50
8	88	10	0.83	7.33	0.83	0.50
9	90	10	0.83	10.00	0.83	0.83
10	100	12	1.00	10.00	1.00	1.00

assure similar conditions between the two groups.

Measuring the dephosphorization in the BOF process was fundamental to quantify the slag formation, the core of this section was to check the dephosphorization for both groups, which meant a comparison between trial versus regular heats. The dephosphorization reactions are complex and influenced by many parameters, such as the combination of Phosphorus partition capacity (L_P), slag volume and kinetics over the main blowing and stirring phase [210]. So, to define the best dephosphorization, a depth evaluation through a statistical approach is necessary.
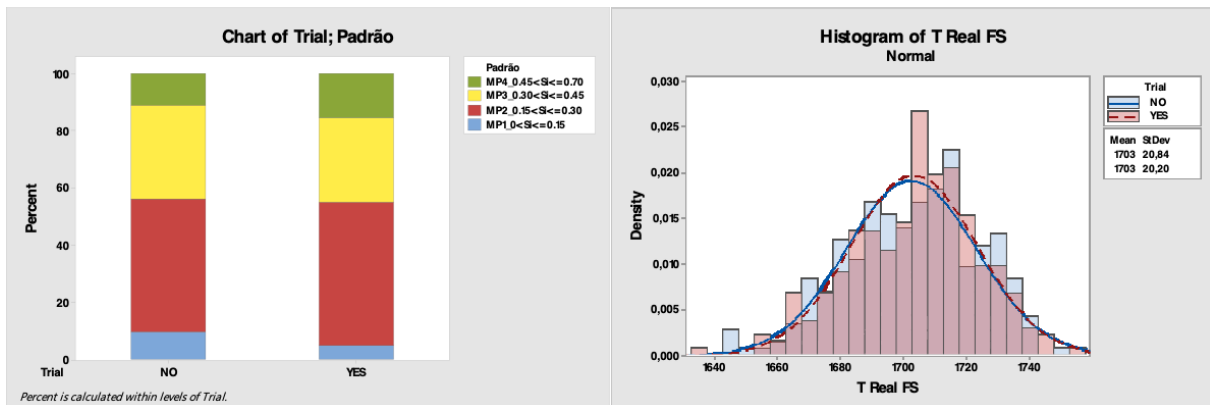
Figure 5.29: Operational data comparing the $\%Si$ of the hot metal (left) and the end of blow temperature, T_{EOB} (°C) (right).

P-partition (L_P), Equation 5.3, is the capacity to retain phosphorus in the slag phase in contact with the liquid steel, in form of stable P_2O_5. The efficiency of phosphorus removal (η_P), Equation 5.1, covers the phosphorus partition (L_P), slag mass and dephos-

phorization kinetics [210].

$$L_P = \frac{(\%P)}{[\%P]} \tag{5.3}$$

In the BOF process, the aimed dephosphorization is defined by the difference of hot metal phosphorus (plus other inputs), and target phosphorus, according to the quality specification. To obtain maximum phosphorus removal (η_P), a higher phosphorus partition (L_P) is required. Nevertheless, according to Figure 5.30, to achieve a different η_P is possible even for similar L_P.
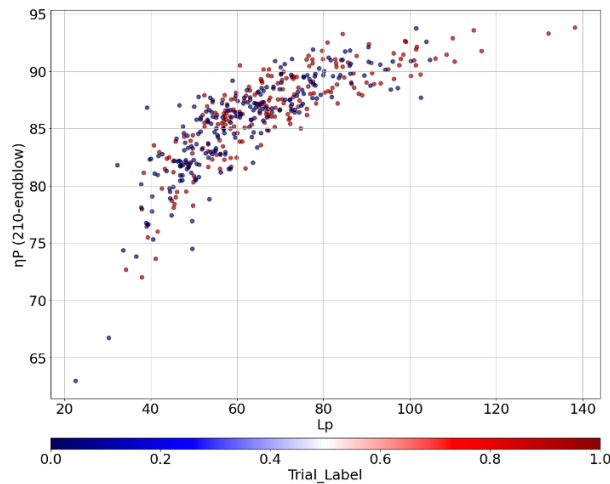
Figure 5.30: Dephosphorization eficiency (η_P) for different phosphorus partitions (L_P). Regular heats labelled as 0, and trial heats labelled as 1.

Figure 5.30 shows the data for the trial and regular heats, respectively labelled as 1.0 (red) and 0.0 (blue). Based on this scatterplot, defining the best group regarding dephosphorization efficiency is not so clear, because other factors may influence the phosphorus partition (L_P) results.
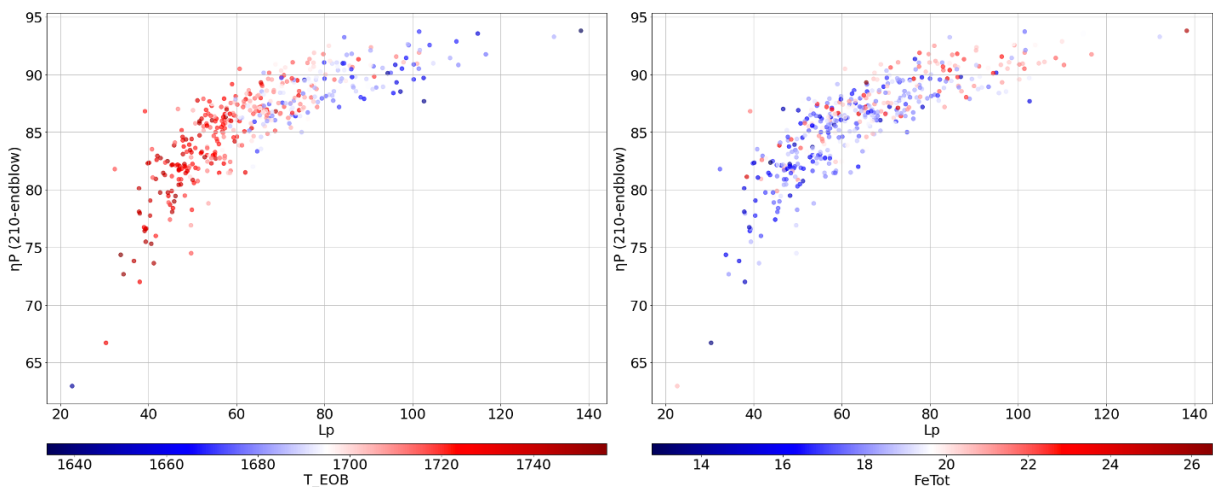
Figure 5.31: Phosphorus removal efficiency (η_P) for different phosphorus partitions (L_P) according to the influence of T_{EOB} (°C) (left) and the slag oxidation, Fe_T (right).

Figure 5.31 confirms the high influence of T_{EOB} and the slag Fe_T on the effect of the phosphorus removal efficiency (η_P) for different phosphorus partitions (L_P). Higher L_P results are obtained for lower T_{EOB} and higher slag oxidation (Fe_T), and confirms the possibility of different η_P even for similar L_P.
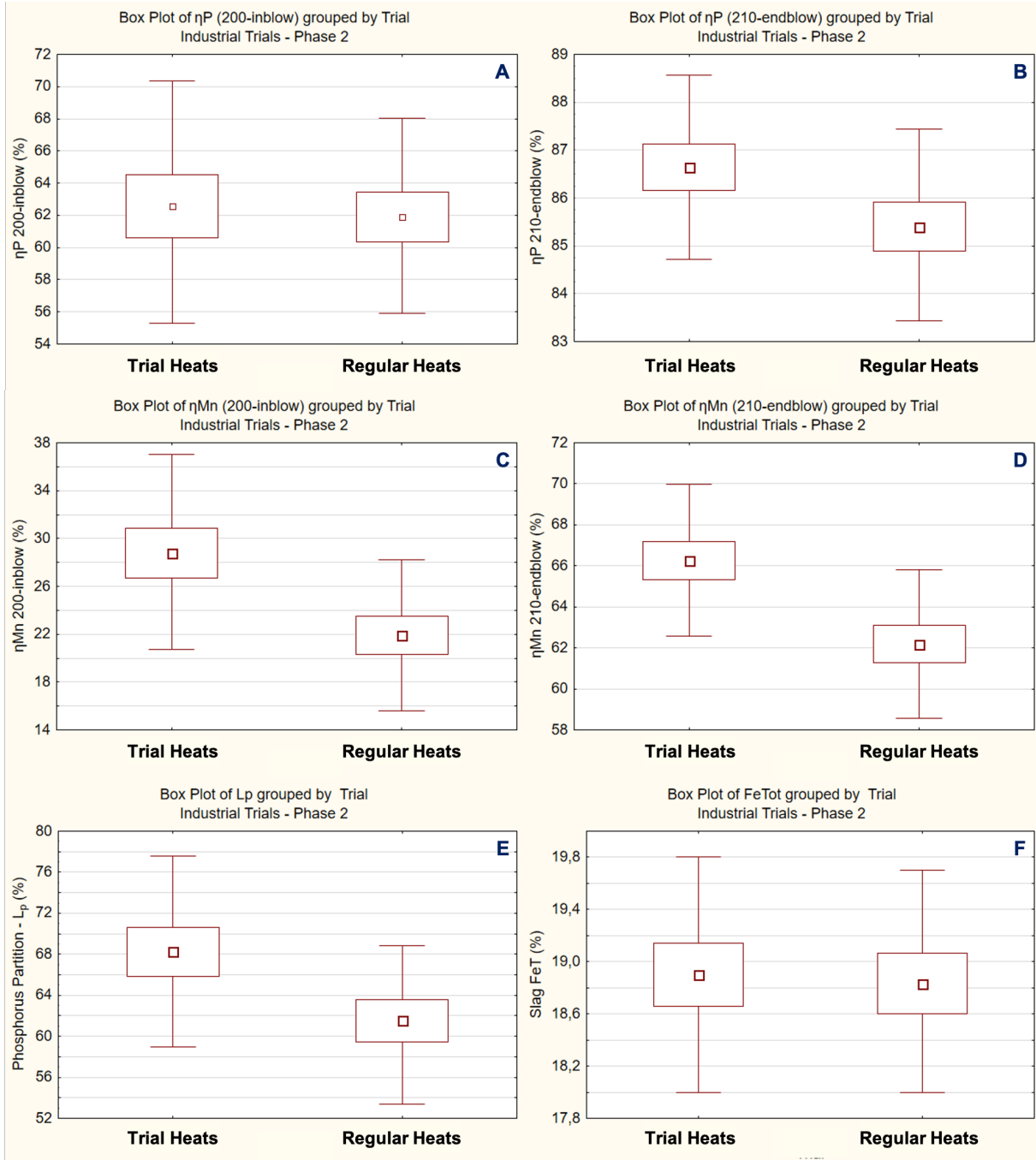
Figure 5.32: Metallurgical results comparing the $\eta_{P\,200}$ in the inblow sample (A), $\eta_{P\,210}$ in the EOB sample (B), manganese oxidation levels in the inblow sample $\eta_{Mn\,200}$ (C), and in the EOB sample $\eta_{Mn\,210}$ (D), slag oxidation (Fe_T) (E), and phosphorus partition L_P (F). Box plots label, mean value: □, mean±0.95 conf. interval: ▢, and non-outlier range: ⊥.

Figure 5.32 compares the metallurgical results through the two groups (trials vs reg-

ular) box plot. Important metallurgical parameters are shown, and this evaluation evidenced the best performance for the trial group. The trial group showed improved results for the L_P, $\eta_{P\,210}$ in the EOB sample, $\eta_{P\,200}$ in the inblow sample, slag oxidation (Fe_T). On the other hand, a higher level of manganese oxidation was observed in the inblow $\eta_{Mn\,200}$, and in the EOB sample $\eta_{Mn\,210}$. The inblow sample results showed a better slag formation, and the indication is that the higher level of manganese oxidation ($\eta_{Mn\,200}$) was associated to the better phosphorus removal efficiency ($\eta_{P\,200}$). This result is essential for the BOF process, a good dephosphorization until the inblow sample gives the operator a higher level of confidence, which allows a fast decision for direct tapping.

Despite the previous box plots showing better performance for the trial groups, it was still necessary to check the individual performance for each parameter on a broader range, and a better dephosphorization is observed in the scatterplot comparing the $\eta_{P\,210}$ in all the range of T_{EOB} ($°C$), Fe_T (%), O_2 (ppm) and CxO ratio, Figure 5.33.
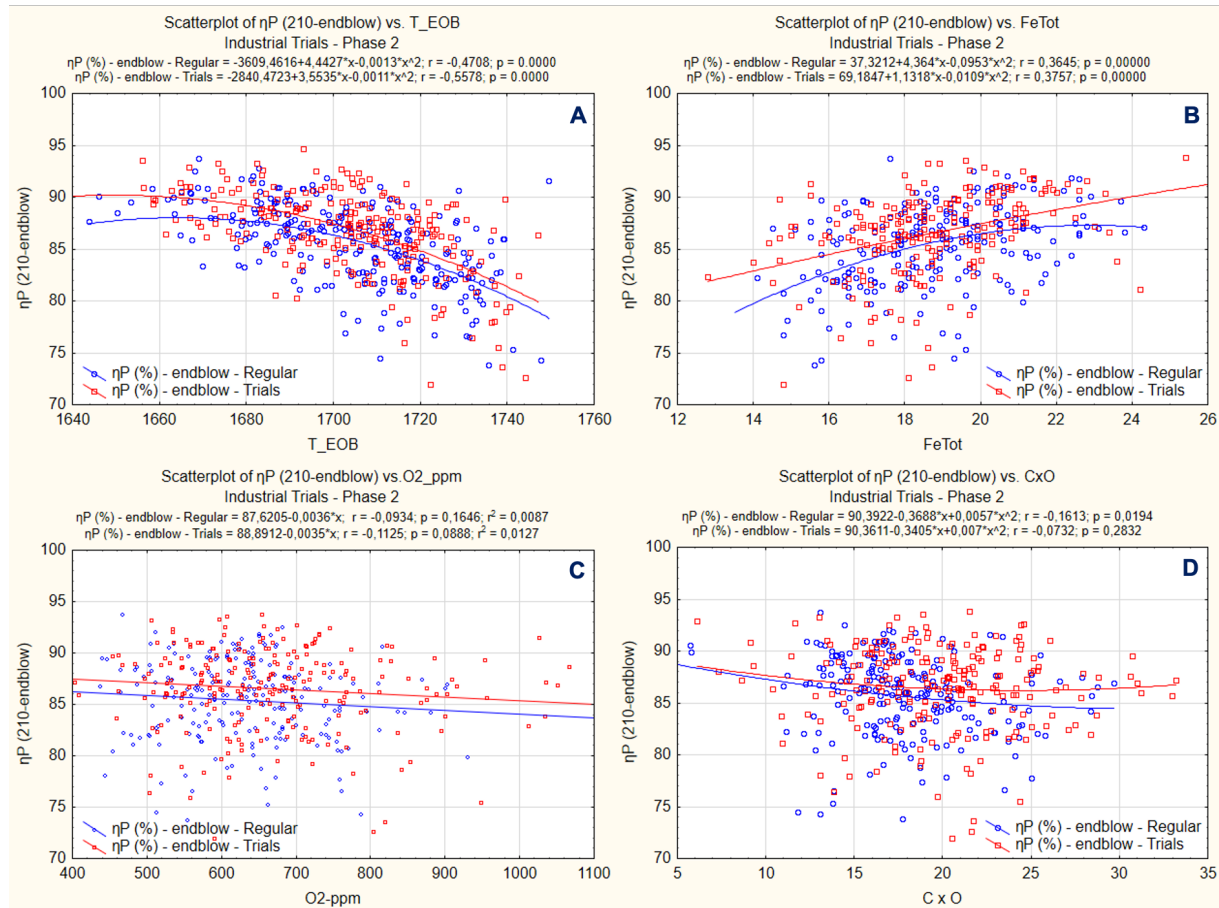
Figure 5.33: Scatterplots comparing the influence of the T_{EOB} ($°C$) (A), the slag Fe_T (%) (B), the oxygen activity O_2 (ppm) (C), and the CxO ratio (D) for the dephosphorization eficiency ($\eta_{P\,210}$).

In a similar method, better phosphorus partition (L_P) is observed in all the range of T_{EOB} ($°C$), Fe_T (%), O_2 (ppm) and CxO ratio, Figure 5.34.

It is not the intention of this work to explain the phosphorus partition L_P models,
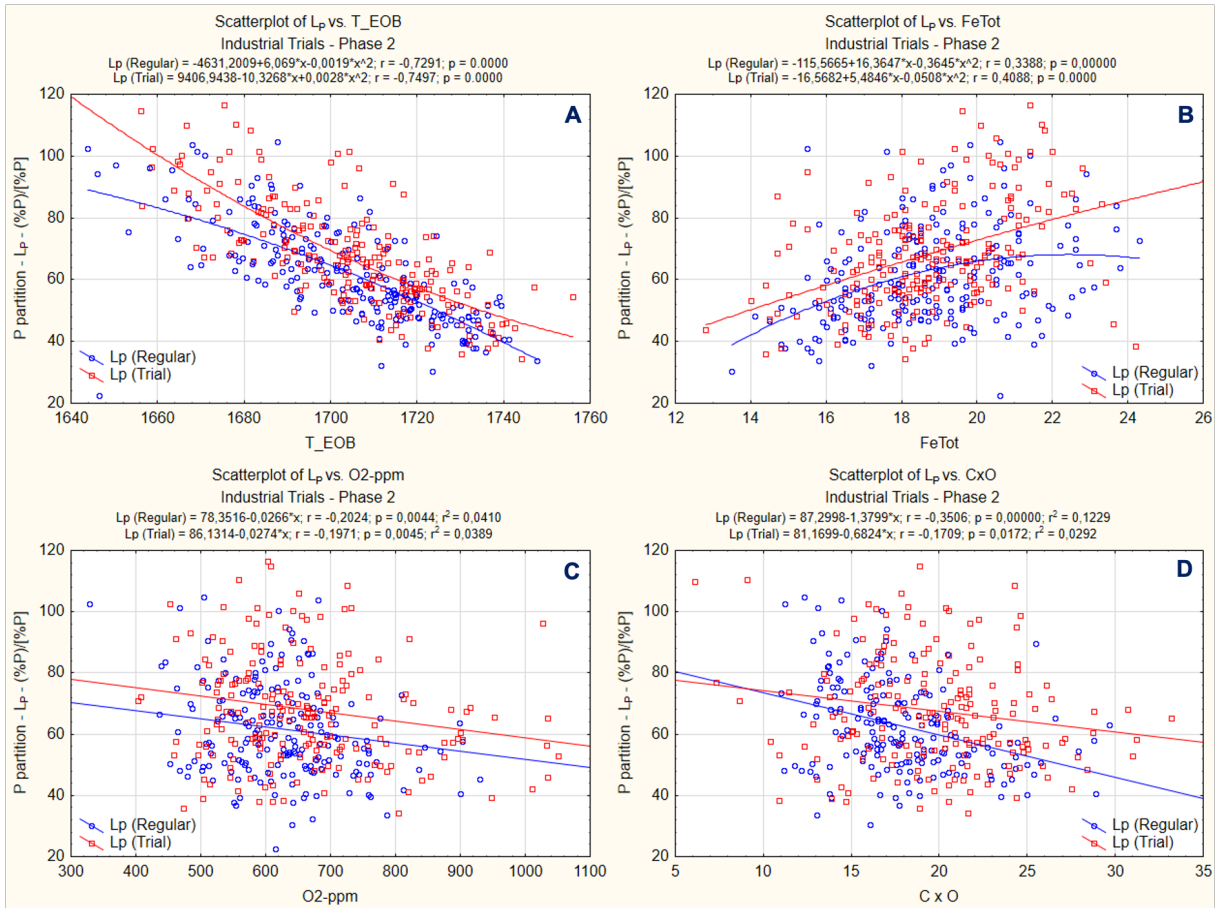
Figure 5.34: Scatterplots comparing the influence of the T_{EOB} ($°C$) (A), the slag Fe_T (%) (B), the oxygen activity O_2 (ppm) (C), and the CxO ratio (D) for the phosphorus partition (L_P).

but a suitable modelling approach may confirm and quantify the effect of the trials on the result of the phosphorus partition (L_P). Up to now, all variables have been isolated to evaluate the dephosphorization performance, aiming at a better comprehension on the effect of the proposed bottom stirring pattern on the dephosphorization results, a Machine Learning algorithm using the Python programming language was proposed to model the effects of each variable in the phosphorus partition (L_P). The LightGBM, a tree-based algorithm, was employed because of its computation power, delivering fast results with high accuracy results [211]. Despite the recommendation of its use for a larger volume of datasets, this algorithm was employed, and the results were checked through the normal probability evaluation, Figure 5.37. SHAP values library was employed to plot the data and explain the machine learning phosphorus partition (L_P) model [212], Figure 5.35.

According to the model output, the simplified SHAP variable importance graph, Figure 5.35 (left), lists the most significant variables in a decreasing rank. The top variables contribute more to the machine learning phosphorus partition (L_P) model than the bottom ones and consequently have an increased predictive influence. The detailed SHAP value plot also shows the negative and positive influence of the predictors between the
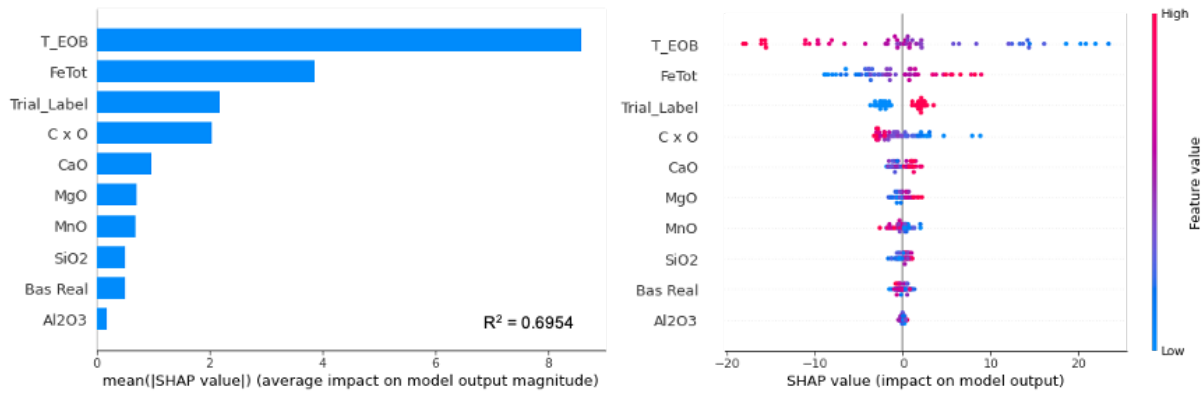
Figure 5.35: The simplified (left), and detailed (right) SHAP variable importance plot for the phosphorus partition (L_P) machine learning model.

target variable, Figure 5.35 (right). This plot contains all the dots in the train data and shows the feature importance of variables in descending order. The horizontal location shows whether the impact of one value is associated with a positive or negative prediction, and the colours show whether the effect of that variable is high (in red) or low (in blue) for the model [212].

Figure 5.36: Dataset test for the Phosphorus partition (L_P) model, calculated versus observed values.

The detailed SHAP value plot, Figure 5.35 (right), confirms the available literature of phosphorus partition (L_P) [213, 214, 215, 216, 217, 218, 210], it shows that a "lower" end of blow temperature (T_{EOB} (°C)) has the higher and "positive impact" on the phosphorus partition (L_P) model. The blue colour explains the "lower," and the "positive impact" is displayed on the X-axis. Similarly, higher slag oxidation ($Fe_T, \%$) contents have a positive correlation with the L_P model. The trial heats were ranked just after the Fe_T (%) results, and this surprising feature importance rank validates the previous discussions of this topic. The performed trials were labelled as one (1), and regular heats as zero (0), which confirms a positive correlation of the trial heats with the phosphorus partition (L_P) machine learning model. A lower CxO ratio shows a positive impact, and it indicates the performance of the bottom stirring. A higher CaO (%) and MgO (%) content in the slag also has a positive impact. Despite the literature review, the slag basicity (Bas Real), CaO/SiO_2, did not indicate a strong correlation, and it may be explained by the
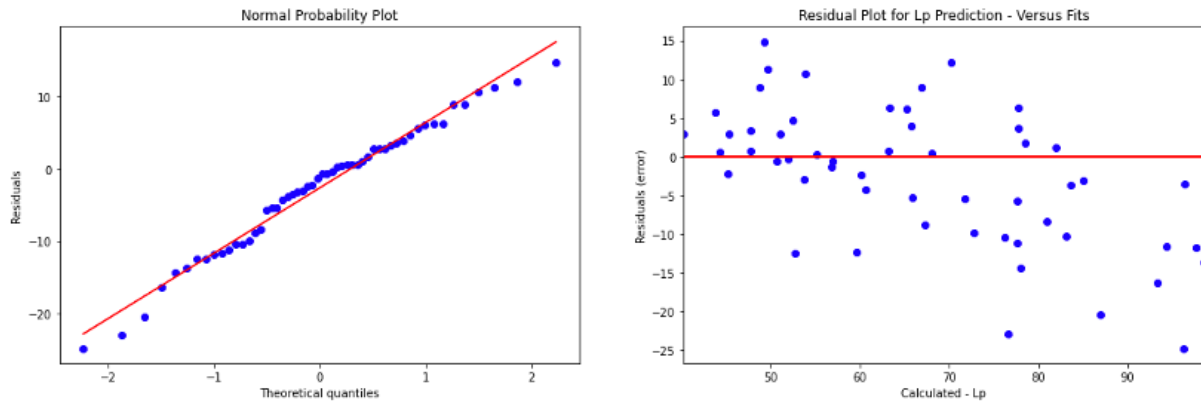
Figure 5.37: Normal probability evaluation for the phosphorus partition (L_P) model.

low range of basicity in the evaluated heats.

The dataset test, Figure 5.36, compares the measured phosphorus partition (L_P) values with the results calculated by the machine learning model. A good similarity between the measured and calculated values can be observed. The normal probability evaluation of the residual model errors shows the *normality* distribution of the data, Figure 5.37.

6 Conclusion

This thesis developed investigations to enhance the BOF process's metallurgical results through laboratory cold model investigations validated in the industrial environment, and more than 1750 trial heats were produced in a 330 t BOF.

This research introduced novel modified dimensionless numbers (Fr^*_{LaSiP}, Eo^*_{LaSiP}, We^*_{LaSiP}, Q^*, and E^*), the new parameters added in the equations delivered a unique solution to develop a complete BOF process similarity. According to the literature review, this study consolidated the numerous parameters connected to the BOF refining process. For the first time, a similarity study employed and associated the effects of the multi-nozzle supersonic lance, slag-phase and the bottom stirring gas parameters to design a new BOF cold model.

The methods applied in the laboratory measurements employed a mix of modified procedures available in the literature, and new techniques to evaluate the bath mixing time, mass transfer rate, jet penetration, decarburization area, sloping and projection rate for BOF cold modelling.

Regarding the mixing time measurements, the Luxmeter measurement method launched the improvement of the colourimetric method, and this new technique, firstly introduced in this research, was suitable for the global mixing time determination, especially for triphasic experiments. Nevertheless, it did not perform well to determine the local mixing time due to the equipment's sensitivity. On the other hand, the conductivimeter was more reliable to measure the local results for the biphasic trials; however, the oil phase's measurement remains a problem.

The performed mass transfer rate experiments employed the CO_2 desorption technique to measure the biphasic experiments. The benzoic acid titration was used to evaluate the triphasic trials, to simulate the steel-slag interaction. The first method contributed to verify the effects of the top blowing parameters in the mass transfer rate, which diverged from other investigations available in the literature. The second technique was fundamental to assess the influence of the bottom stirring patterns and arrangement. This work also introduced a new technique to measure jet penetration and the decarburization area through image analysis software.

The performed laboratory trials delivered essential pieces of evidence about the BOF process:

- Compared to all the other parameters evaluated, the lance flow rate was predom-

inant to determine the bath homogenization, and obtained higher decarburization areas for setups with higher lance flow rate and higher Bath Level Distance (BLD).

- The collisions caused by the jet of the top blowing lance, and the bubbles of the bottom stirring reduced the decarburization size, as well as the jet penetration.

- Higher lance flow rates exhibited more significant mass movement, supporting the kinetics of the reactions.

- Higher mass transfer coefficients were observed in experiments with higher decarburization area, validating the theory of more significant chemical reactions for larger impacted areas.

- Considering only the bottom stirring experiments, the mass transfer rate coefficients were proportional to the total bottom stirring flow rate. LaSiP 1 showed the best performance, a result explained by the smaller stagnant area and more significant reaction interface mixing. On the other hand, LaSiP 3 showed larger bath stagnation areas, delivering the smaller mass transfer coefficient.

- Regarding the bath mixing time, LaSiP 3 presented the best performance for bottom stirring experiments. Nevertheless, when the bottom stirring investigation combined the different top blowing setups, the top lance parameters played a crucial role to determine the mixing time. Moreover, the lowest values were found for higher bath level distances (BLD), and higher lance flow rate, respectively $0,45\ m$, and $160\ Nm^3.h^{-1}$. The different bottom stirring setups showed similar results for fixed top blowing parameters.

The industrial-scale experiments were fundamental to validate the laboratory trials, the first phase of experiments delivered important laboratory and process data for seven different bottom stirring configurations. Due to the lack of bottom stirring industrial data available in the literature, this work is another original contribution to science, and further studies as well.

Despite the influence of many other parameters and variables faced in the industrial environment, the performed trials delivered essential process data for a statistical and machine learning analysis. The evaluated parameters confirmed this thesis's primary objective; the improvement of the mixing time and the mass transfer rate between steel-slag phase due to a gradient of apparent density caused by the different bottom stirring flow zone.

7 Outlook

This thesis delivered a comprehensive understanding of the BOF cold modelling, including industrial-scale trials to validate the laboratory results. The outstanding literature review, fundamentals discussions and analysis, methods evaluation and results analysis delivered novel approaches to cope with the BOF cold modelling, and is an excellent opportunity for researchers to focus on future topics for investigations.

This thesis developed new measurement techniques and employed existing ones to successfully measure the experiments, such as mixing time, mass transfer rate between the steel and slag, jet depth, and decarburization area. Nevertheless, measuring mixing time for triphasic trials ($air - water - oil$) is still a challenge. The novel luxmeter technique showed the global mixing time but failed to determine the local mixing time. This experimental condition requires intensive investigations to develop a suitable measurement.

The new parameter introduced in the modified dimensionless numbers delivered a unique solution to develop a complete BOF process similarity, this research focused on simulating the current Ternium BR bottom stirring elements, maintaining the bottom design. These developments allowed further investigations considering a more comprehensive range of BOF process parameters, investigation and comparison of the results with the ones in the literature is recommended for different bottom stirring assembling and element types, as well as other top lance tip parameters and designs.

Regarding industrial practice, this thesis did not evaluate the long term results for the refractory performance. So, it is recommended to run one full campaign employing the suggested parameters, and compare the refractory laser measurements results for the trial campaign versus a regular campaign. The lining consumption may reduce, improving process stability and costs.

Bibliography

[1] F. Wallner and E. Fritz, "Fifty years of oxygen-converter steelmaking," *Revue de Métallurgie*, vol. 99, no. 10, pp. 825–837, oct 2002. [Online]. Available: http://www.metallurgical-research.org/10.1051/metal:2002143

[2] Voestalpine AG, "The story of the Linz-Donawitz process," *PPT*, p. 44, 2013. [Online]. Available: www.voestalpine.com.{%}0Awww.voestalpine.com

[3] J. K. Stone, "The origins of modern oxygen steelmaking," *Steel Times*, vol. September, pp. 328–330, 2000.

[4] W. Association, "World Steel in Figures 2019," Brussels, Belgium, Tech. Rep., 2019.

[5] D. Carvalho, "Additives dissolution model in the BOF converter process," Ph.D. dissertation, UFF, Volta Redonda, Brazil, 2015. [Online]. Available: https://sucupira.capes.gov.br/sucupira/public/consultas/coleta/trabalhoConclusao/viewTrabalhoConclusao.jsf?popup=true{&}id{_}trabalho=3348985

[6] World Steel Association, "Energy Use in the Iron and Steel Industry," *Energy Use in Steel Industry*, 2019. [Online]. Available: worldsteel.org

[7] J. Oda, K. Akimoto, and T. Tomoda, "Long-term global availability of steel scrap," *Resources, Conservation and Recycling*, vol. 81, pp. 81–91, dec 2013. [Online]. Available: http://dx.doi.org/10.1016/j.resconrec.2013.10.002https://linkinghub.elsevier.com/retrieve/pii/S0921344913001997

[8] C. Roth, M. Peter, M. Juhart, and K. Koch, "Cold model investigations of fluid flows and mixing within top and combined blowing in metallurgical processes," *Steel Research*, vol. 70, no. 12, pp. 502–507, 1999.

[9] D. Joao, "Otimização da injeção de gás inerte no convertedor MRP-L," Ph.D. dissertation, UFMG, 2002.

[10] AISE, Ed., *The making shaping and treating of steel.* Pittsburgh: The AISE Steel Foundation, 1998.

[11] R. Hüsken, P. Pottie, Z. Guoguang, and J. Cappel, "Overcoming the conflict between long BOF refractory lifetime and efficient bottom stirring: a case study at Meishan Steel in China," in *ABM Proceedings*, ABM, Ed. São Paulo: Editora Blucher, may

2014, pp. 2286–2297. [Online]. Available: http://abmproceedings.com.br/ptbr/article/overcoming-the-conflict-between-long-bof-refractory-lifetime-and-efficient-bottom-stirring-a-case-study-

[12] C. Oehler, M. Bock, M. Thiel, and J. Schoop, "Development of lance tips for the LD / BOF steelmaking process," in *European Oxygen Steelmaking Conference - EOSC*. Graz: ASMET, 2003, p. 14.

[13] M. Iguchi and O. J. Ilegbusi, *Modeling Multiphase Materials Processes*. New York, NY: Springer New York, 2011. [Online]. Available: http://link.springer.com/10.1007/978-1-4419-7479-2

[14] J. Szekely, *Fluid Flow Phenomena in Metals Processing*. Elsevier, 1979. [Online]. Available: https://linkinghub.elsevier.com/retrieve/pii/B9780126808407X50014https://www.elsevier.com/books/fluid-flow-phenomena-in-metals-processing/szekely/978-0-12-680840-7

[15] J. Szekely and O. J. Ilegbusi, *The Physical and Mathematical Modeling of Tundish Operations*, 1989.

[16] H. J. Odenthal, J. Kempken, J. Schlüter, and W. H. Emling, "Advantageous numerical simulation of the converter blowing process," *Iron and Steel Technology*, vol. 4, no. 11, pp. 71–89, 2007.

[17] H. Odenthal, U. Falkenreck, and J. Schlüter, "CFD Simulation of Multiphase Melt Flows in Steelmaking Converters," in *European Conference on Computational Fluid Dynamics*, no. ECCOMAS CFD, Delft, The Netherlands, 2006, pp. 1–21.

[18] H. J. Odenthal, P. Grygorov, M. Reifferscheid, and J. Schlüter, "Advanced blowing and stirring conditions in the BOF process," *AISTech - Iron and Steel Technology Conference Proceedings*, vol. 1, pp. 142–155, 2013.

[19] V. Seshadri, R. Tavares, C. Silva, and I. Silva, *Transport Phenomena: Fundamentals and aplications in Metallurgical and Materials Engineering*, São Paulo, 2011.

[20] L. Cao, Y. Wang, Q. Liu, and X. Feng, "Physical and mathematical modeling of multiphase flows in a converter," *ISIJ International*, vol. 58, no. 4, pp. 573–584, 2018.

[21] F. Oeters, *Metallurgie der Stahlherstellung*. Berlim: Verlag Stahleisen, 1989.

[22] K. Saito, K. Nakanishi, N. Misaki, K. Nakai, and M. Onishi, "Dephosphorization of Hot Metal with Injection of Lime Bearing Fluxes in a Ladle," *Tetsu-to-Hagane*, vol. 69, no. 15, pp. 1802–1809, 1983. [Online]. Available: https://www.jstage.jst.go.jp/article/tetsutohagane1955/69/15/69{_}15{_}1802/{_}article/-char/ja/

[23] H. ichiro Iso, Y. Ueda, Yoshida, S. Osada, S. Eto, and K. Arima, "Refining Control of Top- and Bottom-Blowing Converter By Manipulating Bottom-Blown Gas Flow Rate." *Transactions of the Iron and Steel Institute of Japan*, vol. 28, no. 5, pp. 372–381, 1988.

[24] Y. Higuchi and Y. Tago, "Effect of Top and Bottom Blowing Conditions on Metallurgical Characteristics in Converter," *Tetsu-to-Hagane*, vol. 86, no. 10, pp. 654–659, 2000. [Online]. Available: https://www.jstage.jst.go.jp/article/tetsutohagane1955/86/10/86{_}10{_}654/{_}article/-char/ja/

[25] T. Fabritius, P. Kupari, and J. Harkki, "Physical modelling of a sidewall-blowing converter," *Scandinavian Journal of Metallurgy*, vol. 30, no. 2, pp. 57–64, apr 2001. [Online]. Available: http://doi.wiley.com/10.1034/j.1600-0692.2001.300201.x

[26] Y. Kato and H. Okuda, "Reaction model for carbon, manganese, and oxygen in bottom blowing with mixed gas in final stage of steel refining in converter," *ISIJ International*, vol. 43, no. 11, pp. 1710–1714, 2003.

[27] M. Martín, M. Rendueles, and M. Díaz, "Global and local mixing determinations for steel converter analysis," *Chemical Engineering Science*, vol. 60, no. 21, pp. 5781–5791, 2005.

[28] J.-H. Wei, H.-L. Zhu, H.-B. Chi, and H.-J. Wang, "Physical modeling study on combined side and top blowing AOD refining process of stainless steel: Gas stirring and fluid flow characteristics in bath," *ISIJ International*, vol. 50, no. 1, pp. 17–25, 2010.

[29] A. K. Shukla, B. Deo, S. Millman, B. Snoeijer, A. Overbosch, and A. Kapilashrami, "An insight into the mechanism and kinetics of reactions in BOF steelmaking: Theory vs practice," *Steel Research International*, vol. 81, no. 11, pp. 940–948, 2010.

[30] D. Carvalho, B. Maia, C. Diniz, D. Souza, J. A. Guimarães, R. Salgado, and R. Tavares, "TBM tuyeres arrangements and flow - Comparison between BOF Ternium Brasil and cold model," in *Iron and Steel Technology*, vol. 15, no. 4, apr 2018, pp. 50–57.

[31] C. Chigwedu, J. Kempken, and W. Pluschkell, "A new approach for the dynamic simulation of the BOF process," *Stahl und Eisen*, vol. 126, no. 12, pp. 25–32, 2006. [Online]. Available: https://www.tib.eu/de/suchen/id/BLSE{%}3ARN200515879/A-new-approach-for-the-dynamic-simulation-of-the/

[32] B. Maia, J. Cappel, R. Tavares, and S. Balajee, "Practical approach of penetration index equations for use in BOF blowing pattern design," *AISTech - Iron and Steel Technology Conference Proceedings*, vol. 2018-May, pp. 1045–1061, 2018.

[33] S. Murakami, K. Okohira, M. Anabuki, and H. Nakagawa, "Improvement of the Top Blown Converter Process by the Suplementary Oxygen Bottom Blowing," in *4th Process Metallurgy Conference*, no. Mixed Gas Blowing Proceedings. Chicago: TMS-AIME, 1984, pp. 169–174.

[34] T. KATO, J. IMAI, and K. FUJIWARA, "Acceleration of Dephosphorization in Oxygen Converter under Agitation by Blowing of Gas." *Tetsu-to-Hagane*, vol. 49, no. 8, pp. 1065–1071, 1963.

[35] K. W. Lange, "Kombinierte Blas- und Spuelverfahren bei der Stahlerzeugung," *Stahl und Eisen*, vol. 101, no. 13-14, pp. 90–96, 1981. [Online]. Available: https://www.tib.eu/en/search/id/tema-archive{%}3ATEMAW81001384UDH/ Kombinierte-Blas-und-Spuelverfahren-bei-der-Stahlerzeugung/

[36] E. Hoeffken, H. D. Pflipsen, and R. A. Weber, "Das kombinierte Blasen in den Konverterstahlwerken der Thyssen AG," *Stahl und Eisen*, vol. 103, no. 4, pp. 155–158, 1983. [Online]. Available: https://www.tib.eu/en/search/id/tema-archive{%}3ATEMAW83000700UDH/ Das-kombinierte-Blasen-in-den-Konverterstahlwerken/

[37] L. Fiege, V. Schiel, H. Schroeer, L. Weber, and H. M. Delhey, "Einfluss des Bodenspuelens auf die metallurgischen Ergebnisse in den LD-Stahlweren der Krupp Stahl AG," *Stahl und Eisen*, vol. 103, no. 4, pp. 159–162, 1983.

[38] K. Chiara and S. Murakami, "Combined Blowing Process in Nippon Steel," in *Nippon Steel Technical Report.* Tokyo: Nippon Steel Corporation, 1984.

[39] P. Gugliermina, J. C. Grosjean, and A. Maubon, "Combined Blowing at Solmer," *4th Process Metallurgy Conference*, no. Mixed Gas Blowing Proceedings, pp. 183–187, 1984.

[40] M. Yaji, R. Asaho, A. Tamida, F. Sudo, and T. Imai, "Production of Ultra Low Carbon Steel By Combined Blowing," in *4th Process Metallurgy Conference*, no. Mixed Gas Blowing Proceedings. Chicago: TMS-AIME, 1984, pp. 137–143.

[41] S. Ito, K. Minoru, S. Koyama, H. Matsui, and H. Fujimoto, "On the new refining process by the top and bottom blowing converter," in *Iron and Steel Society*, 1982, pp. 123–130.

[42] H. Gruner, H. E. Wiemer, W. Fix, and K. Wunnenberg, "New Metallurgical Insight into BOF-Steelmaking and improved Process Control using Sublance Technique and Bottom Gas Stirring," in *4th Process Metallurgy Conference*, no. Mixed Gas Blowing Proceedings. Chicago: TMS-AIME, 1984, pp. 113–120.

[43] B. Attwood, R. G. Blossey, and L. Conner, "Metallurgical Benefits of BOF combined Blowing," in *4th Process Metallurgy Conference*, no. Mixed Gas Blowing Proceedings. Chicago: TMS-AIME, 1984, pp. 96–100.

[44] R. M. Wardrop, "LBE Operations at Gary Works," in *4th Process Metallurgy Conference*, no. Mixed Gas Blowing Proceedings. Chicago: TMS-AIME, 1984, pp. 107–112.

[45] P. Mink, G. Unen, and B. Deo, "Development in the bath agitation process at Hoogovens Ijmuiden," in *European Oxygen Steelmaking Conference - EOSC.* Dusseldorf: Published by VDEH, 1993, pp. 65–70.

[46] T. Kollman, C. Jandl, J. Schenk, H. Mizelli, W. Hofer, M. Hiebler, and A. Viertauer, "Comparison of Basic Oxygen Furnace Bottom Gas Purging Options," *RHI Bulletin*, no. 1/2012, pp. 8–15, 2012.

[47] D. N. Ghosh and R. P. Singh, "Cold model study of mixing time in hybrid process," *Transactions of the Iron and Steel Institute of Japan*, vol. 28, no. 8, pp. 659–662, 1988.

[48] H. S. Furtado, T. Bhattacharya, H. Hwang, and O. J. Kirmse, "Ultra-low phosphorus steel grade production in one batch BOF bottom blowing process," in *ABM Proceedings*, no. October. São Paulo: Editora Blucher, may 2014, pp. 2298–2308. [Online]. Available: http://abmproceedings.com.br/ptbr/article/ ultra-low-phosphorus-steel-grade-production-in-one-batch-bof-bottom-blowing-process

[49] A. C. P. Cardoso Filho, H. F. P. Gonçalves, C. A. R. Carneiro, and T. C. d. S. Araújo, "Estudo da técnica post-stirring e mecanismos envolvidos," *Tecnologia em Metalurgia e Materiais*, vol. 9, no. 1, pp. 16–21, 2012.

[50] H. F. P. Gonçalves, A. C. P. Cardoso Filho, C. A. R. Carneiro, and T. C. Silva Araujo, "Avaliação da técnica de post-stirring nos convertedores de 170 toneladas da Usiminas," in *42 Seminario de Aciaria Internacional*. Salvador, Brazil: ABM Brasil, 2011.

[51] M. Bock, J. Schoop, and C. Oehler, "The influence of blowing techniques, bottom stirring and lance design in the LD-process on slag formatio, the formation of lance and converter skulls and converter lining life," in *Seminario Fusao, Refino e Solidificacao de Metais*, no. 904/e, Vitoria, Brazil, 2000, pp. 1–7.

[52] M. Bock, "Theoretical considerations on the geometrical position of the converter bottom stirring plugs," *Seminario Fusao, Refino e Solidificacao de Metais*, no. 903/e, pp. 1–8, 1999.

[53] M. Haider, M. Kirschen, R. Ehrengruber, R. Ude, and K. Zettl, "BOF Process improvements by modern purging strategy and Technology," *Stahl und Eisen*, vol. 137, no. 9, pp. 39–44, 2017.

[54] K. Naito, S. Kitamura, and Y. Ogawa, "Effects of BOF top blowing and bottom stirring conditions on suppressing excessive oxidation," *Ironmaking & Steelmaking*, vol. 29, no. 3, pp. 208–213, jun 2002. [Online]. Available: https://doi.org/10.1179/ 030192302225005583http://www.tandfonline.com/doi/full/10.1179/030192302225005583

[55] Z. Guoguang, R. Hüsken, and J. Cappel, "Experience with long BOF campaign life and TBM bottom stirring technology at Meishan steel in China," *AISTech - Iron and Steel Technology Conference Proceedings*, no. November 2012, pp. 829–839, 2012.

[56] Z. Guoguang, Z. Kanglin, and G. Zhenhe, "Application and Maintenance of TBM Combined Blowing Technology in MeiShan Converter," in *European Oxygen Steelmaking Conference - EOSC*. Aachen - Germany: Stahl-Institut VDEh, 2006, pp. 130–135.

[57] G. SMS, "Converter Bottom Stirring," SMS, Hilchenbach, Tech. Rep., 2015. [Online]. Available: www.sms-siemag.com

[58] T. Kollmann, M. Kirschen, C. Jandl, and K. Zettl, "BOF Benefits of Gas Purging in BOF and eaf with a focus on material efficiency and CO2 emission reduction," in *57th International Colloquium on Refractories*, Aachen - Germany, 2014, pp. 76–80.

[59] S. Millman, M. Millman, A. Kapilashrami, M. Bramming, and D. Malmberg, "EUR 25005 - Imphos : Improving Phosphorus Refining," Luxemborg, Tech. Rep., 2011. [Online]. Available: https://op.europa.eu/s/nDWKhttps://op.europa.eu/s/nDWL

[60] Y. Lytvynyuk, J. Schenk, M. Hiebler, and A. Sormann, "Thermodynamic and kinetic model of the converter steelmaking process. Part 1: The description of the BOF model," *Steel Research International*, vol. 85, no. 4, pp. 537–543, 2014.

[61] F. M. Penz and J. Schenk, "A Review of Steel Scrap Melting in Molten Iron-Carbon Melts," *Steel Research International*, vol. 90, no. 8, pp. 1–20, 2019.

[62] N. Dogan, G. A. Brooks, and M. A. Rhamdhani, "Kinetics of flux dissolution in oxygen steelmaking," *ISIJ International*, vol. 49, no. 10, pp. 1474–1482, 2009.

[63] J. Szekely and N. J. Themelis, "Rate phenomena in process metallurgy," 1971.

[64] B. Maia, C. Diniz, G. Germano, R. Imagawa, R. Salgado, and R. Tavares, "Jet Penetration in Slag and Metal Into BOF Cold Model," in *Anais do Seminário de Aciaria, Fundição e Metalurgia de Não-Ferrosos*. São Paulo: Editora Blucher, sep 2017, pp. 46–56. [Online]. Available: http://abmproceedings.com.br/ptbr/article/jet-penetration-in-slag-and-metal-into-bof-cold-model

[65] A. Meidani, M. Isac, A. Richardson, A. Cameron, and R. Guthrie, "Modelling shrouded supersonic jets in metallurgical reactor vessels," *ISIJ International*, vol. 44, no. 10, pp. 1639–1645, 2004.

[66] M. Alam, "Modelling of Oxygen Injection and Splashing in Steelmaking," Ph.D. dissertation, Swinburne University of Technology, 2012.

[67] B. Maia and R. Tavares, "Modelamento Físico e Matemático do Escoamento de Fluidos nos Processos BOF e EOF," Ph.D. dissertation, UFMG, Be, 2013.

[68] A. Meidani, M. Isac, M. Kamal, and R. Guthrie, "Modelling Shrouded Supersonic Jets in Steelmaking Reactor Vessels," *ICS PRoceedings*, vol. 4, pp. 601–608, 2005.

[69] R. Flinn, R. Pehlke, D. Glass, and P. Hays, "Jet Penetration and Bath Circulation in the BOF," *Transactions of the Metallurgical Society of AIME*, vol. 239, no. November, pp. 1776–1791, 1967.

[70] S. K. Sharma, J. W. Hlinka, and D. W. Kern, "The Bath Circulation, Jet Penetration and High Temperature Reaction Zone in BOF Steelmaking," in *NOH-BOSC Proceedings*, Pittsburgh, 1977, pp. 187–197.

[71] A. R. Baker and V. Rajakumar, "Deoxidation of molten copper by an impinging jet of reducing gas," *Transactions of the Institution of Mining and Metallurgy, Section C: Mineral Processing and Extractive Metallurgy*, vol. 92, pp. 179–186, 1983.

[72] S. C. Koria and K. W. Lange, "Development of blowing practice for combined top blowing and bottom stirred processes," *International Iron Steel Congress*, vol. 6, pp. 219–224, 1986.

[73] C. British Steel, "Bath Stirring in Basic Oxygen Steelmaking by gas injection through basal tuyeres," Tech. Rep. EUR 10307 EN, 1986.

[74] M. P. Newby, "Experiments on the gas and fluid flow in a side-blown converter model," *Iron and Steel Institute*, vol. 162, no. August, pp. 452–456, 1949.

[75] R. D. Collins and H. Lubanska, "The depression of liquid surfaces by gas jets," *British Journal of Applied Physics*, vol. 5, no. 1, pp. 22–26, 1954.

[76] D. Glass and P. Hays, "The performance of supersonic nozzles as used in the oxygen conversion process." The University of Michigan, Tech. Rep. August, 1963. [Online]. Available: https://deepblue.lib.umich.edu/bitstream/handle/2027.42/5088/bac2716.0001.001.pdf?sequence=5

[77] F. R. Cheslak, J. A. Nicholls, and M. Sichel, "Cavities formed on liquid surfaces by impinging gaseous jets," *Journal of Fluid Mechanics*, vol. 36, no. 1, pp. 55–63, mar 1969. [Online]. Available: https://www.cambridge.org/core/product/identifier/S0022112069001509/type/journal{_}article

[78] D. Glass and E. Howard, "A study of supersonic nozzle design as applied to the oxygen conversion process," *University of Michigan*, vol. ERI 2409-1, no. November, 1955.

[79] D. Glass and P. Hays, "A design study of supersonic nozzles for the oxygen conversion process," *University of Michigan*, vol. ERI 2638-1, no. June, 1957.

[80] D. Glass and E. Howard, "An evaluation of the average impact pressure produced by a supersonic nozzle operating at conditions specified for the oxygen conversion process," *University of Michigan*, vol. ERI 2625-1, no. February, 1957.

[81] D. Glass and P. Hays, "An evaluation of supersonic nozzles used in the oxygen conversion process," *University of Michigan*, vol. ORA 04806-, no. January, 1962.

[82] E. Kurath, P. Hays, and D. Glass, "Final Report - Design Studies of Oxygen Nozzles," *University of Michigan*, no. ORA 05983, 1964.

[83] F. Rote, "Effect of Blowing Conditions on Dephosphorization in the BOF," *University of Michigan*, vol. D, no. IP-789, 1967.

[84] S. Inada, T. Watanabe, and K. Araki, "A Study of the Effects of CO2 Absorption in the NaOH Solution-CO2 Gas Jet Model," *Tetsu-to-Hagane*, vol. 62, no. 7, pp. 807–816, 1976. [Online]. Available: https://www.jstage.jst.go.jp/article/tetsutohagane1955/62/7/62{_}7{_}807/{_}article/-char/ja/

[85] S. C. Koria and K. W. Lange, "Production of drops in the initial stages of Basic Oxygen Steelmaking," in *International Iron Steel Congress*. Chicago: ASM and ISS-AIME, 1978, pp. 375–385.

[86] ——, "An experimental study on the behaviour of an underexpanded supersonic gas jet," *Archiv für das Eisenhüttenwesen*, vol. 55, no. 9, pp. 427–432, sep 1984. [Online]. Available: http://doi.wiley.com/10.1002/srin.198405369

[87] S. C. Koria, "Nozzle design in impinging jet steelmaking processes," *Steel Research*, vol. 59, no. 3, pp. 104–109, mar 1988. [Online]. Available: http://doi.wiley.com/10.1002/srin.198801614

[88] ——, "Dynamic variations of lance distance in impinging jet steelmaking practice," *Steel Research*, vol. 59, no. 6, pp. 257–262, jun 1988. [Online]. Available: http://doi.wiley.com/10.1002/srin.198801640

[89] S. C. Koria and K. W. Lange, "Breakup of iron-carbon drops by a high velocity oxygen gas jet," *Canadian Metallurgical Quarterly*, vol. 18, no. 2, pp. 131–143, 1979.

[90] ——, "Desintegration of iron-carbon drops by high-velocity gas jet," *Ironmaking & Steelmaking*, vol. 10, no. 4, pp. 160–168, 1983.

[91] ——, "A new approach to investigate the drop size distribution in basic oxygen steelmaking," *Metallurgical Transactions B*, vol. 15, no. 1, pp. 109–116, jan 1984. [Online]. Available: http://link.springer.com/10.1007/BF02661068

[92] ——, "Estimation of drop sizes in impinging jet steelmaking processes," *Ironmaking and Steelmaking*, vol. 13, no. 5, pp. 236–240, 1986.

[93] ——, "Correlation between drop size distribution or total drop mass and oxygen top blowing parameter," *International Iron Steel Congress*, vol. 6, pp. 353–356, 1986.

[94] ——, "Penetrability of impinging gas jets in molten steel bath," *Steel Research*, vol. 58, no. 9, pp. 421–426, sep 1987. [Online]. Available: http://doi.wiley.com/10.1002/srin.198700241

[95] T. Labus and J. Aydelott, "Gas-jet Impingement Normal to a Liquid Surface," in *NASA*, vol. TN D-6368, no. September, 1971, pp. 1–16.

[96] H. Ishikawa, S. Mizoguchi, and K. Segawa, "A Model Study on Jet Penetration and Slopping in the LD Converter," *Tetsu-to-Hagane*, vol. 58, no. 1, pp. 76–84, 1972. [Online].

Available: https://www.jstage.jst.go.jp/article/tetsutohagane1955/58/1/58{_}1{_}76/{_}article/-char/ja/

[97] S. Paul and D. N. Ghosh, "Model study of mixing and mass transfer rates of slag-metal in top and bottom blown converters," *Metallurgical Transactions B*, vol. 17, no. 3, pp. 461–469, 1986.

[98] Q. He, "Fluid dynamics and droplet generation in the BOF steelmaking process," *University of Wollongong*, no. Doctor of Philosophy, 1990. [Online]. Available: http://ro.uow.edu.au/theses/1497

[99] Q. L. He and N. Standish, "A model study of droplet generation in the BOF steelmaking_Translation," *ISIJ International*, vol. 30, no. 4, pp. 305–309, 1990. [Online]. Available: http://joi.jlc.jst.go.jp/JST.Journalarchive/isijinternational1989/30.305?from=CrossRef

[100] M. J. Luomala, T. M. J. Fabritius, E. O. Virtanen, T. P. Siivola, and J. J. Härkki, "Splashing and spitting behaviour in the combined blown steelmaking converter," *ISIJ International*, vol. 42, no. 9, pp. 944–949, 2002.

[101] T. Kumagai and M. Iguchi, "Instability Phenomena at Bath Surface Induced by Top Lance Gas Injection," *ISIJ International*, vol. 41, no. Suppl, pp. S52–S55, 2001. [Online]. Available: http://joi.jlc.jst.go.jp/JST.Journalarchive/isijinternational1989/41.Suppl{_}S52?from=CrossRef

[102] T. Kumagai, M. Iguchi, T. Uemura, and N. Yonehara, "Gas-Liquid Mass Transfer in Simulated Turbulent Wake Flow." *ISIJ International*, vol. 42, no. 1, pp. 112–114, 2002. [Online]. Available: http://joi.jlc.jst.go.jp/JST.Journalarchive/isijinternational1989/42.112?from=CrossRef

[103] A. Nordquist, "A physical modeling study of top blowing with focus on the penetration region," in *KTH Royal Institute of Technology*. Sweden: Licenciate Thesis, 2005.

[104] A. Nordquist, N. Kumbhat, L. Jonsson, and P. Jönsson, "The effect of nozzle diameter, lance height and flow rate on penetration depth in a top-blown water model," *Steel Research International*, vol. 77, no. 2, pp. 82–90, 2006.

[105] M. Evestedt and A. Medvedev, "Cavity Shape Dynamical Modelling and Estimation in a Water Model of the Steel Converter Process," *Journal of the Japanese Society for Experimental Mechanics*, vol. 7, no. Special_Issue, pp. s93–s98, 2007.

[106] A. Chatterjee and A. V. Bradshaw, "Break-up of a liquid surface by an impinging gas jet," *Journal of The Iron and Steel Institute*, vol. March, pp. 179–187, 1972.

[107] A. Chatterjee, "On some aspects of supersonic jets of interest in LD steelmaking - Part 1: Jet Design and Characteristics," in *Iron and Steel International*, vol. XP00200136. GUILDFORD GB: IPC Science and Technology Press., 1972, pp. 627–634.

[108] ——, "On some aspects of supersonic jets of interest in LD steelmaking - Part 2: Interaction of a supersonic jet with a steelmaking bath," *Iron and Steel International*, vol. XP00200136, pp. 38–40, 1973.

[109] U. S. Shrivastava, B. N. Mukhopadhyay, and S. L. Malhotra, "Interaction of gas jets with liquid surface: onset of splashing," *Indian Journal Technololgy*, vol. 14, no. 1, pp. 13–17, 1976.

[110] C. Lee, J. Neilson, and A. Gilchrist, "Correlation of the decay characteristics of jets from multi-nozzle oxygen lances with the performance of the charge in steel converters," *Iron and Steel International*, vol. 50, no. 3, pp. 175–184, 1977.

[111] M. Ek and D. Sichen, "Study of penetration depth and droplet behavior in the case of a gas jet impinging on the surface of molten metal using liquid Ga-In-Sn," *Steel Research International*, vol. 83, no. 7, pp. 678–685, jul 2012. [Online]. Available: http://doi.wiley.com/10.1002/srin.201100336

[112] M. Asai, H. Nijo, and K. Ito, "Simulation of the impingement of a liquid jet on a molten iron bath by using a particle method," *ISIJ International*, vol. 49, no. 2, pp. 178–181, 2009.

[113] N. Asahara, K.-i. Naito, I. Kitagawa, M. Matsuo, M. Kumakura, and M. Iwasaki, "Fundamental Study on Interaction between Top Blown Jet and Liquid Bath," *Steel Research International*, vol. 82, no. 5, pp. 587–594, may 2011. [Online]. Available: http://doi.wiley.com/10.1002/srin.201100041

[114] G. Brooks, S. Sabah, B. Rout, and Z. Li, "Splash generation in oxygen steelmaking: What is known?" *AISTech - Iron and Steel Technology Conference Proceedings*, vol. 2, pp. 1253–1260, 2017.

[115] X. Zhou, M. Ersson, L. Zhong, J. Yu, and P. Jönsson, "Mathematical and Physical Simulation of a Top Blown Converter," *Steel Research International*, vol. 85, no. 2, pp. 273–281, feb 2014. [Online]. Available: http://doi.wiley.com/10.1002/srin.201300310

[116] J. Solórzano-López, R. Zenit, and M. Ramírez-Argáez, "Mathematical and physical simulation of the interaction between a gas jet and a liquid free surface," *Applied Mathematical Modelling*, vol. 35, no. 10, pp. 4991–5005, oct 2011. [Online]. Available: https://linkinghub.elsevier.com/retrieve/pii/S0307904X11002290

[117] M. K. Mondal and K. Logachander, "Modelling study of jet- metal interaction in LD process," *International Journal of Research in Engineering and Technology*, vol. 02, no. 12, pp. 451–456, dec 2013. [Online]. Available: https://ijret.org/volumes/2013v02/i12/IJRET20130212076.pdf

[118] O. Olivares, A. Elias, R. Sánchez, M. Díaz, and R. Morales, "Physical and mathematical models of gas-liquid fluid dynamics in LD converters," *Steel Research*, vol. 73, no. 2, pp. 44–51, 2002.

[119] M. Diaz-Cruz, R. D. Morales, O. Olivares, and A. Elias, "Characteristic of mixing time and splashing in the basic oxygen steel-making processes," *ICAMMP-2002*, 2002.

[120] L. L. Cao, Q. Liu, Z. Wang, and N. Li, "Interaction behaviour between top blown jet and molten steel during BOF steelmaking process," *Ironmaking and Steelmaking*, vol. 45, no. 3, pp. 239–248, mar 2018. [Online]. Available: https://www.tandfonline.com/doi/full/10.1080/03019233.2016.1255373

[121] S. Sabah and G. Brooks, "Study of cavity modes in BOF by analysis of sound," *Ironmaking and Steelmaking*, vol. 43, no. 6, pp. 473–480, 2016.

[122] ——, "Splash Distribution in Oxygen Steelmaking," *Metallurgical and Materials Transactions B: Process Metallurgy and Materials Processing Science*, vol. 46, no. 2, pp. 863–872, 2014.

[123] B. Maia, "Efeito da configuração do bico da lança na interação janto-banho metálico em convertedor LD," Ph.D. dissertation, UFMG, 2007. [Online]. Available: http://www.bibliotecadigital.ufmg.br/dspace/bitstream/handle/1843/MAPO-7R5MTZ/breno{_}totti{_}maia.pdf?sequence=1

[124] B. Maia, R. Imagawa, A. C. Petrucelli, and R. Tavares, "Effect of blow parameters in the jet penetration by physical model of BOF converter," *Journal of Materials Research and Technology*, vol. 3, no. 3, pp. 244–256, jul 2014. [Online]. Available: http://dx.doi.org/10.1016/j.jmrt.2014.06.010https://linkinghub.elsevier.com/retrieve/pii/S223878541400057X

[125] B. Maia, R. Imagawa, and R. Tavares, "Estudo do comportamento do banho no convertedor LD com sopro combinado," in *Anais do Seminário de Aciaria, Fundição e Metalurgia de Não-Ferrosos*. São Paulo: Editora Blucher, sep 2017, pp. 1–13. [Online]. Available: http://abmproceedings.com.br/ptbr/article/estudo-do-comportamento-do-banho-no-convertedor-ld-com-sopro-combinado

[126] L. Zhong, Y. Zhu, M. Jiang, Z. Qu, Y. Za, and X. Bao, "Cold modelling of slag splashing in LD furnace by oxygen lance with twisted nozzle tip," *Steel Research International*, vol. 76, no. 9, pp. 611–615, 2005.

[127] M. J. Luomala, T. M. Fabritius, E. O. Virtanen, T. P. Siivola, T. L. Fabritius, H. Tenkku, and J. J. Härkki, "Physical model study of selective slag splashing in the BOF," *ISIJ International*, vol. 42, no. 11, pp. 1219–1224, 2002.

[128] K. Nakanishi, Y. Kato, T. Nozaki, and T. Emi, "Cold Model Study on the Mixing Rates of Slag and Metal Bath in Q-BOP," *Tetsu-To-Hagane/Journal of the Iron and Steel Institute of Japan*, vol. 66, no. 9, pp. 1307–1316, 1980.

[129] T. Kai, K. Okohira, M. Higuchi, and M. Hirai, "Cold Model Study of Characteristics in Ld Converter With Bottom Blowing." *Tetsu-To-Hagane/Journal of the Iron and Steel Institute of Japan*, vol. 69, no. 2, pp. 228–237, 1983.

[130] N. Kyoji, S. Kenji, N. Tsutomu, K. Yoshiei, S. Ken ichiro, and E. Toshihiko, "Physical and metallurgical characteristics of combined blowing processes," in *Steelmaking Conference Proceedings*. Japan: Iron & Steel Soc of AIME, 1982, pp. 101–108.

[131] S. C. Koria and K. W. Lange, "Effect of Melting scrap on the mixing – time of bottom gas stirred melts," in *6th Japan-Germany seminar*, Tokyo, 1984, pp. 91–101.

[132] ——, "Mixing-time correlation in top gas stirred melts," *Archiv für das Eisenhüttenwesen*, vol. 55, no. 3, pp. 97–100, mar 1984. [Online]. Available: http://doi.wiley.com/10.1002/srin.198405317

[133] S. C. Koria and A. George, "Selection of bottom injection parameters in combined blown steelmaking," *Ironmaking and Steelmaking*, vol. 15, no. 3, pp. 127–133, 1988.

[134] S. C. Koria, "Studies of the Bath Mixing Intensity in Converter Steelmaking Processes," *Canadian Metallurgical Quarterly*, vol. 31, no. 2, pp. 105–112, apr 1992. [Online]. Available: http://openurl.ingenta.com/content/xref?genre=article{&}issn=0008-4433{&}volume=31{&}issue=2{&}spage=105

[135] S. C. Koria and S. Pal, "Experimental study of the effect of gas injection parameters on the bath mixing intensity induced during steelmaking," *Steel Research*, vol. 62, no. 2, pp. 47–53, feb 1991. [Online]. Available: http://doi.wiley.com/10.1002/srin.199101249

[136] M. G. Frohberg, F. Gerlach, and G. Handschuh, "Investigations of drop-size-distribution and mass transfer in gas-stirred liquid-liquid systems," *Steel Research*, vol. 61, no. 4, pp. 151–156, apr 1990. [Online]. Available: http://doi.wiley.com/10.1002/srin.199000322

[137] H. Schlarb and M. G. Frohberg, "Experiments on the mass transfer between two immiscible phases by a top and bottom blown converter model," *Steel Research*, vol. 56, no. 1, pp. 15–18, jan 1985. [Online]. Available: http://doi.wiley.com/10.1002/srin.198500590

[138] F. Gerlach and M. G. Frohberg, "Mass transfer in a bottom blowing cold model converter," *Steel Research*, vol. 64, no. 1, pp. 7–14, jan 1993. [Online]. Available: http://doi.wiley.com/10.1002/srin.199300975

[139] M. Martín, M. Rendueles, and M. Díaz, "Emulsion Analysis in a Gas/Liquid/Liquid Reactor With Top Blowing," *The Canadian Journal of Chemical Engineering*, vol. 82, no. 2, pp. 249–255, may 2004. [Online]. Available: http://doi.wiley.com/10.1002/cjce.5450820206

[140] W. Wu, L.-b. Yang, C.-j. Zheng, and L. Liu, "Cold Simulation of Oxygen Transfer Rate in BOF," *Journal of Iron and Steel Research International*, vol. 17, no. 9, pp. 7–13, sep 2010. [Online]. Available: http://dx.doi.org/10.1016/S1006-706X(10)60134-3http://link.springer.com/10.1016/S1006-706X(10)60134-3

[141] C. Roth, M. Peter, M. Schindler, and K. Koch, "Cold model investigations into the effects of bottom blowing in metallurgical reactors," *Steel Research*, vol. 66, no. 8, pp. 325–330, aug 1995. [Online]. Available: http://doi.wiley.com/10.1002/srin.199501132

[142] M. J. Luomala, E. O. Virtanen, P. T. Mure, T. P. Siivola, T. M. Fabritius, J. J. Härkki, T. Silvola, T. M. Fabritius, and J. J. Härkki, "A novel approach in the estimation of splashing in the BOF," *Steel Research*, vol. 73, no. 1, pp. 9–14, jan 2002. [Online]. Available: http://doi.wiley.com/10.1002/srin.200200166

[143] M. J. Luomala, T. M. Fabritius, and J. J. Härkki, "The effect of bottom nozzle configuration on the bath behaviour in the BOF," *ISIJ International*, vol. 44, no. 5, pp. 809–816, 2004.

[144] M. Martín, M. Díaz, M. Martin, and M. Diaz, "Gas-liquid and gas-liquid-liquid reactors with top and bottom blowing: I. Fluid dynamic regimes," *Chemical Engineering Communications*, vol. 189, no. 2, pp. 543–570, apr 2002. [Online]. Available: https://www.tandfonline.com/doi/full/10.1080/00986440212088

[145] S. K. Ajmani and A. Chatterjee, "Cold model studies of mixing and mass transfer in steelmaking vessels," *Ironmaking and Steelmaking*, vol. 32, no. 6, pp. 515–527, 2005.

[146] S. K. Choudhary and S. K. Ajmani, "Evaluation of bottom stirring system in BOF steelmaking vessel using cold model study and thermodynamic analysis," *ISIJ International*, vol. 46, no. 8, pp. 1171–1176, 2006.

[147] V. Singh, J. Kumar, C. Bhanu, S. K. Ajmani, and S. K. Dash, "Optimisation of the bottom tuyeres configuration for the BOF vessel using physical and mathematical modelling," *ISIJ International*, vol. 47, no. 11, pp. 1605–1612, 2007.

[148] J.-H. Wei, H.-L. Zhu, S.-L. Yan, X.-C. Wang, J.-C. Ma, G.-M. Shi, Q.-Y. Jiang, H.-B. Chi, L.-B. Che, and K. Zhang, "Preliminary Investigation of Fluid Mixing Characteristics during Side and Top Combined Blowing AOD Refining Process of Stainless Steel," *Steel Research International*, vol. 76, no. 5, pp. 362–371, may 2005. [Online]. Available: http://doi.wiley.com/10.1002/srin.200506023

[149] J.-H. Wei and H.-Y. Zuo, "Study on Mass Transfer Characteristics in an AOD Converter Bath under Conditions of Combined Side and Top Blowing," *Steel Research International*, vol. 78, no. 12, pp. 863–875, dec 2007. [Online]. Available: http://doi.wiley.com/10.1002/srin.200706299

[150] R. Bruckhaus and H. Lachmund, "Stirring strategies to meet the highest metallurgical requirements in the BOF process," *Iron and Steel Technology*, vol. 4, no. 11, pp. 44–50, 2007.

[151] H. Lachmund, R. Bruckhaus, V. Fiedler, and Y. Xie, "Optimisation of the BOF process after replacement of vessels with a different geometry," *Stahl und Eisen*, vol. 123, no. 11, pp. 53–58, 2003.

[152] D. Oymo and R. I. Guthrie, "Mixing Times in Combination Blowing Processes," in *4th Process Metallurgy Conference*, no. Mixed Gas Blowing Proceedings. Chicago: TMS-AIME, 1984, pp. 45–52.

[153] X. Zhou, M. Ersson, L. Zhong, and P. Jönsson, "Optimization of combined blown converter process," *ISIJ International*, vol. 54, no. 10, pp. 2255–2262, 2014.

[154] X. Zhou, M. Ersson, L. Zhong, and P. G. Jönsson, "Numerical and Physical Simulations of a Combined Top-Bottom-Side Blown Converter," *Steel Research International*, vol. 86, no. 11, pp. 1328–1338, nov 2015. [Online]. Available: http://doi.wiley.com/10.1002/srin.201400376

[155] X. Zhou, "Mathematical and Physical Simulations of BOF Converters," Ph.D. dissertation, KTH Royal Institute of Technology, 2015.

[156] D. Carvalho, J. Schenk, R. Tavares, B. Maia, D. Silveira, M. Ribeiro, and R. Salgado, "Evaluation of mixing and mass transfer at ternium Brazil's BOF through cold model experiments," *AISTech - Iron and Steel Technology Conference Proceedings*, vol. 2019-May, no. May, pp. 979–986, 2019.

[157] D. Carvalho, H. Castro, L. Demuner, M. Viana, R. Formage, T. Schulz, and P. Wojnar, "BOF blowing process challenges for high rate of iron ore pellet addition - Process development and results at tkCSA," in *AISTech - Iron and Steel Technology Conference Proceedings*, vol. 2, 2017.

[158] B. Maia, C. Diniz, G. Germano, R. Salgado, and R. Tavares, "Determinação Da Massa Movimentada Em Modelo a Frio Do Banho Metal Escoria Por Sopro Supersônico De Bicos Multifuros," in *Anais do Seminário de Aciaria, Fundição e Metalurgia de Não-Ferrosos*. São Paulo: Editora Blucher, sep 2017, pp. 86–100. [Online]. Available: http://abmproceedings.com.br/ptbr/article/determinacao-da-massa-movimentada-em-modelo-a-frio-do-banho-metal-escoria-por-sopro-supersonico-

[159] R. M. Figueira and J. Szekely, "Turbulent Fluid Flow Phenomena in a Water Model of an AOD System," *Metallurgical Transactions B*, vol. 16, no. 1, pp. 67–75, 1985.

[160] T. Stišovic and K. Koch, "Bottom blowing investigations on a cold model reactor to optimise mixing behaviour in metallurgical processes," *Steel Research*, vol. 73, no. 9, pp. 373–377, sep 2002. [Online]. Available: http://doi.wiley.com/10.1002/srin.200200002

[161] V. Singh, S. N. Lenka, S. K. Ajmani, C. Bhanu, and S. Pathak, "A novel bottom stirring scheme to improve BOF performance through mixing and mass transfer modelling," *ISIJ International*, vol. 49, no. 12, pp. 1889–1894, 2009.

[162] A. Quiyoom, R. Golani, V. Singh, and V. V. Buwa, "Effect of differential flow schemes on gas-liquid flow and liquid phase mixing in a Basic Oxygen Furnace,"

Chemical Engineering Science, vol. 170, pp. 777–789, 2017. [Online]. Available: http://dx.doi.org/10.1016/j.ces.2017.03.010

[163] D. Mazumdar and J. W. Evans, *Modeling Of Steelmaking Processes*, 2010.

[164] G. Ascanio, "Mixing time in stirred vessels: A review of experimental techniques," *Chinese Journal of Chemical Engineering*, vol. 23, no. 7, pp. 1065–1076, 2015. [Online]. Available: http://dx.doi.org/10.1016/j.cjche.2014.10.022

[165] L. A. Melton, C. W. Lipp, R. W. Spradling, and K. A. Paulson, "DISMT - Determination of mixing time through color changes," *Chem. Eng. Comm.*, vol. 189, no. 3, pp. 322–338, 2002.

[166] G. Ascanio, S. Foucault, and P. Tanguy, "Time-Periodic Mixing of Shear-thinning Fluids," *Chemical Engineering Research and Design*, vol. 82, no. 9, pp. 1199–1203, sep 2004. [Online]. Available: https://linkinghub.elsevier.com/retrieve/pii/S0263876204726076

[167] T. Y. Kuo and J. C. Kuo, "Determination of mixing time in a ladle-refining process using optical image processing," *ISIJ International*, vol. 51, no. 10, pp. 1597–1600, 2011.

[168] C. Wuppermann, N. Giesselmann, A. Rückert, H. Pfeifer, H. J. Odenthal, and E. Hovestädt, "A novel approach to determine the mixing time in a water model of an AOD converter," *ISIJ International*, vol. 52, no. 10, pp. 1817–1823, 2012.

[169] A. Kumar, M. Malathi, K. M. Godiwalla, E. Z. Chacko, S. K. Ajmani, and S. Ranganathan, "Cold model study of submerged peripheral gas bubbling from a cylindrical dispenser," *ISIJ International*, vol. 54, no. 10, pp. 2239–2247, 2014.

[170] A. Rosseburg, J. Fitschen, J. Wutz, T. Wucherpfennig, and M. Schlüter, "Hydrodynamic inhomogeneities in large scale stirred tanks – Influence on mixing time," *Chemical Engineering Science*, vol. 188, pp. 208–220, 2018. [Online]. Available: https://doi.org/10.1016/j.ces.2018.05.008

[171] D. B. Holmes, R. M. Voncken, and J. A. Dekker, "Fluid flow in turbine-stirred, baffled tanks-I. Circulation time," *Chemical Engineering Science*, vol. 19, no. 3, pp. 201–208, 1964.

[172] C. Chen, Q. Rui, and G. Cheng, "Effect of salt tracer amount on the mixing time measurement in a hydrodynamic model of gas-stirred ladle system," *Steel Research International*, vol. 84, no. 9, pp. 900–907, 2013.

[173] S. Inada and T. Watanabe, "The Model Experiment on the Reaction between the Liquid and the Swarms of Gas Bubbles by NaOH-CO2 System," *Tetsu-to-Hagane*, 1976.

[174] N. Bessho, S. Taniguchi, and A. Kikuchi, "Mass Transfer Between Gas and Liquid in a Gas-Stirred Vessel." *Tetsu-To-Hagane/Journal of the Iron and Steel Institute of Japan*, vol. 71, no. 14, pp. 1623–1630, 1985.

[175] J.-H. Zong, H.-K. Park, and J.-K. Yoon, "The Cold Model Study on the Decarburization Rate in Oxygen Steelmaking Processes by C02/KOH System," *ISIJ International*, vol. 30, no. 9, pp. 748–755, 1990.

[176] Y. Kawabe, M. A. Uddin, Y. Kato, M. O. Seok, and S. B. Lee, "Correlation between liquid/liquid and gas/liquid mass transfers in a top/bottom blowing converter," *ISIJ International*, vol. 57, no. 2, pp. 296–303, 2017.

[177] M. Martín, M. Rendueles, and M. Díaz, "Steel-slag mass transfer in steel converter, bottom and top/bottom combined blowing through cold model experiments," *Chemical Engineering Research and Design*, vol. 83, no. 9 A, pp. 1076–1084, 2005.

[178] J. H. Zong and J. K. Yoon, "Theoretical interpretation of the decarburization mechanism in convective oxygen steelmaking," *Metallurgical Transactions B*, vol. 21, no. 1, pp. 49–57, 1990.

[179] Q. Li, M. Li, S. Kuang, and Z. Zou, "Numerical Simulation of the Interaction Between Supersonic Oxygen Jets and Molten Slag–Metal Bath in Steelmaking BOF Process," *Metallurgical and Materials Transactions B*, vol. 46, no. 3, pp. 1494–1509, jun 2015. [Online]. Available: http://link.springer.com/10.1007/s11663-015-0292-3

[180] R. B. Banks and D. V. Chandrasekhara, "Experimental investigation of the penetration of a high-velocity gas jet through a liquid surface," *Journal of Fluid Mechanics*, vol. 15, no. 1, pp. 13–34, jan 1963. [Online]. Available: https://www.cambridge.org/core/product/identifier/S0022112063000021/type/journal{_}article

[181] K. I. Naito, N. Asahara, A. Kaizawa, Y. Ogawa, I. Kitagawa, T. Inomoto, N. Sasaki, and M. Matsuo, "Behavior of top-blowing lance jets in BOF," *Nippon Steel Technical Report*, no. 104, pp. 33–41, 2013.

[182] G. Wei, R. Zhu, T. Cheng, K. Dong, L. Yang, and X. Wu, "Study on the Impact Characteristics of Coherent Supersonic Jet and Conventional Supersonic Jet in EAF Steelmaking Process," *Metallurgical and Materials Transactions B: Process Metallurgy and Materials Processing Science*, vol. 49, no. 1, pp. 361–374, 2018.

[183] M. S. Lee, S. L. O'Rourke, and N. A. Molloy, "Oscillatory flow in the steelmaking vessel," *Scandinavian Journal of Metallurgy*, vol. 32, no. 5, pp. 281–288, 2003.

[184] J. Shi, X. Luo, J. Li, and J. Jiang, "Investigation on penetration model of shaped charge jet in water," *Modern Physics Letters B*, vol. 30, no. 2, pp. 1–15, 2016.

[185] S. Kobayashi, A. Hatono, K. Katohgi, A. Kuriyama, and K. Ichihara, "Prediction and Control of Slag Slopping in BOF Using Microwave Gauge," *IFAC Proceedings Series*, vol. 16, no. 15, pp. 297–301, 1984. [Online]. Available: http://dx.doi.org/10.1016/S1474-6670(17)64281-2

[186] B. Deo, A. Overbosch, B. Snoeijer, D. Das, and K. Srinivas, "Control of slag formation, foaming, slopping, and chaos in BOF," *Transactions of the Indian Institute of Metals*, vol. 66, no. 5-6, pp. 543–554, 2013.

[187] M. Belahouel and A. Abdenbi, "Numerical simulation of the interaction of a jet of gas with a liquid surface," *International Review of Mechanical Engineering*, vol. 8, no. 5, pp. 857–863, 2014.

[188] S. Ramani and A. K. Lahiri, "Determination of mixing time in BOF process by a cold model study," *Steel Research*, vol. 59, no. 3, pp. 93–95, mar 1988. [Online]. Available: http://doi.wiley.com/10.1002/srin.198801612

[189] R. B. Banks and D. V. Chandrasekhara, "Experimental investigation of the penetration of a high-velocity gas jet through a liquid surface," *Journal of Fluid Mechanics*, vol. 15, no. 1, pp. 13–34, jan 1963. [Online]. Available: https://www.cambridge.org/core/product/identifier/S0022112063000021/type/journal{_}article

[190] ——, "Hydromechanics of a High Velocity Gas Jet Penetrating a Liquid Surface," *SEATO Graduate School of Engineering*, no. Research Report No. 2, 1962.

[191] T. Kai, K. Okohira, M. Hirai, S. Murakami, and N. Sato, "Influence of Bath Agitation Intensity on Metallurgical Characteristics in Top and Bottom Blown Converter." *Tetsu-To-Hagane/Journal of the Iron and Steel Institute of Japan*, vol. 68, no. 14, pp. 1946–1954, 1982.

[192] Petrobras, "FISPQ Parafina Industrial," Petrobras, Tech. Rep., 2016. [Online]. Available: www.br.com.br/quimicos

[193] K. Ray, M. Isac, R. Guthrie, and M. Gagne, "A comparative study of isothermal and non-isothermal modeling of flows in tundishes," *AISTech - Iron and Steel Technology Conference Proceedings*, vol. 1, no. 33, pp. 1151–1162, 2009. [Online]. Available: http://digital.library.aist.org/download/PR-356-112.25798.pdf

[194] R. Okada and Z. I. Morita, "Evaluation of Critical Gas Flow Rate for the Entrapment of Slag Using a Water Model," *ISIJ International*, vol. 34, no. 2, pp. 164–170, 1994. [Online]. Available: http://joi.jlc.jst.go.jp/JST.Journalarchive/isijinternational1989/34.164?from=CrossRef

[195] R. D. Morales, F. A. Calderon-Hurtado, and K. Chattopadhyay, "Demystifying underlying fluid mechanics of gas stirred ladle systems with top slag layer using physical modeling and mathematical modeling," *ISIJ International*, vol. 59, no. 7, pp. 1224–1233, 2019.

[196] M. Iguchi, K. Takahashi, O. J. Ilegbusi, M. Sano, and H. Kiuchi, "Effects of the physical properties of top oil layer on bubble and liquid flow characteristics in a bottom blown water bath," *ISIJ International*, vol. 38, no. 9, pp. 1032–1034, 1998. [Online]. Available: http://joi.jlc.jst.go.jp/JST.Journalarchive/isijinternational1989/38.1032?from=CrossRef

[197] N. Kochi, Y. Ueda, T. Uemura, T. Ishii, and M. Iguchi, "Numerical Simulation on Penetration Stage of a Rising Bubble through an Oil/Water Interface," *ISIJ International*, vol. 51, no. 6, pp. 1011–1013, 2011. [Online]. Available: http://joi.jlc.jst.go.jp/JST.JSTAGE/isijinternational/51.1011?from=CrossRef

[198] D. Carvalho, M. Ribeiro, R. Correa, R. Teodoro, B. Braga, B. Maia, R. Tavares, D. Carvalho, and J. Schenk, "Measurements Methodologies for BOF converter cold modeling," Ternium, Rio de Janeiro, Tech. Rep., 2020.

[199] C. Borgnakke and R. E. Sonntag, *Fundamentals of Thermodynamics*, 8th ed. Oxford, UK: John Wiley & Sons Ltd, jan 2013. [Online]. Available: http://doi.wiley.com/10.1002/9781118516911.ch5

[200] S. Asai, T. Okamoto, J. C. He, and I. Muchi, "Mixing Time of Refining Vessels Stirred By Gas Injection." *Transactions of the Iron and Steel Institute of Japan*, vol. 23, no. 1, pp. 43–50, 1983.

[201] K. Krishnapisharody and G. A. Irons, "A unified approach to the fluid dynamics of gas-liquid plumes in ladle metallurgy," *ISIJ International*, vol. 50, no. 10, pp. 1413–1421, 2010.

[202] ——, "A critical review of the modified Froude number in Ladle Metallurgy," *Metallurgical and Materials Transactions B: Process Metallurgy and Materials Processing Science*, vol. 44, no. 6, pp. 1486–1498, 2013.

[203] D. Carvalho, B. Maia, C. Diniz, D. Souza, J. A. Guimarães, R. Salgado, and R. Tavares, "TBM tuyeres arrangements and flow - Comparison between BOF Ternium Brasil and cold model," *Iron and Steel Technology*, vol. 15, no. 4, pp. 50–57, 2018.

[204] T. CSA, "Relatório Matriz de Teste 01 - Simulação do Refino Primário em Modelo a Frio," UFMG, Belo Horizonte, Tech. Rep., 2017.

[205] D. Carvalho, D. Silveira, M. Ribeiro, R. Salgado, R. Tavares, and B. Maia, "A Novel Technique For Determination of Mixing Times in Physical Models of Steelmaking Reactors," in *ABM Proceedings*. São Paulo: Editora Blucher, oct 2019, pp. 225–234. [Online]. Available: http://abmproceedings.com.br/ptbr/article/desenvolvimento-de-nova-tcnica-para-determinao-de-tempo-de-mistura-em-reatores-siderrgicos-atravs-d

[206] D. Silveira, M. Ribeiro, R. Salgado, R. Tavares, D. Carvalho, B. Maia, and J. Schenk, "Evaluation of Mixing and Mass Transfer a t Ternium Brazil ' s B OF Through Cold Model Experiments Methodology Laboratory Tests," pp. 3–8.

[207] R. Tavares, "Mass Transfer in Steelmaking Operations," in *Mass Transfer in Multiphase Systems and its Applications*. InTech, feb 2011, no. February 2011, pp. 255–272. [Online]. Available: http://www.

intechopen.com/books/mass-transfer-in-multiphase-systems-and-its-applications/mass-transfer-in-steelmaking-operations

[208] S. H. Kim and R. J. Fruehan, "Physical modeling of gas/liquid mass transfer in a gas stirred ladle," *Metallurgical Transactions B*, vol. 18, no. 4, pp. 673–680, 1987.

[209] D. Carvalho, J. Schenk, R. Tavares, B. Maia, D. Silveira, M. Ribeiro, and R. Salgado, "Evaluation of Mixing and Mass Transfer at Ternium Brazil's BOF Through Cold Model Experiments," *Iron & Steel Technology*, no. April, pp. 84–89, 2020.

[210] D. Carvalho, H. Castro, L. Demuner, and M. Viana, "BOF Process Optimization and Technology Improvements at Ternium Brazil," *Iron & Steel Technology*, pp. 60–73, apr 2020.

[211] R. Dwivedi, "What is LightGBM Algorithm, How to use it?" 2020. [Online]. Available: https://www.analyticssteps.com/blogs/what-light-gbm-algorithm-how-use-it

[212] D. Dataman, "Explain Your Model with the SHAP Values," 2019. [Online]. Available: https://towardsdatascience.com/explain-your-model-with-the-shap-values-bc36aac4de3d

[213] G. Healy, "A new look at phosphorus distribution," *Journal of The Iron and Steel Institute*, vol. 208, no. July, pp. 664–668, 1970.

[214] R. Nagabayashi, "Mathematical expression of phosphorus distribution in steelmaking process by quadratic formalism," *ISIJ International*, vol. 29, no. 2, pp. 140–147, 1989.

[215] N. Bennenberg and H. Lachmund, "Metallurgical procedures to achieve very low phosphorus contents," *Revue de Métallurgie*, vol. 91, no. 7-8, pp. 1043–1054, jul 1994. [Online]. Available: http://www.metallurgical-research.org/10.1051/metal/199491071043

[216] H. Suito and R. Inoue, "Thermodynamic Assessment of Hot Metal and Steel Dephosphorization with MnO-containing BOF Slags," *ISIJ International*, vol. 35, no. 3, pp. 258–265, 1995.

[217] K. Chattopadhyay and S. Kumar, "Application of thermodynamic analysis for developing strategies to improve BOF steelmaking process capability," *AISTech - Iron and Steel Technology Conference Proceedings*, vol. 1, pp. 809–819, 2013.

[218] W. Urban, M. Weinberg, and J. Cappel, "Dephosphorization strategies and modeling in oxygen steelmaking," *Iron and Steel Technology*, vol. 12, no. 4, pp. 91–102, 2015.